DEVELOPMENT OF A SIMPLIFIED INFLOW MODEL FOR A HELICOPTER ROTOR IN DESCENT FLIGHT

A Dissertation
Presented to
The Academic Faculty

by

Chang Chen

In Partial Fulfillment of
the Requirements for the Degree of
Doctor of Philosophy

School of Aerospace Engineering
Georgia Institute of Technology
August 2006

DEVELOPMENT OF A SIMPLIFIED INFLOW MODEL FOR A HELICOTPER ROTOR IN DESCENT FLIGHT

Approved by:

Dr. J.V.R. Prasad, Advisor
School of Aerospace Engineering
Georgia Institute of Technology

Dr. Lakshmi Sankar
School of Aerospace Engineering
Georgia Institute of Technology

Dr. Marilyn Smith
School of Aerospace Engineering
Georgia Institute of Technology

Dr. Daniel Schrage
School of Aerospace Engineering
Georgia Institute of Technology

Dr. Chengjian He
Advanced Rotorcraft Technology, Inc.

Date Approved: May 30, 2006

To my wife Vera

ACKNOWLEDGEMENTS

I first met Dr. Prasad, my Ph.D. advisor, at the AIAA GNC conference in Boston 1998. At that time, I wanted to ask him a few questions on ship airwake formulation. I was interested in this subject because I was working on helicopter/ship dynamic interface project at the DSO National Laboratories, Singapore. Dr. Prasad impressed me as a knowledgeable and serious scholar.

Little did I know that we would soon establish a close research relationship. In 1999, I invited Dr. Prasad to come to DSO for a 5-day course on Helicopter Stability and Control. I also went to Georgia Tech for a rotorcraft specialists' meeting in 2000. Back then, Dr. Prasad invited me to visit a few research labs in the School of Aerospace Engineering. One reason for the close interaction was, of course, that we were in the same research area. Another reason was more of geography. Singapore, as a regional aviation hub, is right on the transit route on Dr. Prasad's way back his home in India.

At the end of 2001, I was awarded the DSO Postgraduate Scholarship to further my study. I applied to Georgia Tech and asked Dr. Prasad to be my Ph.D. advisor. Dr. Prasad kindly agreed. Fast forwarding to present time, I am sometimes puzzled over the fact that I applied one and only one graduate school without worrying that Dr. Prasad might well reject me. Of course, that never happened.

Since my arrival at Georgia Tech in August 2002, Dr. Prasad has provided me invaluable guidance during my study with his wisdom, patience and generosity. He encouraged me to take the Ph.D. qualifier one year after I enrolled, saving considerable time of my study duration. I always enjoy discussions with Dr. Prasad for his unique insights. For all these reasons, I give Dr. Prasad my deepest appreciation.

This study was conducted under the cooperation established between ONERA, France, and Georgia Tech as part of the US-France MoA task on rotorcraft flight dynamics. I

want to use this opportunity to specially thank Dr. Pierre-Marie Basset from ONERA. We have established close and fruitful collaborations during my Ph.D. study.

I would like to express my sincere gratitude to my dissertation advisory members: Dr. Lakshmi Sankar, Dr. Marilyn Smith, Dr. Daniel Schrage, and Dr. Chengjian He for giving their precious time for the evaluation of this dissertation. I have gained much from their valuable suggestions.

Besides Dr. Prasad, I own an enormous debt to Dr. Daniel Schrage and Dr. Robert Loewy, both from the School of Aerospace Engineering, for their great support of my applications of the Vertical Flight Foundation Scholarship in 2004 and the AIAA Foundation Award in 2005. They provided generous letters of recommendation to the point that I felt almost embarrassed upon reading them. I got the first award, but was not as fortunate with the second one.

I want to express my sincere appreciation to the DSO National laboratories for providing the financial support for my study. DSO has helped me to realize one of my dreams, and it is only proper for me to do the same thing after my graduation.

No words can describe my thankfulness towards Janice Yeo and Yao Wanli from Singapore. Four years ago, Janice and Wanli bravely (not recklessly, I hope) signed on as my guarantors for the DSO Scholarship. It is not exaggerated to say that my study wouldn't have happened without their kind agreements as guarantors.

I equally appreciate Wang Aimin, my friend for nearly twenty years, for helping my family handle all the issues while we were not around in Singapore. As an old Latin proverb says, *a friend in need is a friend indeed*.

I am very grateful, as well, to my DSO colleagues for their continuing support. Those colleagues include, but are not limited to, Ng Tong Jin, Seah Choon Siang Peter, Lim Kok Yong, Zhou Min, Pay Yew Chai, Chew Siou Chye, Cheng Wei Ping, Ho Quan Wai, Leena Goh, Priscilla Tong, and Sarah Leong Siew Wai.

I thank all my friends at Georgia Tech for their support and help. Those friends include, but are not limited to, Yeo Yong Kee, Illkay Yavrucuk, Suraj Unnikrishnan, Moon Jongki, Graham Drozeski, Manuj Dhingra, Geoffrey Jeram, Zhao Jinggen, Surresh Kannan, Henrik Christophersen, James Rigsby, David Benavente-Sanchez, Han Gil Chae, Jeff Johnson, Kyle Collins, Richard Melnyk, Justin Kighley, and Troy Schank.

I reserve the last paragraph for my family. My interest in pursuing a higher degree is no doubt inspired by my parents. I have had fruitful four years at Georgia Tech, and I hope they can be proud of that. My parents-in-law have provided us a great deal of help in the past four years. I wish them an enjoyable and more relaxing life after we settle down. Following my example, my son Tony also loves all kinds of airplanes. Hopefully he can keep it as a hobby as he grows up. My wife Vera has done everything she could to support my study during the last four years. She single-handedly took care of Tony for nearly one year during the busiest period at her company. She made a tremendous career sacrifice by taking an unpaid leave from her company for our family reunion in the States. Without her constant love and support, this work would not have been possible. It is only right to delicate this dissertation to her.

TABLE OF CONTENTS

LIST OF TABLES

LIST OF FIGURES

LIST OF SYMBOLS AND ABBREVIATIONS

c	blade chord
C_Q	rotor torque coefficient
C_T	rotor thrust coefficient
$\overline{C}_T$	rotor steady state thrust coefficient
C_{T_o}	rotor thrust coefficient at hover
GW	gross weight
k_{ring}	non-dimensional factor used to compute induced velocity from a vortex ring
k_Γ	strength factor of a vortex ring
k	empirical factor used in Newman criterion
k_x	empirical factor used in tip vortices criterion
k_z	empirical factor used in Wolkovitch criterion
N_{ring}	number of vortex rings
N_b	number of blades
Q	rotor torque
R	rotor radius
RVM	ring vortex model
S	rotor disk area
T	rotor thrust
ΔT	amplitude of rotor thrust fluctuation
V	free stream velocity

V_{con}	vertical convection speed of a vortex ring
V_h	rotor induced velocity at hover
V_i	rotor induced velocity
V_{im}	rotor mean induced velocity
V_{tp}	transport velocity of trailing vortices in Wang's model
V_{tv_X}	in-plane component of tip vortex velocity
V_{tv_Z}	vertical component of tip vortex velocity
V_x	rotor horizontal speed (positive forward)
V_z	rotor vertical speed (positive in climb)
VRS	vortex ring state
α	blade angle of attack
α_D	rotor descent angle
θ_0	collective pitch at root
$\theta_{0.75}$	collective pitch at 0.75R
θ_{tw}	blade twist
λ_i	non-dimensional induced velocity
λ_z	non-dimensional rotor vertical speed (positive downward)
$\overline{\lambda}_i$	normalized induced velocity used in Newman criterion
μ	rotor advanced ratio
$\overline{\mu}$	rotor advanced ratio normalized by induced flow at hover
$\overline{\mu}_x$	normalized translational velocity used in Newman criterion
$\overline{\mu}_z$	normalized vertical velocity used in Newman criterion

$\overline{\mu}_{WTV}$	normalized wake transport velocity used in Newman criterion
$\overline{\mu}_{WTVE}$	normalized effective wake transport velocity used in Newman criterion
$\overline{\mu}_{WTVECRIT}$	critical value of $\overline{\mu}_{WTVE}$ used in Newman criterion
ρ	air density
σ_e	equivalent rotor solidity
η	normalized rotor vertical speed (positive in climb)
η_{peak}	normalized rotor vertical speed when its corresponding normalized induced velocity reaches the peak value in the experimental results
ν	normalized induced velocity
ν_{con}	normalized vertical convection speed of a vortex ring
ν_{peak}	peak value of normalized induced velocity in the experimental results
Γ	strength of a vortex ring
Ω	rotor rotational speed

SUMMARY

A helicopter rotor in descent flight encounters its own wake, resulting in a doughnut-shaped ring around the rotor disk, known as the Vortex Ring State (VRS). Flight in the VRS condition can be dangerous as it may cause uncommanded drop in descent rate, power settling, excessive thrust and torque fluctuations, vibration, and loss of control effectiveness. As the simple momentum theory is no longer valid for a rotor in VRS, modeling of rotor inflow in the VRS continues to challenge researchers, especially for flight simulation applications.

In this dissertation, a simplified inflow model, called the ring vortex model, is developed for a rotor operating in descent condition. By creating a series of vortex rings near the rotor disk, the ring vortex model addresses the strong flow interaction between the rotor wake and the surrounding airflow in descent flight. Each vortex ring induces normal velocity at the rotor disk. In addition, the momentum theory is augmented by adjusting the total mass flow parameter to create a steady state transition between the helicopter and the windmill branches. The combined effect of the normal velocity from the vortex rings and the baseline induced velocity from the augmented momentum theory provides an improvement in predicting the inflow at the rotor disk in descent flight. With the ring vortex model, the rotor inflow can now be reasonably predicted over a wide range of descent rates.

Validations of the ring vortex model for helicopter rotors are conducted in both axial and inclined descent. Sources of test data are from four selected experiments, including Castles and Gray's wind-tunnel tests, Yaggy and Mort's wind-tunnel tests, Washizu's moving track tests, and ONERA's Dauphin flight tests. The validations focus on rotor induced velocity variation, torque requirement, collective control setting, and changes in

rotor thrust and torque. Effects from blade taper, blade twist, and rotor thrust are also discussed with further application of the finite-state inflow model.

The ring vortex model is applied to a full-scale single main-rotor helicopter. The main effort is to establish a VRS boundary based on heave stability criterion. In the dynamic simulation, two important phenomena observed in the descent flight tests are addressed, including uncommanded drop in descent rate and loss of collective control effectiveness.

In addition to being applied to the conventional helicopter, the ring vortex model is further applied to a side-by-side rotor configuration. Lateral thrust asymmetry on a side-by-side rotor configuration can be reproduced through uneven distribution of vortex rings at the two rotors. Aerodynamic interaction between the two sets of vortex rings associated with its two rotors is taken into account. Two important issues are investigated: the impact of vortex rings on lateral thrust deficit and the impact of vortex rings on the lateral AFCS limit.

CHAPTER 1 INTRODUCTION

1.1 Overview

A helicopter is able to stay aloft because its rotor pushes air downwards and generates an upward thrust to balance the rotorcraft weight. When a helicopter increases its descent rate, the downward flow due to thrust generation competes with the upward flow due to the descent motion. As a result, the smooth slipstream around the rotor disk is gradually destroyed. In particular, when the descent rate is close to the rotor-induced velocity, the rotor enters its own wake and creates a doughnut-shaped ring, known as the Vortex Ring State (VRS).

Dree and Hendal produced a series of smoke photos in their investigation of airflow patterns near the helicopter rotors (Ref. [1]), particularly in the region of VRS. A spherical airbody can be visualized in Figure 1.1 with air circulating within the airbody. As the rotor pumped energy into the flow field near the rotor, the size of the airbody continued to grow until it burst like a bubble. The airbody returned to its original shape and started the process again. In this unsteady process, the fluctuation of air mass was obvious, which in turn affected the rotor thrust and torque.

Prouty provided a vivid graphical illustration of how the flow near a rotor behaved in vertical flight, as shown in Figure 1.2 (Ref. [2]). The setting was in a wind-tunnel with the tunnel fan at the bottom and the rotor at the top. At hover, the tunnel fan was stopped and the rotor produced flow moving downstream. In order to simulate a climbing flight in the tunnel, the fan created a downflow in the tunnel. In this case, both the local flow at the rotor disk and the tunnel flow moved downward. To simulate slow descent, the fan created a small upflow in the tunnel. The local flow near the rotor disk was still dominated by the rotor-induced velocity, but the rest of the flow moved upwards. In the

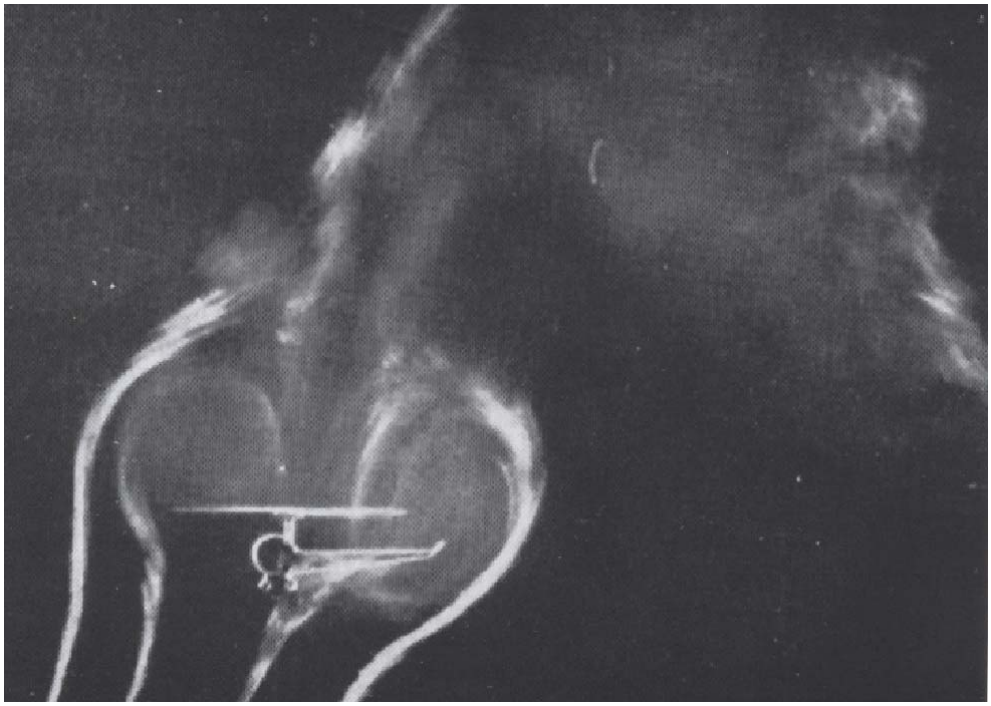

Figure 1.1: Flow visualization of a rotor in the vortex ring state condition (Ref. [1]).

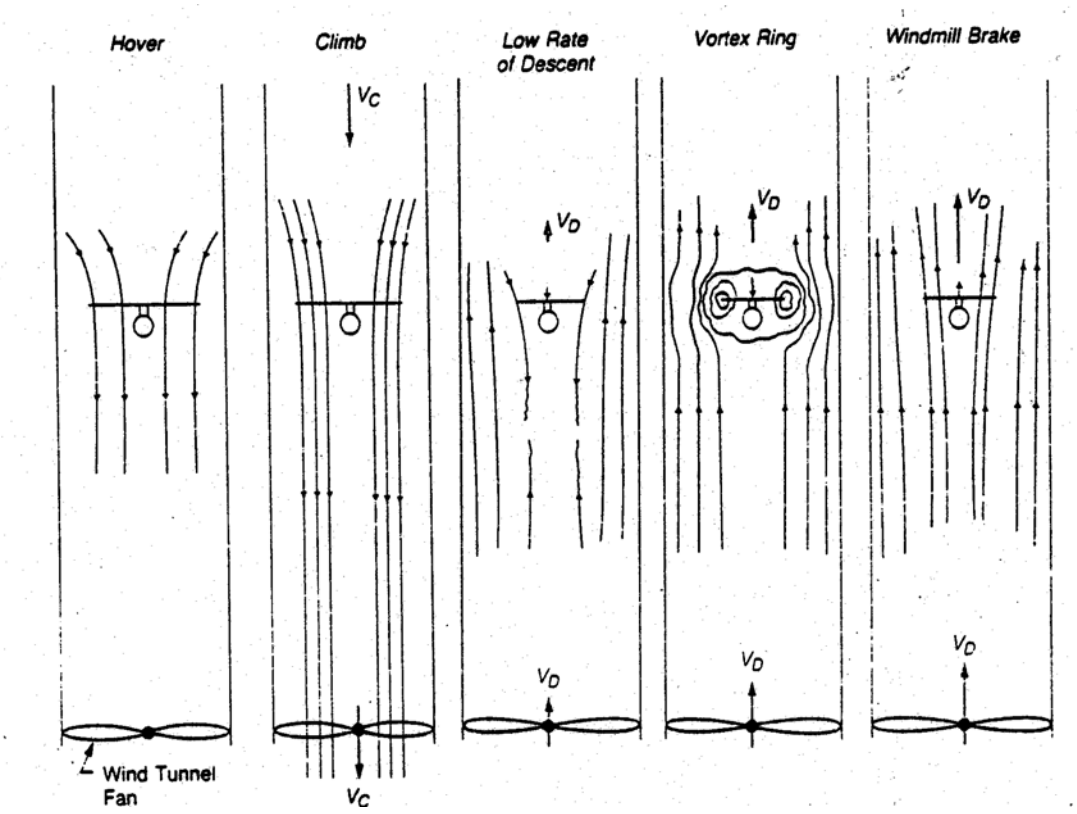

Figure 1.2: Flow behavior at vertical flight as illustrated by wind-tunnel conditions (Ref. [2]).

vortex ring state, the fan generated an upflow of the same order of magnitude as the rotor-induced velocity. In such a condition, a doughnut-shaped ring was formed near the rotor disk and recirculation of airflow could be observed. There was no existence of a definite and continuous wake in this condition. In the windmill state, the velocity of the upflow from the fan was much higher than the rotor-induced velocity. Both the local flow at the rotor and the tunnel flow moved upward. In this state, the rotor absorbed energy from free stream air.

Flight in VRS condition can be dangerous as it may result in uncommanded drop in descent rate, power increase during descent, thrust and torque fluctuations, vibration, and loss of control effectiveness. Statistically, it has been reported that between 1982 and 1997, 32 helicopter accidents occurred in the flight regime associated with the vortex ring state (Ref. [3]). More recently, in April 2000, a Marine Corps V-22 Osprey crashed in Arizona, killing all 19 Marines on board. At the time of the crash, the aircraft was flying at a rate of descent of over 2000 feet per minute while at a low horizontal speed of around 30 knots. It has been determined that a contributing cause of that accident was the vortex ring state (Ref. [4]). Just two months later in California, a Hughes 269C helicopter was substantially damaged after experiencing power settling (a phenomenon related with vortex ring state) while attempting to land and subsequently rolling over (Ref. [5]). In April 2002, a Robinson R-22 helicopter, flown by a student pilot and his instructor, crashed at Glenbeigh Strand, Ireland, during a landing practice (Ref. [6]). During the latter stage of the landing approach, both the student and the instructor observed that the rate of descent was higher than that normally experienced. Fearful of a heavy impact with the ground, the instructor went on the controls with the student. However, even with the application of "full up collective", the helicopter struck the ground heavily. The post-accident investigation suggested the vortex ring state was the most likely cause.

Descending flight is an integrated part of helicopter operations. Civil helicopters can have significant noise abatement through segmented steep approaches. Military

helicopters can increase their capability for more aggressive maneuvers. A better understanding of the VRS problem and an ability to accurately predict the VRS are highly desirable. Regrettably, current rotorcraft flight simulation models still cannot accurately predict helicopter dynamic behavior in descent flight, especially in VRS. In the following, a historical review is provided on past experimental and analytical studies of rotors in descent condition.

1.2 Literature Review

1.2.1 Experimental Tests

A number of wind-tunnel experiments and flight tests have been performed over the years. The results from these wind-tunnel experiments and flight tests have provided a better understanding of flow characteristics on rotors in descent condition. A summary of important parameters of the tested rotors is presented in Table 1.1.

Castles and Gray (1951)

Castles and Gray (Ref. [7]) performed wind-tunnel tests for rotors operating in descent condition. The rotors were tested with four different configurations and at two different rotor speeds. The purpose was to investigate effects on VRS from rotor thrust, rotor radius, rotational speed, blade taper, and blade twist.

The wind-tunnel tests found no significant differences in the inflow curves (normalized induced velocity *versus* normalized descent rate) due to variations in the thrust coefficient, rotor speed, and rotor diameter. The main effects of the 3:1 blade taper were two fold. First, for the rotor with tapered blades, normalized induced velocity decreased slightly at hover and small rates of descent. Second, for the rotor with tapered blades, the rate of descent for ideal autorotation increased by about 3% over that for the rotor with constant-chord, untwisted blades operating at the same thrust-coefficient. A

Table 1.1: Critical parameters used for experimental tests in the vortex ring state.

	Test Date	Reference	# of blades	Radius, ft	RPM	Twist	Solidity	Descent Condition	Facility
Castles and Gray	1951	[7]	3	2, 3	1200, 1600	0^o, -12^o	0.05	axial	Wind-tunnel, 9 ft
Yaggy and Mort	1962	[11]	3	4.75, 6	700 – 1410 for flapping propeller 700-1100 for rigid propeller	-22.4^o for flapping, -46.6^o for rigid	0.2 for flapping, 0.18 for rigid	axial, inclined	Wind-tunnel, 40x80 ft
Washizu	1966	[12]	3	1.8	1000	-8.33^o	0.057	axial, inclined	Moving track
Empey and Ormiston	1974	[13]	2	0.53	13250	0^o	0.105	axial, inclined	Wind-tunnel, 7x10 ft
Xin and Gao	1993	[14], [15]	2	1.8	1406	0^o, -5.5^o, -9.22^o	0.069, 0.085	axial, inclined	Whirling beam
Betzina	2001	[16]	3	2	1800	-41^o	0.119	axial, inclined	Wind-tunnel, 80x120 ft
Taghizad	2002	[9]	4	19.6	319.6	-10^o	0.083	axial, inclined	Flight test, Dauphin
V-22 IIT	2004	[17], [18]	3	19	397	-38^o	0.105	axial, inclined	Flight test, V-22

significant influence of blade twist was observed with an increase of 10% in the rate of descent for ideal autorotation. Also, an increase of 24% in the peak induced velocity occurred at 17% higher descent rate for the rotor with twisted blades. Nevertheless, as later pointed out in Ref. [8], the 9-foot wind-tunnel used in the tests may have significant facility effect on the 6-foot rotor. Despite this concern, induced velocity data obtained in the Castles and Gray's tests formed the basis of a variety of empirical inflow models (for example, Refs. [9]-[10]).

In addition to induced velocity variations, trimmed collective pitch and rotor torque at given rotor thrust were studied with respect to descent rate. It was discovered that larger collective pitch and rotor power were needed in order to increase the descent rate.

Yaggy and Mort (1962)

Yaggy and Mort (Ref. [11]) conducted wind-tunnel tests for two VTOL propellers in descent condition. Of the two propellers, one was a conventional rigid rotor, and the other was an articulated (flapping only) propeller. The tests measured steady and oscillating rotor thrust in both axial and inclined descent. The results of the tests clearly indicated the loss in steady state thrust during VRS. The amount of thrust loss varied with angle of descent.

For a given disk loading, thrust oscillation increased in magnitude with rate of descent as the propellers entered into VRS. The oscillation decreased with further increase in the descent rate as the propellers moved toward the windmill state. The oscillations in rotor thrust were found as large as ±75% of the steady state thrust. The period of oscillation was about 0.2±0.03 second for all the conditions, and seemed to be independent of test parameters.

For a given rate of descent, thrust oscillation generally diminished with increasing disk loading. This trend was maintained until the maximum thrust oscillation occurred.

Beyond the maximum thrust oscillation, the behavior varied depending on the angle of descent.

Washizu (1966)

Washizu et al carried out an experiment to measure unsteady aerodynamic characteristics of a single rotor operating in VRS (Ref. [12]). Instead of conducting the experiment in a wind-tunnel, the researchers utilized a model basin. The rotor was installed on a carriage moving on a track of the model basin. It was argued that while a wind-tunnel experiment could provide qualitative measurements of rotor characteristics, it would not always be reliable in terms of quantitative measurements. Because of the size of the fluctuating airbody around the rotor, which may extend to a distance of several rotor diameters in some descent conditions, interference effects from the wall in a wind-tunnel cannot be ignored. The wind-tunnel shall be significantly large for good quantitative measurements. In the experiment, the effective length of the track was 200 m, the width of the track was 5 m, the inner width of the building was 12 m, and the height of the ceiling from the floor was 4.7 m. In comparison, the diameter of the rotor was 1.1 m. The relative sizing of the model basin and the rotor ensured good quality of the experimental measurements.

Mean induced velocity was derived from the measured rotor power. It was observed from the experiment that rotor thrust fluctuated violently in VRS condition. In some regions of descent rate, periodic fluctuations of rotor thrust were also observed. In fact, an attempt was made to derive a VRS boundary based on the magnitude of $\Delta T / T$, where ΔT and T were the amplitude of fluctuation and the mean value of the thrust, respectively. Another finding was that rotor torque fluctuated very little when compared with rotor thrust.

Empey and Ormiston (1974)

Empey and Ormiston (Ref. [13]) tested a 1/8-scale AH-1G helicopter in a wind-tunnel. Although the purpose of the experiment was to investigate tail-rotor performance for in ground effect, measurements from the tests provided plenty of data for a rotor in VRS condition. The rotor was tested in the settling chamber of the USAAMRDL – Ames Directorate 7- by 10-foot wind-tunnel. The chamber was 30- by 33-foot, sufficiently large to eliminate wind-tunnel wall effects even for very low speed conditions. The tail rotor had a diameter of 1.061 feet with the solidity of 0.1051 and no twist. The test conditions included both axial and non-axial flow.

From the tests, it was observed that the largest thrust reduction occurred in climb condition, while significant unsteady perturbations occurred in axial descent.

Xin and Gao (1993)

Xin and Gao conducted whirling beam tests in axial and non-axial descent (Refs. [14]-[15]). During the axial descent tests, remarkable fluctuations in both rotor thrust and torque were observed, especially in the region of $\eta = -0.6$ to $\eta = -0.8$ (η being normalized rate of descent). The loss in the mean rotor thrust was also clearly indicated in the same region. At $\eta = -0.28$, power settling was observed as the curve of rotor torque reversed its downtrend and began to go up for increased descent rates. Effect of disk loading on the non-dimensional mean rotor torque appeared to be insignificant.

Similar variations of mean rotor torque were observed in steep inclined descent. However, as the angle of descent was reduced to 45^o, the changes became less obvious. In fact, there was a steep decrease in mean rotor torque beyond $\eta = -0.28$, indicating that the rotor was clear of VRS. There was no evidence of VRS when the descent angle was below 30^o.

The torque fluctuations were more severe in the 75^o and 60^o inclined descent than they were in axial descent. It was suggested that the most turbulent VRS occurred in steep

inclined descent with descent angle between 60^o and 75^o. As the descent angle decreased, the torque fluctuations became smaller and finally disappeared below 30^o inclined descent. This was because the in-plane component of free stream was large enough to blow the turbulent flow away from the rotor.

While a number of researchers predicted VRS boundaries based on either heave dynamics stability characteristics (Refs. [8]-[9]) or rotor thrust oscillations (Refs. [12], [16]), Xin and Gao were able to obtain the boundary based on rotor torque measurements.

Betzina (2001)

Betzina's wind-tunnel tests provided the first VRS data directly applicable to the tilt-rotor configuration (Ref. [16]). From the experiment, thrust fluctuations and mean rotor thrust reduction were detected in the VRS region. Relatively large differences in VRS effects were reported when an isolated rotor was tested with and without an image plane (used to simulate a second rotor). These differences implied that a side-by-side rotor configuration might have significantly different VRS characteristics than a single rotor. However, in the later V-22 flight test program (Refs. [17]-[18]), it was discovered that the side-by-side rotor interference is not a primary factor in determining the V-22 VRS boundary.

Taghizad (2002)

Taghizad et al from ONERA conducted experimental and theoretical investigations to develop an aerodynamic model for a rotor in steep descent (Ref. [9]). The tested aircraft was an SA 365N Dauphin 6075. Several behaviors were observed during the flight test, especially in the VRS region. During the phase leading to VRS, the crew first felt an increased level of vibration, followed by a sudden increase in the rate of descent. Increasing the collective control did not prevent the helicopter from descending at an increased rate. During the descent, the helicopter was very unstable and hard to control. The flight test also established that the VRS effects disappeared beyond a certain forward

velocity. The increase in the forward velocity undoubtedly stabilized the rate of descent. Hence, one conclusion from the flight tests was that in order to minimize the VRS effects, a pilot was better off increasing the indicated airspeed rather than increasing the collective.

V-22 Flight Test Program (2004)

Extensive flight tests were conducted to evaluate VRS effects on the V-22 tilt-rotor aircraft (Refs. [17]-[18]). Initial testing was aimed at defining a steady state VRS boundary. Controllability of the aircraft in VRS was also evaluated and effective recovery technique was demonstrated. Subsequent testing demonstrated dynamic maneuvers deeply penetrating the steady state VRS boundary. The test program found that the V-22 aircraft had a greater sink-rate margin for VRS avoidance than that of a conventional helicopter.

The degradation of control effectiveness in the vertical axis often presented for a single-rotor configuration. However, for a tilt-rotor configuration, uncommanded roll response was more obvious in VRS. Thus, the two main criteria in defining VRS effects for the V-22 were uncommanded thrust fluctuations and uncommanded roll response. With quantitative substantiations of VRS effects, the test team was able to develop a VRS onset boundary. It was found that the VRS boundaries between the tilt-rotor aircraft and the conventional helicopter were remarkably similar.

High blade twist and high disk loading are two distinctive features of a V-22 rotor. From the flight test program, it was found that blade twist was not a primary factor in determining the V-22 steady state VRS boundary. However, high disk loading allowed higher descent rates before VRS symptoms were encountered. Higher thrust also extended the VRS boundary to higher forward airspeeds.

While the commonly used VRS recovery technique for the conventional helicopter was to initiate cyclic command to gain forward speed, the V-22 pilot could mechanically

actuate forward tilting of nacelle in order to rapidly restore lateral control during VRS. This marked an improvement over the conventional helicopter, which depended on a rotor aerodynamic flapping response following the cyclic command to recover from VRS.

1.2.2 Analytical Investigations

From the review above, it seems that experimental tests have been relatively sparse. In addition, analytical investigations have not been particularly encouraging as well. Limited efforts on inflow modeling have been conducted, and a review of the analytical studies is provided in the following.

Wolkovitch (1972)

In order to analytically predict the VRS boundary in descent condition, Wolkovitch considered a flow model consisting of a slipstream with uniform flow at any rotor section surrounded by a protective tube of vorticity (Ref. [19]). The tube was made up of tip vortices leaving the rotor. It was assumed that the unsteady vortex ring flow was associated with a breakdown of this protective tube of vorticity. Some key ideas used by Wolkovitch are later extended in the proposed inflow model, as described in Chapter 2.

Heyson (1975)

Heyson argued that the simple momentum theory, when properly interpreted, yielded the optimum performance of the rotor in descent flight (Ref. [20]). On the one hand, the flow in VRS was circulatory and unsteady, therefore no resemblance of a smooth slipstream postulated by the theory. On the other hand, the existence of the rotor thrust in VRS suggested that there must be a transfer of momentum to the surrounding air. This transfer of momentum might occur under less than ideal conditions with all viscous losses and all losses caused by non-uniformity of momentum transfer.

Johnson (1980)

Johnson elaborated that, even in hover condition, there was entrainment of air into the slipstream below the rotor and some recirculation near the disk (Ref. [21]). Such phenomena were not included in the simple momentum theory since those effects on the induced power were negligible at hover. However, the flow pattern in VRS resembles a vortex ring in the plane of the rotor disk or just below it. The blade tip vortex spirals piled up due to the upward free stream velocity in descent. With each revolution of the rotor, the ring vortex built up strength until it broke away from the rotor disk in a sudden breakdown of the flow.

Wang (1990)

Wang applied classical vortex theory in axial descent (Ref. [22]). Instead of assuming the conservation of circulation in an ideal flow, Wang assumed a linear decay of circulation of trailing vortices owing to the effect of the fluid viscosity and the interaction of the induced flow with the opposite free-stream flow, typical of a real wake. The distance required for the linear decay (down to zero) was further assumed to be directly proportional to the transport velocity of trailing vortices, V_{tp}. The direction of vortex shedding depended on the direction of V_{tp}. When $V_{tp} < 0$, the trailing vortices were shed downward and *vice versa*. VRS occurred when $V_{tp} = 0$. With this model, good correlations were achieved between the predicted induced velocity and the experimental data from Ref. [7].

The concepts of transport distance and transport velocity of trailing vortices helped spur the development of the proposed inflow model. It is also noted that Wang did not extend his work to inclined descent.

Leishman, Bhagwat, Brown, Newman and Perry (2002)

A significant development of VRS study in recent years has been the time-accurate free-vortex wake scheme initiated by Leishman and Bhagwat (Ref. [23]). The aerodynamic phenomenon associated with the descending flight is described as follows. At hover and low descent rate, the rotor wake is inherently unstable. As the descent rate increases, the wake is more prone to be unstable and the regular helical structure of the wake tends to break down. As net velocity near the rotor becomes low at higher descent rates, vorticity accumulates near the rotor plane, and individual tip vortices form tight bundles of vorticity resembling vortex rings. Vorticity may break away from the rotor disk suddenly, usually with only a small variation in rate of descent.

With the free-vortex wake model, thrust time-histories were computed for a 4-bladed rotor and for a 2-bladed rotor. In both rotor configurations, thrust fluctuations were initially modest, followed by rapid growth in intensity before subsiding in the turbulent wake state. The fluctuations eventually died down as the rotor operated in the windmill state. The onset of thrust fluctuations for the 2-bladed rotor occurred at a much higher rate of descent than for the 4-bladed rotor. The net duration for VRS was shorter with 2-bladed rotor. This suggested that the rotor was more susceptible to develop wake instabilities with a large number of blades.

In the computation of rotor induced power during a continuous transition from hover to windmill state, the free-vortex wake method was able to match experimental results up to $\eta = -0.3$. However, there was a significant drop in power consumption with the free-vortex wake method while experimental results showed much higher power consumption. It was argued that aerodynamic losses resulting from rotational effects in the flow might be important in improving the power prediction.

The effect of rotor thrust (or disk loading for a given rotor) was two fold. On the one hand, the tip vortex strengths for a given rotor were proportional to the blade loading

coefficient (C_T / σ). This implied an increased susceptibility to the development of wake instabilities. On the other hand, increased axial separation distance between adjacent vortex filaments due to higher rotor thrust suggested a decreased susceptibility to wake instabilities. The numerical investigation showed that increasing rotor thrust made the wake marginally more stable.

The primary effect of blade twist was to off-load the blade loading at the tip region, and thus to reduce the convection velocity of the wake. In terms of wake instability, the blade with higher twist was potentially more prone to develop wake instability.

Brown, Leishman, Newman and Perry further suggested that the onset of VRS was related to the collapse of the orderly structure of the rotor wake into a highly disturbed, irregular, aperiodic flow state (Ref. [24]). Their calculations traced the evolution of the rotor wake in VRS and suggested that the location of the VRS boundary and the depth of VRS regime were sensitive to the blade spanwise loading distribution. It was suggested that blade twist would have significant effect on rotor behavior in VRS.

Through detailed computation of flow behavior, the free-vortex wake approach offers a better understanding of VRS initiation and subsequent development. Nevertheless, this approach is computationally expensive and numerically sensitive. Moreover, it has inherent difficulties being integrated with current helicopter flight simulation models.

Basset and Prasad (2002)

As rotorcraft flight dynamics in the VRS flight region are highly nonlinear, bifurcation theory can be utilized to address the problem of the aerodynamic instability of the rotor in VRS. Basset and Prasad applied bifurcation theory in the study of VRS (Ref. [25]). The finite-state unsteady wake approach provided an ideal modeling structure for their nonlinear analysis. A model with three axi-symmetric states was used and nonlinear dynamic behaviors were found rich enough to catch the various dynamic characteristics of the rotor inflow. Those behaviors included stable and unstable equilibrium points,

stable and unstable limit cycles and even the chaotic vibrations associated with a strange attractor. As a preliminary study, the authors stressed that the emphasis was on the application of the bifurcation and nonlinear dynamics techniques rather than on the realism of the models and parameters. Thus, certain parameters in the inflow model associated with special nonlinear behaviors might not be realistic enough in the application to a practical helicopter.

Johnson (2004)

The momentum theory has been widely used at hover and in climb and even forward flight conditions for flight dynamics analyses and simulation. However, this theory breaks down in descent flight due to the collapse of the smooth slipstream. Nevertheless, due to its simplicity, rotorcraft researchers have developed various methods in extending the simple momentum theory to descent flight. One of the earliest efforts can be traced back to Glauert (Ref. [26]). Recent attempts were from He (Ref. [10]) and Taghizad (Ref. [9]). They individually formulated parametric extension of momentum theory in the flow model to remove the modeling singularity in VRS and rendered simulation models to cover the full range of flight conditions.

Perhaps the most comprehensive parametric extension of momentum theory was carried out by Johnson (Ref. [8]). A broad review of available wind-tunnel and flight test data was conducted for rotors in VRS. Using the available data, Johnson initiated an empirical VRS model suitable for simple calculations and for real-time simulations. The development of the VRS model was conducted in two steps. The first step was to eliminate the singularity of the momentum theory at ideal autorotation in axial descent. The second step was to create the region of negative (inflow) slope in VRS. In both steps, third order polynomials were identified as a function of descent rate. For the formula's details, refer to Ref. [8].

With this empirical VRS model, Ref. [8] showed negative (unstable) heave damping for a certain range of descent rates, and the VRS boundary was thus defined in terms of the stability boundary of the aircraft flight dynamics. Besides the advantages offered by the parametric extension, this approach has an apparent drawback, *i.e.*, a lack of dependence on critical rotor parameters such as rotor solidity and blade twist.

1.2.3 A Few Frequently Asked Questions

This section responds to a few frequently asked questions related to the descent flight. The answers to these questions can be regarded as a summary of the historical review.

1. What is the general status of current studies for VRS?

Although the studies for a rotor in descent condition have been traced back to as early as the 1920s, the results have been far from satisfactory. The two commonly used methods include the free-vortex wake and the parametric extension of momentum theory. Both methods have their shortcomings. The free-vortex wake method is computationally expensive, numerically sensitive, and difficult to integrate with current rotorcraft flight simulation software. The parametric extension method, on the other hand, is too general and has no correlation with important model parameters such as blade taper, blade twist, and disk loading.

2. What are the limitations of using wind-tunnel tests in the VRS study?

Strong facility effect is always a concern when conducting wind-tunnel tests. Because the size of the fluctuating airbody around the rotor often extends to a distance of several rotor diameters in VRS condition, interference wall effect cannot be ignored. Castles and Gray (Ref. [7]) had a 6-foot diameter rotor in a 9-foot wind-tunnel. The test conducted by Yaggy and Mort (Ref. [11]) was made in the NASA Ames 40- by 80-foot wind-tunnel with its bigger 12-foot diameter propeller. Washizu tested a 1.1-meter diameter rotor using a model basin in a building with an inner width of 12 meters (Ref. [12]). Empey

and Ormiston experimented a 1.061-foot diameter rotor in a 30- by 33-foot settling chamber of the USAAMRDL (Ref. [13]). Among the listed wind-tunnel tests, it appears that Castles and Gray's tests had the strongest wall effect.

Measurements conducted in these wind-tunnel tests often focused on flow visualization, flow speed derivation, and rotor thrust and torque fluctuations. Due to the nature of wind-tunnel experiments, typical VRS characteristics including rapid increase in descent rate and loss of control effectiveness can be observed only in flight tests.

3. What does the loss of control effectiveness mean in descent flight?

It is well-known from the flight tests that a pilot can experience difficulty with collective control in VRS. Once the pilot encounters unstable heave dynamics, collective increase may not prevent the helicopter from descending at an increased rate.

Erratic pitch and roll responses have also been reported in the past (Ref. [27]). Decreasing collective pitch when approaching unsteady conditions precipitated the nose-down pitching. In some cases, application of a significant rearward cyclic control didn't stop the nose-down motion. Rather violent, random yawing motions were also noticed for some flights in VRS condition (Ref. [8]).

4. What are the effects of the fuselage and tail rotor on main rotor VRS?

Flow interference from the fuselage and other parts of the helicopter tends to have a more significant effect on the rotor under descending condition than it does under other flight conditions. When the shape of a fuselage is more that of a circular cylinder, vortex shedding known as *von Karman vortex street* can be observed behind the fuselage. If the shape of a fuselage is more box-like, unsteady wake influence from the fuselage becomes even stronger. Due to the presence of an upflow acting upon the fuselage in descent flight, an unsteady wake from the fuselage may affect a significant portion of the main rotor, resulting in variations in flow characteristics, blade load distribution, trim, and vehicle dynamic response.

Rotor/Fuselage interaction remains an open problem in the rotorcraft community, even under much benign flight conditions. Brown studied fuselage and tail rotor interference effects on the helicopter wake development in descending flight (Ref. [28]). VRS development on the main rotor appeared to be strongly influenced by the flow conditions in a critical region above the rear of the rotor disk. The fuselage modified the flow in this critical region with subtle but significant effect on the VRS character. VRS development tends to be relatively insensitive to the strong perturbation caused by the tail rotor.

In Ref. [8], the upflow acting upon the tail boom in descending condition directly contributed to a large nose-down pitching observed in the previous flight tests. The situation became even more aggravated when the tail boom was not streamlined.

5. How important is the prediction of induced velocity?

Induced velocity is a key parameter for the study of a rotor in descent condition. In fact, it is the foundation of the parametric extension of momentum theory (Refs. [8]-[10], [26]). If the prediction of induced velocity is accurate, the corresponding trimmed collective pitch, rotor power, and even dynamic response can be correlated fairly well. Moreover, because the slope of inflow curve (induced velocity *versus* descent rate) determines the entry into and exit out of VRS in the heave stability criterion, the corresponding VRS boundary is significantly impacted by the accuracy of induced velocity prediction in descent flight.

6. How does blade stall affect the VRS?

It seems that blade stall would have a significant effect in the harsh aerodynamic environment of VRS. Nevertheless, a number of flight tests have shown otherwise. Reeder and Gustafson conducted motion picture study on a Sikorsky R4 helicopter and discovered no appearance of blade stall (Ref. [29]). Stewart observed no aerodynamic stalling in the helicopter rotor among the Sikorsky R-4B, R-6, Bell 47, and Bristol 171 (Ref. [30]). This was due to the fact that increasing collective pitch still had a beneficial

effect during the descent flight. Taghizad had similar observation in the Dauphin flight tests (Ref. [9]). During the tests, increasing collective pitch always had a positive effect on reducing the descent rate for at least a short while, although it may not be effective in the long run (an issue of loss of control effectiveness). In the recent V-22 flight test program, no issue on blade stalling was reported (Refs. [17]-[18]).

7. Why some conclusions from both experiments and analytical methods appear to be inconsistent?

Sometimes experiments and flight tests provide inconsistent conclusions regarding certain aspects. For example, the influence of blade twist on a rotor in descent condition is controversial. Castles and Gray observed a strong influence of blade twist on the induced velocity distribution (Ref. [7]). Betzina and Leishman (Refs. [16], [23]) were concerned about the high blade twist of the V-22 aircraft. Nevertheless, flight tests conducted by V-22 test and evaluation team claimed that blade twist had an insignificant role in defining the VRS boundary (Ref. [17]-[18]).

1.3 Present Work

The objective of the current research is to develop a simplified inflow model appropriate for studying and simulating rotorcraft flight dynamics in descent flight. This new model will avoid intensive computational effort demanded in the free-vortex wake technique and will be easily integrated into current flight simulation models. The simplified inflow model will also be capable of correlating with model parameters such as blade taper, disk loading, and blade twist, and addressing the influence of these parameters on flight dynamic behaviors in VRS.

This simplified inflow model, called the ring vortex model, is proposed for inflow modeling in the descent region including VRS (Refs. [31]-[37]). By creating a series of vortex rings near the rotor disk, the ring vortex model addresses the strong interaction

between the rotor wake and the surrounding airflow in descent flight. Each vortex ring induces normal velocity at the rotor disk. In addition, the total mass flow parameter in the existing flow models (including the momentum theory) is adjusted to create a steady state transition between the helicopter and the windmill branches. The combined effect of the additional normal velocity from the vortex rings and the baseline induced velocity from the augmented inflow models provides an improvement in predicting the inflow at the rotor disk in descent flight. With the ring vortex model, the rotor induced inflow can be adequately computed over the entire range of descent flight.

Extensive model validations are required in order to refine the model and understand its limitations. In this study, validations of the ring vortex model for helicopter rotors are conducted extensively in both axial and inclined descent.

Applications of the ring vortex model include both a full-scale single main-rotor helicopter and a side-by-side rotor configuration. In the single main-rotor helicopter, the main effort is to establish VRS boundary based on heave stability criterion. In addition, two important phenomena observed in the descent flight tests are addressed in the dynamic simulation, including uncommanded drop in descent rate and loss of collective control effectiveness. In the side-by-side rotor configuration, two important issues are investigated, including the effect of the vortex rings on lateral thrust deficit and on the lateral AFCS limit.

1.4 Organization of Dissertation

The fundamental problem of rotor inflow modeling in descent flight is described in Chapter 1. Literature reviews on both experimental tests and analytical investigations are provided. The present work stems from the need to develop a simplified inflow model appropriate to rotorcraft flight dynamic study and simulation in descent flight.

In order to develop an efficient and yet accurate representation of the rotor inflow, in Chapter 2, a ring vortex model is proposed for inflow modeling in the descent regime.

Concepts of the ring vortex model and methods to quantify critical parameters in the model are discussed in detail. A method is also introduced to create a steady state transition phase. With the ring vortex model, the rotor induced inflow can be adequately predicted over the entire range of descent flight..

In Chapters 3 and 4, validations of the ring vortex model for helicopter rotors in both axial and inclined descent are conducted. Sources of test data are selected from four experiments, including Castles and Gray's wind-tunnel tests, Yaggy and Mort's wind-tunnel tests, Washizu's moving track tests, and ONERA's Dauphin flight tests. The validations focus on rotor induced velocity variation, trimmed collective control and torque, and changes in rotor thrust and torque. Also illustrated are effects from blade taper, blade twist, and rotor thrust.

In Chapter 5, the ring vortex model is applied to a full-scale single main-rotor helicopter. The main effort is to establish VRS boundary based on heave stability criterion. In addition, two important phenomena observed in the descent flight tests are reproduced in the dynamic simulation. These are uncommanded drop in descent rate and loss of collective control sensitivity.

In addition to being applied to the conventional helicopter, the ring vortex model is also applied to a side-by-side rotor configuration, as described in Chapter 6. Lateral thrust asymmetry on a side-by-side rotor configuration can be produced through uneven distribution of the vortex rings at the two rotors. Aerodynamic interaction between the two sets of vortex rings is taken into account. Two important issues are investigated, including the effects of VRS on lateral thrust deficit and on lateral AFCS limit.

In Chapter 7, conclusions drawn from this study are provided in conjunction with recommendations for future work.

CHAPTER 2 RING VORTEX MODEL

Momentum theory is a simple and efficient tool for inflow modeling at hover and in climb and forward flight. Although the theory breaks down in descent flight due to the collapse of the smooth slipstream, various methods have been developed in extending the momentum theory to descent flight (Refs [8]-[10], [26]). Those extensions have shown some level of engineering capability in flight dynamics analyses and simulation. Therefore, a review of the momentum theory is appropriate.

A major part of the chapter establishes the ring vortex model for the computation of inflow velocity around the rotor disk in descent condition. Concepts of the model and methods to quantify critical modeling parameters are discussed in detail. A method is also introduced to create a steady state transition phase.

2.1 Review of Momentum Theory

The basic momentum equation for a rotor is provided as follows (Ref. [38]):

$$\nu\sqrt{\bar{\mu}^2+(\nu+\eta)^2}=1 \tag{2.1}$$

where η,ν and $\bar{\mu}$ represent normalized values of vertical speed (positive upwards), induced velocity, and forward speed, respectively. Equation 2.1 is essentially a steady state first order representation of the average induced airflow across the rotor in the Peters-He theory (Ref. [39]). The normalization here is conducted by $\nu=\frac{V_i}{\Omega R\sqrt{C_T/2}},\eta=\frac{V\sin\alpha_D}{\Omega R\sqrt{C_T/2}},\bar{\mu}=\frac{V\cos\alpha_D}{\Omega R\sqrt{C_T/2}}$, where V_i,V and α_D are the velocities of induced flow and free stream airflow, and the rotor descent angle, respectively. In axial descent, $\bar{\mu}=0$. Equation 2.1 can be further simplified as:

$$\nu^2(\nu+\eta)^2=1 \tag{2.2}$$

The solution of Equation 2.2 can be obtained for ν in terms of η:

$$\nu = \frac{-\eta + \sqrt{\eta^2 + 4}}{2}, \forall \eta \tag{2.3}$$

$$\nu = \frac{-\eta + \sqrt{\eta^2 - 4}}{2}, \eta \le -2 \tag{2.4}$$

$$\nu = \frac{-\eta - \sqrt{\eta^2 - 4}}{2}, \eta \le -2 \tag{2.5}$$

Note that there are multiple equilibriums for ν when $\eta \le -2$. The above solutions of ν are plotted in Figure 2.1. In order to study the stability characteristics of the equilibrium curves, nonlinear bifurcation analysis software, XppAut, was utilized in generating the plot (Ref. [40]). An extensive treatment of XppAut in the application of VRS study can be referred to Ref. [25]. The upper branch corresponding to Equation 2.3 is often called the helicopter branch, while the lower branch corresponding to Equation 2.5 is the windmill branch. Both the helicopter and the windmill branches are stable, as evident in Figure 2.1. However, the branch corresponding to Equation 2.4 is unstable.

Figure 2.2 gives a comparison of normalized induced velocity between the experimental data from Ref. [7] and the predictions from the momentum theory. Three aspects of Figure 2.2 are noteworthy. First, the momentum theory under-predicts the values of induced velocity along the helicopter and the windmill branches. The increment of induced velocity from the experimental data over the momentum theory data is clearly nonlinear. It is almost negligible at hover, but increases as the rotor descends faster. The increment reaches its peak value at about $\eta = -1.5$. Second, the experimental data shows a transition phase between the helicopter and the windmill branches. There is no such transition accounted for by the momentum theory. Third, the experimental data exhibits considerable fluctuations in the induced velocity distribution. This feature is not captured by the momentum theory.

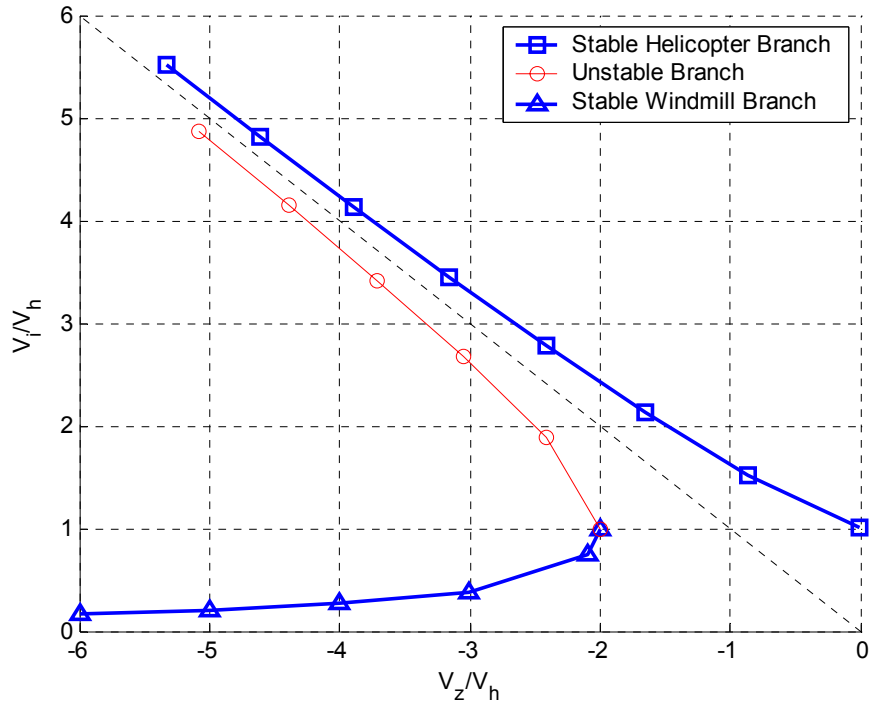

Figure 2.1: Equilibrium curves from the momentum theory using XppAut.

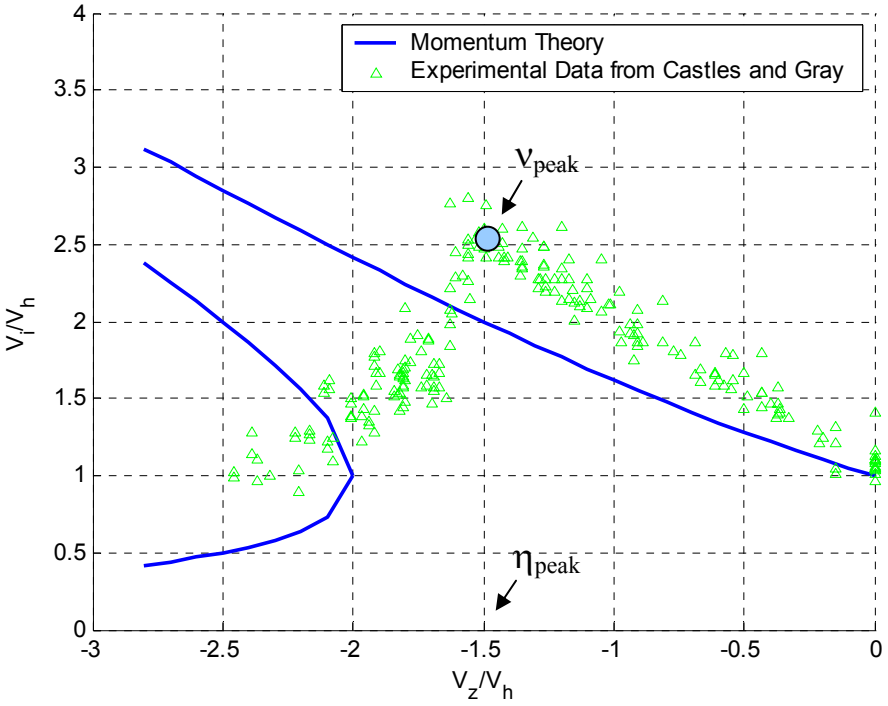

Figure 2.2: Comparison between the experimental data and the momentum theory.

For the convenience of illustration, three notations are defined based on the distribution of the experimental data in Figure 2.2, *i.e.*, VRS phase, transition phase, and windmill phase. The VRS phase ranges from hover to a descent rate (η_{peak}) where its corresponding normalized induced velocity reaches the peak value (ν_{peak}). The windmill phase refers to the windmill state. The transition phase is the connection between the VRS phase and the windmill phase. Notice that these three notations are mainly useful in axial and inclined descent for V_x / V_h up to 0.6204, as indicated in Figure 4 of Ref. [25]. As forward velocity increases during the descent, the transition phase shrinks and eventually disappears.

As a further investigation of the momentum theory, numerical simulation is conducted based on a generic helicopter model. The model has a 3-bladed rotor with a rotor radius of 27 ft. Other key parameters include a rotor speed of 27 rad/sec, a solidity of 0.0816, and a blade twist of -13^o (Ref. [31]). The rotorcraft model is implemented using a commercial rotorcraft modeling and simulation tool, FLIGHTLAB™ (Ref. [41]). When one-state inflow model is chosen in FLIGHTLAB™, the inflow model is the same as Equation 2.1.

Figure 2.3 shows variations of normalized induced velocity (ν). During steady state calculations, two initial conditions of collective pitch are chosen: 16^o and 4^o. The curve with square markers in the figure corresponds to a starting value of θ_0 at 16^o, while the curve with triangle markers corresponds to an initial condition of θ_0 at 4^o. In Figure 2.3, two different steady states are reached at high descent rates with different initial conditions of θ_0. It is also noted that multiple steady states occur when the normalized vertical speed η is beyond -2.2, instead of -2 as predicted by the momentum theory. The reason could be largely due to the trim algorithm implemented in the simulation software.

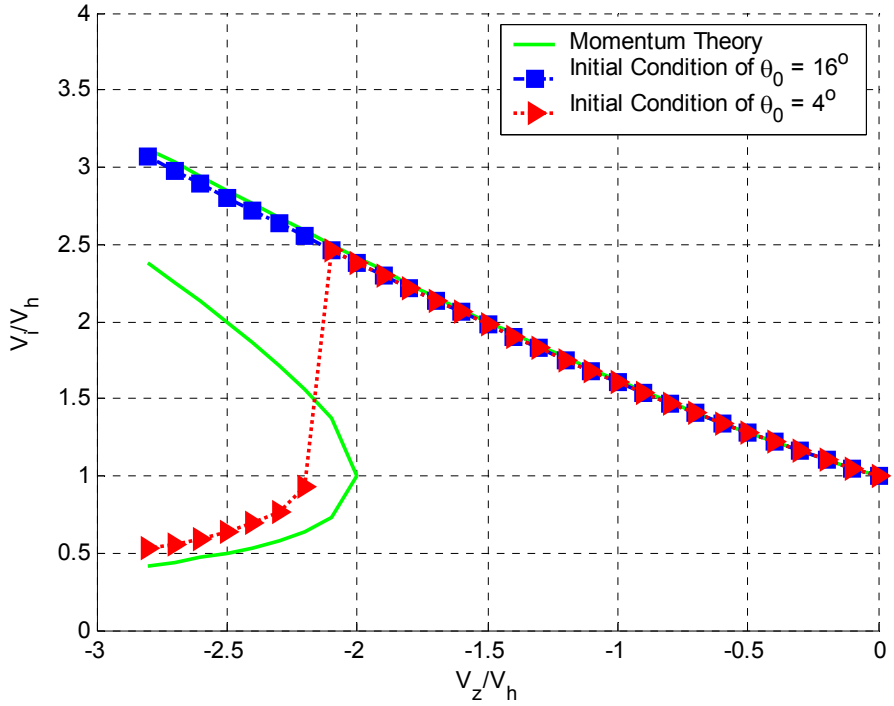

Figure 2.3: Induced velocity variations with different initial values of collective pitch.

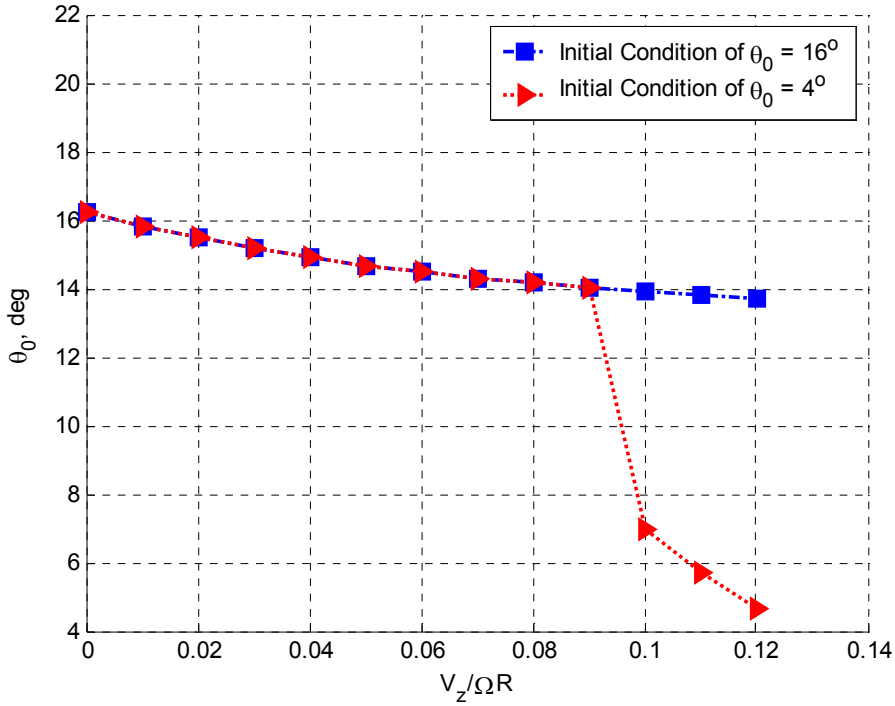

Figure 2.4: Trimmed collective pitch variations with different initial values of collective pitch.

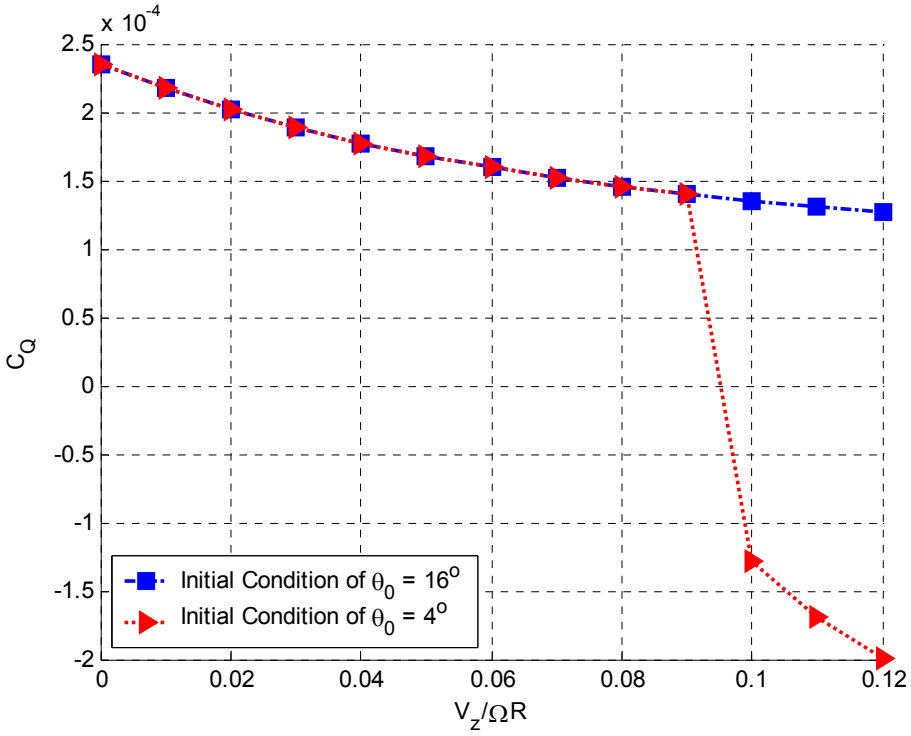

Figure 2.5: Torque coefficient variations with different initial values of collective pitch.

Variations of collective pitch in terms of vertical descent rate are shown in Figure 2.4. Similar to Figure 2.3, multiple steady state values can be observed at high descent rates. Figure 2.5 illustrates torque coefficient variations with respect to vertical descent rate. Notice that at high descent rate, C_Q has negative value when the initial value of θ_0 is at 4^o. This indicates that a rotor indeed extracts power from its descent, as it is expected in the windmill mode. It is also noted that when the initial value of θ_0 is at 16^o, the rotor continuously operates on the helicopter branch and consumes power even at high descent rates. This is of course physically unrealistic.

2.2 Ring Vortex Model

One major source of induced velocity under-prediction by the momentum theory is ignorance of the interaction between the rotor wake and the surrounding airflow. As indicated in Ref. [21], there is entrainment of air into the slipstream below the rotor and

some recirculation near the disk in descent condition. The effect of the flow interaction may be less significant at hover or in climb. Nevertheless, as a helicopter increases its descent rate, the flow interaction becomes more and more intense due to larger velocity gradients between the upflow outside the wake and the downflow inside the wake.

It is therefore conceptualized that, due to the flow interaction, there exists a series of vortex rings located at the rotor periphery. Indicated in Figure 2.6a for axial descent at low rate, the vortex rings move downward along the wake. As the rate of descent increases, the vortex rings tend to accumulate near the blade tip, as shown in Figure 2.6b. When the rate of descent further increases, the vortex rings move upward along the wake, as depicted in Figure 2.6c. A new vortex ring is formed at every rotor rotation, *i.e.,* $2\pi/\Omega N_b$ second. The locations of these discrete vortex rings are determined by the product of convection velocity of the vortex rings and $2\pi m/\Omega N_b$ (m: an integer representing the numbering of vortex rings).

Each vortex ring induces normal velocity at the rotor disk. The flow field of a vortex ring can be computed based on elliptic integrals, and its normal velocity components are tabulated in Ref. [42]. The combined effect of the normal velocity from the vortex rings and the baseline induced velocity from the momentum theory[1] provides an improvement in predicting the inflow at the rotor disk in descent flight. One advantage of utilizing vortex rings is that the effect of vortex rings is non-uniform with respect to relative distance between the rings and the rotor disk. The closer a vortex ring locates to the rotor disk, the larger the magnitude of normal velocity that acts on the disk. The non-uniform effect conforms to the experimental observation in Figure 2.2.

Unlike axial descent, the flow environment in an inclined descent condition is no longer symmetric near the rotor disk. From a modeling point of view, one needs to track

[1] The momentum theory is later augmented to create a steady state transition from the helicopter and the windmill branches. Details will be given in Section 2.4.2.

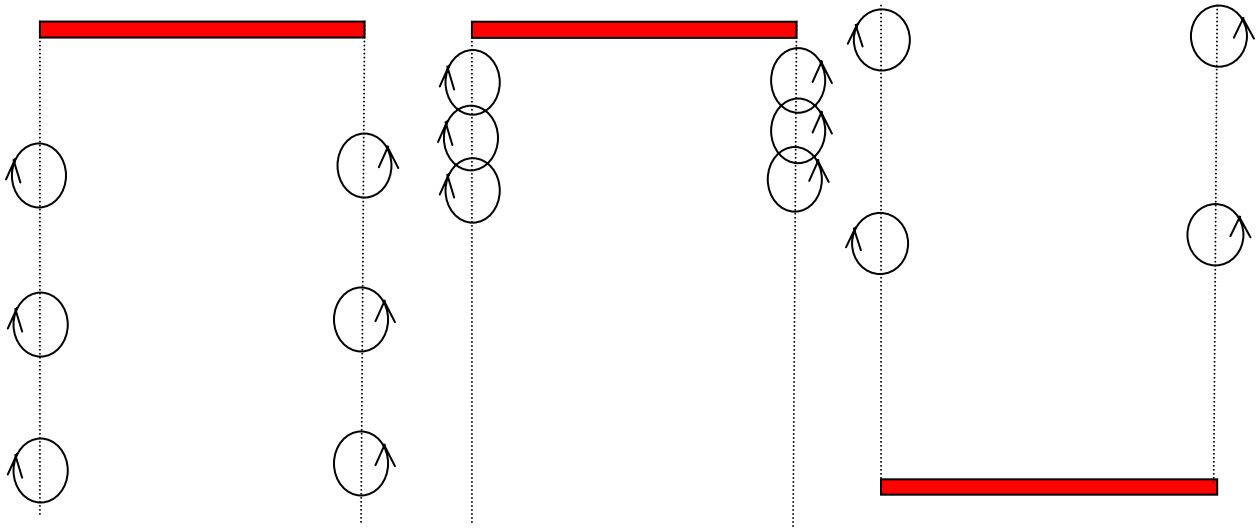

a. Hover and slow descent rate **b. Moderate descent rate** **c. High descent rate**

Figure 2.6: Motion of vortex rings in axial descent.

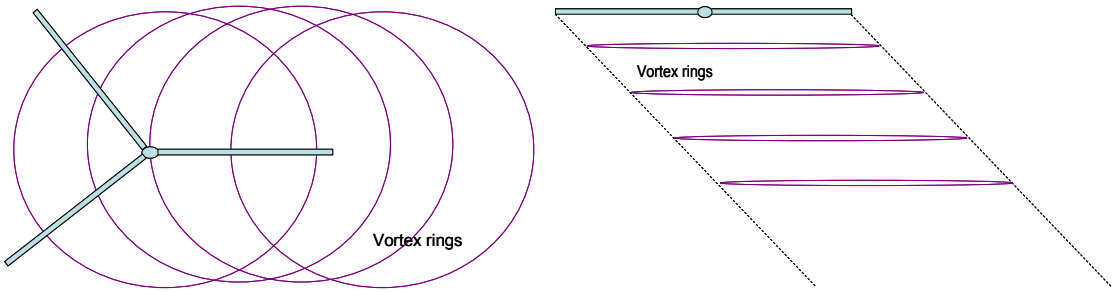

Top view **Side view**

Figure 2.7: Schematic of influence of the ring vortex model on the rotor disk in inclined descent.

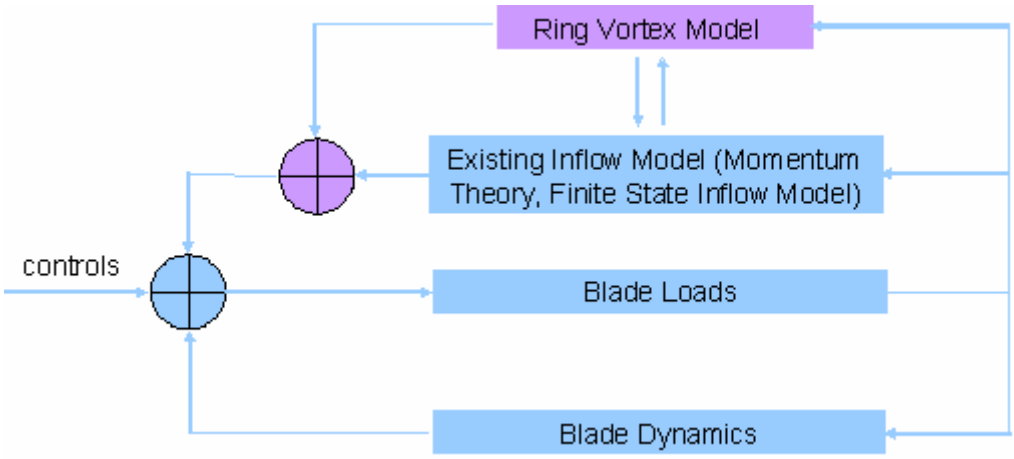

Figure 2.8: Interaction between the ring vortex model and other rotor model components.

the relative distance between aerodynamic computational points on the rotor blades and the vortex rings at every time step. A schematic is provided in Figure 2.7, illustrating how vortex rings could influence induced velocity distribution at the rotor disk. While some portions of the rotor disk experience the downflow, other parts of the rotor disk are subject to the upflow. The resultant mean induced velocity is the average of induced velocities at different radial stations and azimuths.

With the improvement of induced velocity, the required collective pitch is different from the prediction based on the momentum theory. The increase in induced velocity effectively reduces blade angle of attack, and thus requires a larger collective pitch to balance rotor thrust or vehicle weight. Subsequently, higher collective pitch may be needed to increase rate of descent. By the same token, a larger value of rotor torque may also be required as descent rate increases, a phenomenon known as power settling.

The method illustrated herein is named the ring vortex model (RVM). The scope of the RVM is not restricted to the presence of vortex rings. It also includes a steady state transition described in Section 2.4.2. The interaction between the RVM and other rotor model components are depicted in Figure 2.8. Application of the ring vortex model is intended to analyze a rotor in descent condition. The effect of the ring vortex model is

diminished in other flight conditions, including climb and forward flight. This is because vortex rings are quickly swept away from the rotor disk in those flight conditions. Therefore, no special consideration is needed while incorporating the ring vortex model into a flight simulation model at flight conditions other than descent since the contribution from vortex rings to induce velocity is anyway very much diminished at those flight conditions.

2.3 Convection Speed, Vortex Strength, and Number of Vortex Rings

As seen in Figure 2.2, the increment of induced velocity in the experimental data reaches its peak (denoted as υ_{peak}) at a certain descent rate (denoted as η_{peak}, approximately -1.5). In the ring vortex model, the increment in induced velocity over the momentum theory is caused by the vortex rings. Therefore, it can be reasoned that the vortex rings would locate in the same plane of the rotor disk at $\eta = \eta_{peak}$. It can thus be deducted that the vertical convection speed of the vortex rings, V_{con}, is close to zero at $\eta = \eta_{peak}$ in order to produce the largest increment at the rotor disk.

At hover, the vertical convection speed of the vortex rings is equal to V_h (the induced velocity at hover). By combining the vertical convection speeds at both $\eta = 0$ and $\eta = \eta_{peak}$, the normalized vertical convection speed, ν_{con}, can be prescribed as follows:

$$\nu_{con} = \upsilon - \frac{\upsilon_{peak}}{\eta_{peak}}\eta \tag{2.6}$$

Here, ν is the normalized induced velocity. Equation 2.6 is essentially a linear approximation of the actual convection speed of the vortex rings.

In inclined descent, the effect of forward velocity component of free stream air is to sweep the vortex rings behind the rotor disk. Therefore, the total convection speed of a

vortex ring is the vector sum of the vertical convection speed and the forward velocity component.

As a vortex ring is formed by the flow interaction at the blade tip, the strength of a vortex ring is proportional to the velocity gradient between the upflow outside the rotor disk and the downflow inside the disk. Moreover, as a vortex ring is produced by air entrainment, the strength of a vortex ring is also proportional to the rotor radius since a larger vortex ring traps more air. Hence, the strength, Γ, is estimated with the following formula:

$$\Gamma = k_{\Gamma} R V_i \tag{2.7}$$

where V_i is the mean induced velocity and k_{Γ} is the strength factor to be determined.

According to Ref. [42], the increment, ΔV_i, from the vortex rings is determined as follows:

$$\Delta V_i = N_{ring} \frac{k_{ring} \Gamma}{R} \tag{2.8}$$

where N_{ring} is the number of vortex rings and k_{ring} is a non-dimensional factor used to compute induced velocity from a vortex ring in Ref. [42]. At $\eta = \eta_{peak}$, we have

$$\Delta V_i = (\upsilon_{peak} - \upsilon_{mom}) v_h = N_{ring} \frac{k_{ring} k_{\Gamma} R \upsilon_{peak} v_h}{R} \tag{2.9}$$

A relationship between N_{ring} and k_{Γ} can thus be established by the following formula:

$$N_{ring} k_{\Gamma} = \frac{\nu_{peak} - \nu_{mom}}{k_{ring} \nu_{peak}} \tag{2.10}$$

where ν_{mom} is the normalized induced velocity from the momentum theory at $\eta = \eta_{peak}$. The average value of k_{ring} is approximately 0.75 when a vortex ring locates in the same plane of the rotor disk. If the values of ν_{peak} and ν_{mom} are known from the experiment,

the product of N_{ring} and k_Γ becomes a constant. From Figure 2.2 , values for ν_{peak} and ν_{mom} are determined as 2.5 and 2.0, respectively. It thus follows

$$N_{ring} k_\Gamma = 0.2667 \tag{2.11}$$

In the numerical simulation, the number of vortex rings can be varied within a selected range. By doing so, vortex rings may survive beyond its nominal value with slightly benign aerodynamic environment at a particular moment, or prematurely burst in a slightly adversary environment at another moment. With different number of vortex rings, magnitudes of induced velocities are expected to scatter around their nominal values. This indeed provides a numerical means of simulating randomness in the distribution of induced velocity, and hence, randomness in the thrust and torque coefficients.

A sensitivity study is thus carried out to investigate the influence of the number of vortex rings. The judging criterion is to observe the variation range of normalized induced velocity due to random variation of the number of rings. Numerical results from the sensitivity study are presented in Figure 2.9. The experimental data shown in the figure are from Ref. [7]. It is observed from the figure that the best selection of the nominal number of vortex rings is two. When choosing one more (2+1) and one less (2-1) vortex ring, the predicted variation range of normalized induced velocity covers a large number of test data. When choosing two more (2+2) and one less (2-2) vortex rings, the predicted variation range covers almost all the test data.

A numerical investigation is conducted based on the generic helicopter model discussed in Section 2.1. In the simulation, the number of vortex rings is set at two while $\eta_{peak} = -1.5$ and $\nu_{peak} = 2.5$. Figure 2.10 presents induced velocity variation using the ring vortex model along the helicopter and the windmill branches. The predicted results capture the right trend of the experimental data from Ref. [7]. It is cautiously noted that

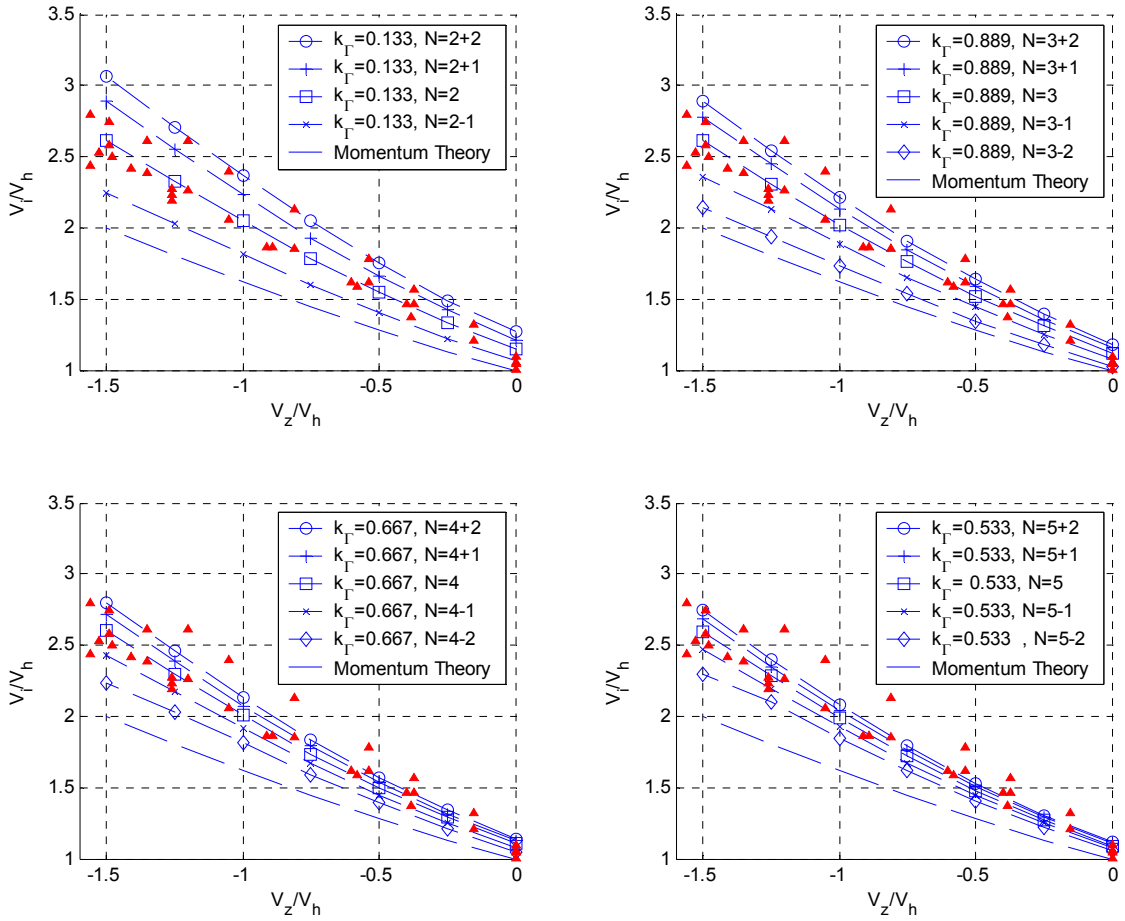

Figure 2.9: Sensitivity study on the number of vortex rings.
(In the plot, triangular markers represent test results)

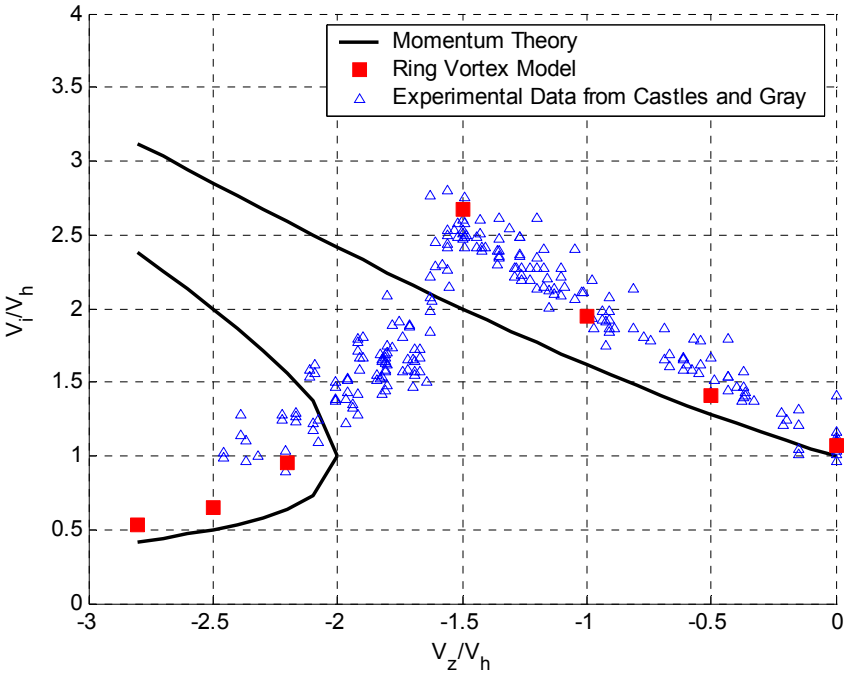

Figure 2.10: Induced velocity comparisons between the ring vortex model, the experimental data and the momentum theory.

the modeling parameters used in the simulation are not the same as those used in Ref. [7]. Nevertheless, the experimental data in Ref. [7] do represent a general trend of the normalized induced velocity of a rotor in descent condition. While the results presented in Figure 2.10 represent a preliminary evaluation of the ring vortex model, a detailed validation of the model is presented in Chapter 3.

2.4 Transition Phase

In the ring vortex model, the downward velocity from the vortex rings is added to the induced velocity calculated from the momentum theory. The concept works well in the VRS and the windmill phases (see Figure 2.10). Nevertheless, in axial and inclined descent (V_x / V_h up to 0.6204), the momentum theory fails to predict a transition phase between the helicopter and the windmill branches. To solve this problem, two methods are proposed for the transition: dynamic transition and steady state transition.

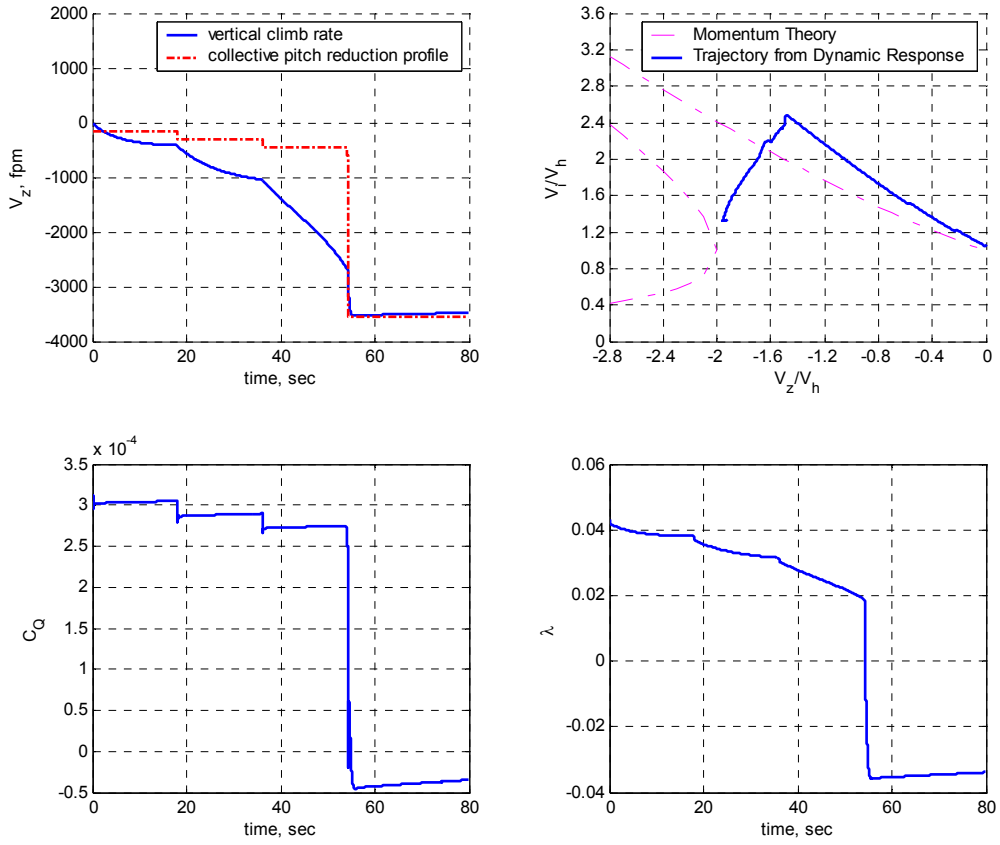

Figure 2.11: Dynamic transition due to collective pitch reduction.

2.4.1 Dynamic Transition

As both the helicopter and the windmill branches represent steady state solutions for the inflow dynamics, the transition between these two regions can be initiated by applying a collective control reduction with a full-vehicle flight dynamic model.

The simulation for dynamic transition is based on the generic rotorcraft model illustrated in Section 2.1. The collective control reduction profile is shown in the top left plot of Figure 2.11. The collective pitch is initially decreased gradually. A large reduction occurs at approximately 53 seconds into the simulation, after which the collective pitch remains unchanged. The corresponding vertical descent rate is also presented in the same plot. During the first two mild collective reductions, the descent rate decreases moderately. However, there is a rapid increase in the descent rate following the third mild

reduction. During the process, the net velocity at blade tip decreases rapidly. When the net velocity at blade tip approaches zero, it triggers the large reduction in collective pitch. The amount of reduction corresponds to the collective pitch difference between the steady state values at $\eta = -1.5$ and $\eta = -2.0$. At the final stage of dynamic simulation, the descent rate reaches a steady value of approximately $\eta = -2.0$.

Variation of inflow curve is shown in the top right plot of Figure 2.11. The presence of a transition between the helicopter and the windmill branches is clearly indicated. From the bottom right plot of Figure 2.11, it can be seen that this dynamic transition essentially forces the total inflow to change its sign, hence the switch between two steady state solutions. Rotor torque coefficient is shown in the bottom left plot of Figure 2.11. During the final phase of the simulation, the rotor extracts power from air after the vehicle stabilizes at a large sink rate.

Vehicle response to collective control changes shown in Figure 2.11 clearly demonstrates that the transition between the helicopter and the windmill branches can be achieved through collective changes in the dynamic simulation. This is consistent with a pilot's experience when one lowers the collective control lever to *flat pitch* in order to enter into autorotation. The idea of dynamic transition is also parallel to dynamic transition between two domains of attraction in nonlinear dynamics. It may be the only way to set up a connection between the helicopter and the windmill branches under the current setting of the momentum theory. Nevertheless, it is realized that the dynamic transition method is sensitive to the collective control reduction profile. Both the magnitude and rate of reduction contribute to resultant variation in induced velocity during the transition. Moreover, the dynamic transition can be utilized only to simulate rotor behavior from the helicopter branch to the windmill branch in a dynamical sense. It cannot predict the intermediate state of inflow in a steady state sense.

2.4.2 Steady State Transition

In axial and inclined descent (V_x / V_h up to 0.6204), there is no steady state transition between the helicopter and the windmill branches in the momentum theory. In order to obtain intermediate flow state, an augmentation to the original momentum theory (as shown in Equation 2.1) is suggested in the following equation:

$$\nu\sqrt{\left(\frac{\eta}{2.72(1+\bar{\mu}^2)}\right)^2+\bar{\mu}^2+(\eta+\nu)^2}=1 \tag{2.12}$$

where $\bar{\mu}$ is the normalized value of advanced ratio. Figure 2.12 provides steady state inflow solutions based on the augmented momentum theory at different advanced ratios. The results in Figure 2.12 indicated that steady state transitions are indeed created between the helicopter and the windmill branches at different forward speeds with the augmented momentum theory.

It is worthwhile to take a closer look at the additional term, $\left(\frac{\eta}{2.72(1+\bar{\mu}^2)}\right)^2$. When $\eta+\nu=0$ (ideal autorotation) and $\bar{\mu}=0$ (axial descent), Equation (2.12) can be easily solved with $\eta=-\nu=-1.65$. Note that the experimental value for ideal autorotation is $\eta=-1.79$ (Refs. [2], [21]). The rationale of such a selection is that -1.65 is the minimum value of which Equation (2.12) has no multiple equilibria over the entire range of descent rates. On the other hand, the difference between -1.65 and -1.79 can be compensated with the inclusion of vortex rings. Details can be found in the validations of the ring vortex model in Chapter 3.

In addition, it is interesting to notice that the additional term, $\left(\frac{\eta}{2.72(1+\bar{\mu}^2)}\right)^2$, is proportional to η^2. In this sense, the term can be physically interpreted as a form of

parachute drag since the rotor behaves like a parachute in the region of ideal autorotation.

When the rotor is in vertical climb, the value of ν diminishes with the increase of climb rate. As such, Equation (2.12) can be approximated by the following form:

$$\nu\sqrt{\left(\frac{\eta}{2.72}\right)^2+\eta^2}=1 \tag{2.13}$$

Note that the influence of the term $\left(\frac{\eta}{2.72}\right)^2$ is much less than that of the term η^2. On the other hand, when the value of $\bar{\mu}$ is large, it follows that $\left(\frac{\eta}{2.72(1+\bar{\mu}^2)}\right)^2 << \bar{\mu}^2$. It is therefore concluded the effect of the additional term diminishes in both climb and forward flight.

The momentum theory provides a uniform induced velocity throughout the rotor disk. It cannot be utilized to investigate the effect of blade taper and blade twist. A natural choice is to select the finite-state inflow model (Ref. [39]). Similar to the adjustment associated with the simple momentum theory, the mass flow parameter, V_T, needs to be modified in the same fashion to accommodate a steady state transition in the inflow model. The augmented inflow models are given in Appendix A. Moreover, it is essential to include a reasonable number of inflow states for an intended study (Ref. [39]). Three inflow states are considered as the minimum number of states to account for radial variation in the spanwise distribution of inflow due to blade taper and blade twist. On the other hand, seven inflow states are the minimum number of states to take into account both radial and azimuthal variation up to 1st harmonic for the effect of forward speed.

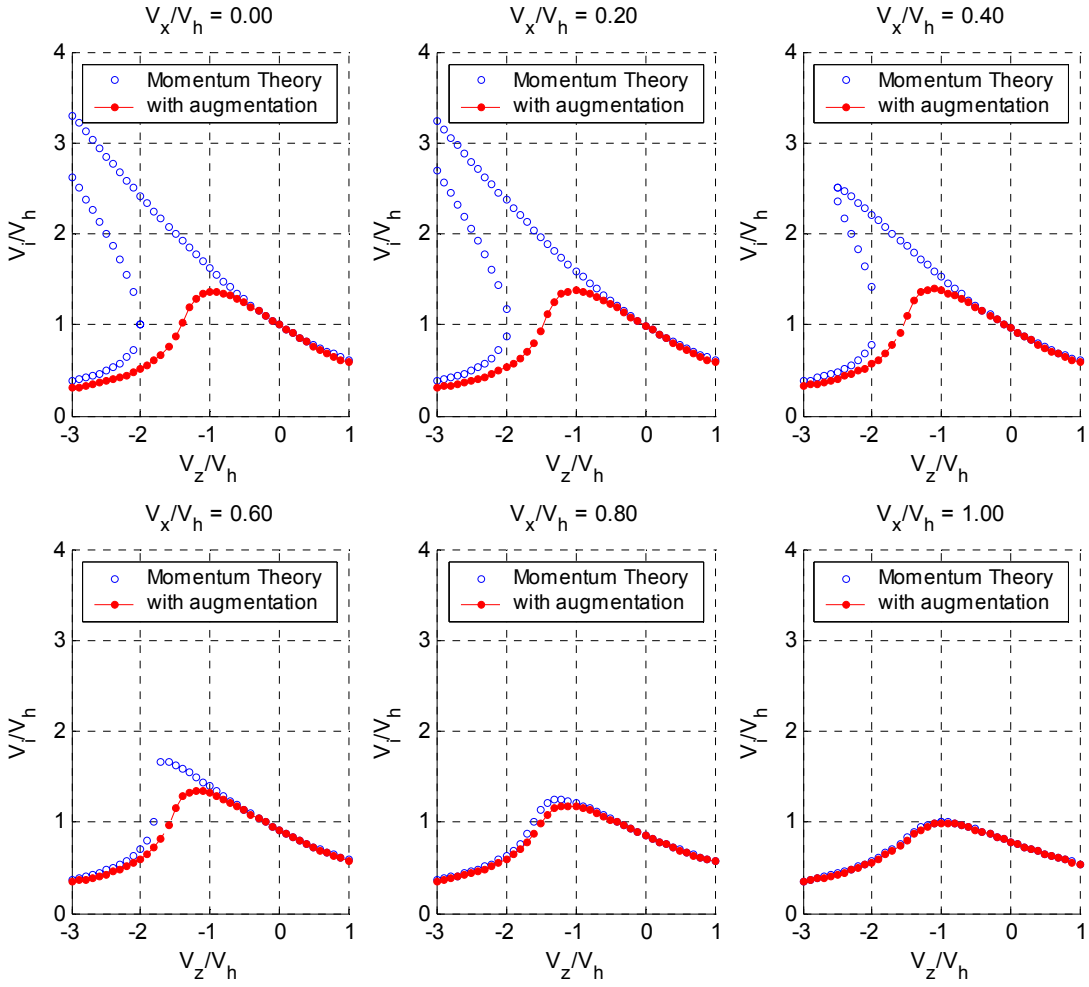

Figure 2.12: Induced velocity distribution with the augmented momentum theory.

CHAPTER 3 VALIDATIONS FOR A ROTOR IN AXIAL DESCENT

In this chapter, validations of the ring vortex model are conducted for a rotor in axial descent. Sources of test data are selected from four experiments, including Castles and Gray's wind-tunnel tests, Yaggy and Mort's wind-tunnel tests, Washizu's moving track tests, and ONERA's Dauphin flight tests. An overview of these four experiments is first provided. In-house rotor models based on parameters from these four experiments are formulated individually. With the ring vortex model, steady state simulations are carried out for rotors in descent conditions. Validations are focused on induced velocity variations, torque requirement, collective control setting, and changes in rotor thrust and torque. Effects from important rotor parameters are also addressed.

3.1 Overview of Experimental Tests

An overview of wind-tunnel experiments and flight tests utilized in the validations is given in the following. The overview concentrates on test set-up, configurations of rotor models, and major test results.

3.1.1 Castles and Gray's Wind-Tunnel Tests

Castles and Gray performed wind-tunnel tests for rotors operating in axial descent condition (Ref. [7]). The wind-tunnel was 9-foot diameter open jet, with a 10-foot long test section. The basic rotor model had three blades with an effective solidity of 0.05 and NACA 0015 blade airfoil section. During the experiment, the rotors were tested at two different rotational speeds: 1200 RPM and 1600 RPM. In order to investigate the influence of critical rotor parameters, tests were performed on four rotor configurations: (1) Constant-chord, untwisted blades of 3-foot radius; (2) Untwisted blades of 3-foot

radius with a 3:1 taper; (3) Constant-chord blades of 3-foot radius with a linear twist of -12^{o}; (4) Constant-chord, untwisted blades of 2-foot radius. In the subsequent numerical study, these four rotor models, respectively, are named as baseline, reduced-radius, tapered, and twisted rotors. Three sets of variables were monitored, including induced velocity, trimmed collective pitch, and steady state rotor torque.

3.1.2 Yaggy and Mort's Wind-Tunnel Tests

Yaggy and Mort tested two propellers operating in descent condition in the NASA 40- by 80-foot wind-tunnel (Ref. [11]). One was a conventional rigid rotor, while the other was an articulated (flapping only) propeller. The 9.5-foot diameter propeller had a solidity of 0.203 and a blade twist of -22.5^{o}. The propellers were tested under the following conditions: (1) Rotational speed: 700 to 1100 rpm for the rigid propeller and 700 to 1410 rpm for the flapping propeller; (2) Descent rates: 0 to 6000 fpm for the rigid propeller and 0 to 3000 fpm for the flapping propeller; (3) Angle of descent relative to the flight path: 0^{o} for the rigid propeller (axial descent) and 0^{o} to 60^{o} for the flapping propeller. Both steady state rotor thrust and thrust oscillation were obtained.

3.1.3 Washizu's Moving Track Tests

Washizu conducted moving track tests of a rotor in descent condition (Ref. [12]). The 1.1-meter diameter rotor had a solidity of 0.0573 and a rotational speed at 1000 rpm. Each blade weighed 100 gram with a blade twist of -8.33^{o}. The blade, of NACA 0012 airfoil, can flap and lag with both hinges at 3.27% R. No pitch mechanism was employed. The tests focused on rotor thrust and torque measurements.

3.1.4 ONERA's Dauphin Flight Tests

ONERA performed flight tests in steep descent (Ref. [9]). The aircraft was a SA 365N Dauphin 6075 with a test weight of 3500 kg. The 5.965-meter radius main rotor had a

solidity of 0.083 and a blade twist of -10.2°. The flight test results included induced velocity distribution and the VRS boundary.

During the validations, different types of in-house rotor models were established in the MATLAB™ environment, corresponding to their hardware counterparts in the experiments. In particular, all of the configurations presented in the Castles and Gray's wind-tunnel tests were simulated in order to investigate effects of critical rotor parameters. Although two types of propellers were tested in the Yaggy and Mort experiment, only the flapping rotor model was built-up in the numerical study. In the simulation, the ring vortex model is integrated with those in-house rotor models for inflow modeling in descending condition. In all simulations, the nominal number of rings is set at 2, while $\eta_{peak} = -1.5$ and $\nu_{peak} = 2.5$. Moreover, the finite-state inflow model is chosen over the momentum theory in the calculation of baseline induced velocity: 3-state model for axial descent (radial variation) and 7-state model for inclined descent (radial and azimuthal variations). Step-by-step computational procedures using the ring vortex model are provided in Appendix B.

3.2 Induced Velocity Variations

Castles and Gray's test results are utilized in the first validation. Induced velocity variations from the numerical investigations and the wind-tunnel tests are presented in Figure 3.1 to Figure 3.4, with each figure corresponding to each of the four rotor configurations. Different markers used in the figures represent a combination of thrust coefficient and rotor speed: unfilled markers stand for the experimental data while filled markers are predictions using the ring vortex model. Note that the experimental data are not available for some combinations of thrust coefficient and rotor speed.

In general, predictions with the ring vortex model correlate well with the experimental data for all four configurations over a wide range of descent rates, including the VRS

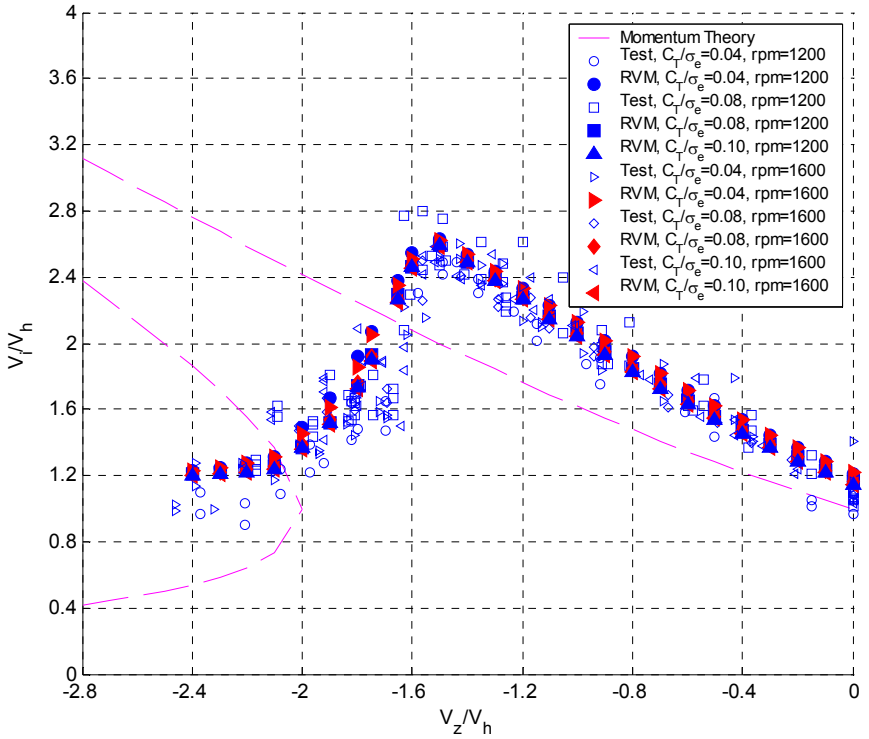

Figure 3.1: Induced velocity variations with Castles and Gray's baseline rotor model: axial flow.

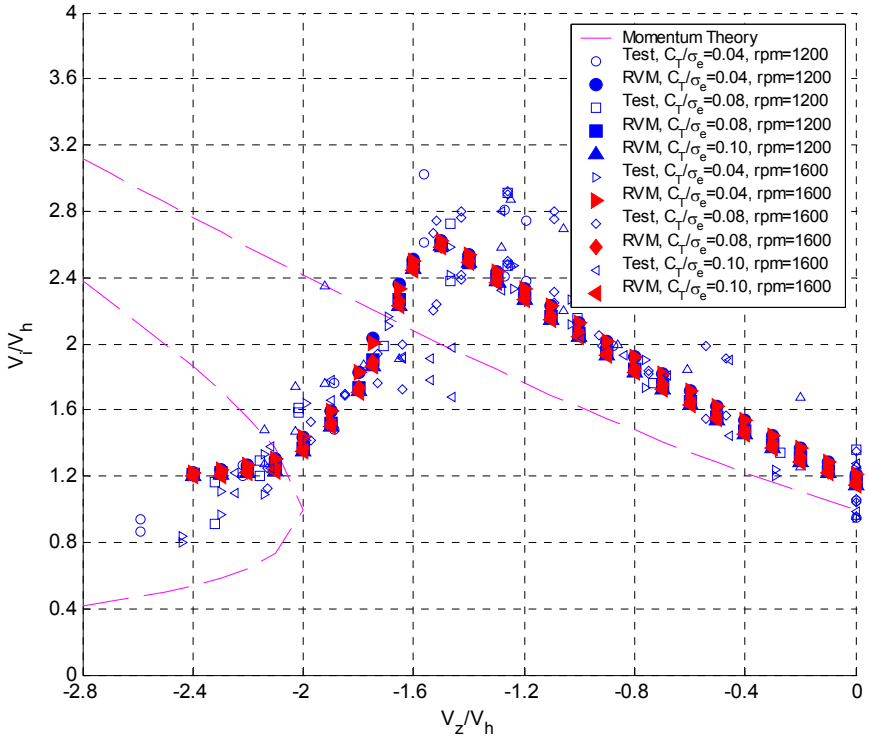

Figure 3.2: Induced velocity variations with Castles and Gray's reduced-radius rotor model: axial flow.

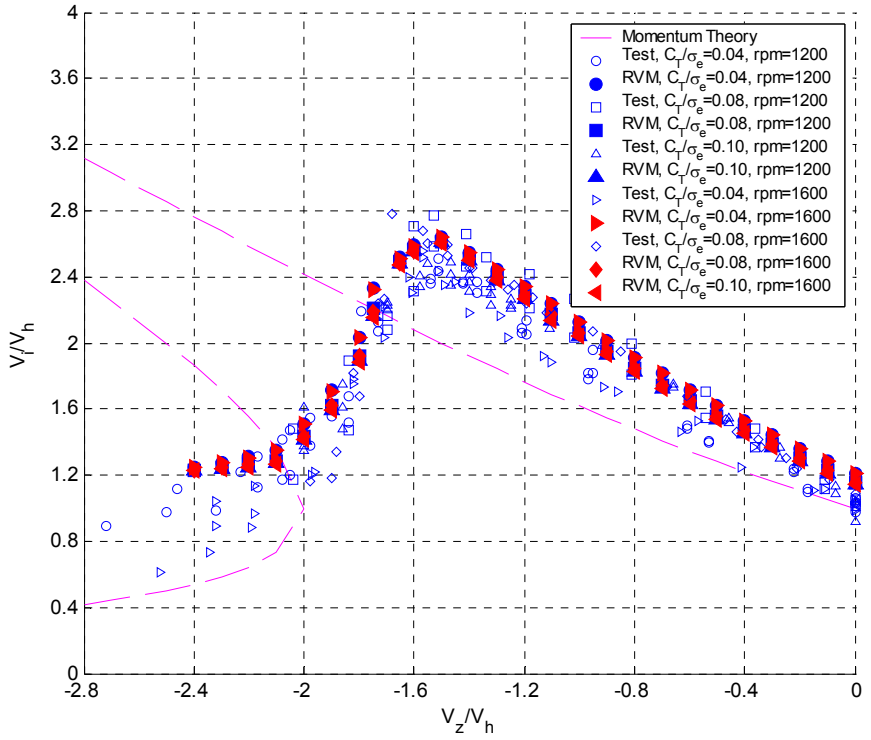

Figure 3.3: Induced velocity variations with Castles and Gray's tapered rotor model: axial flow.

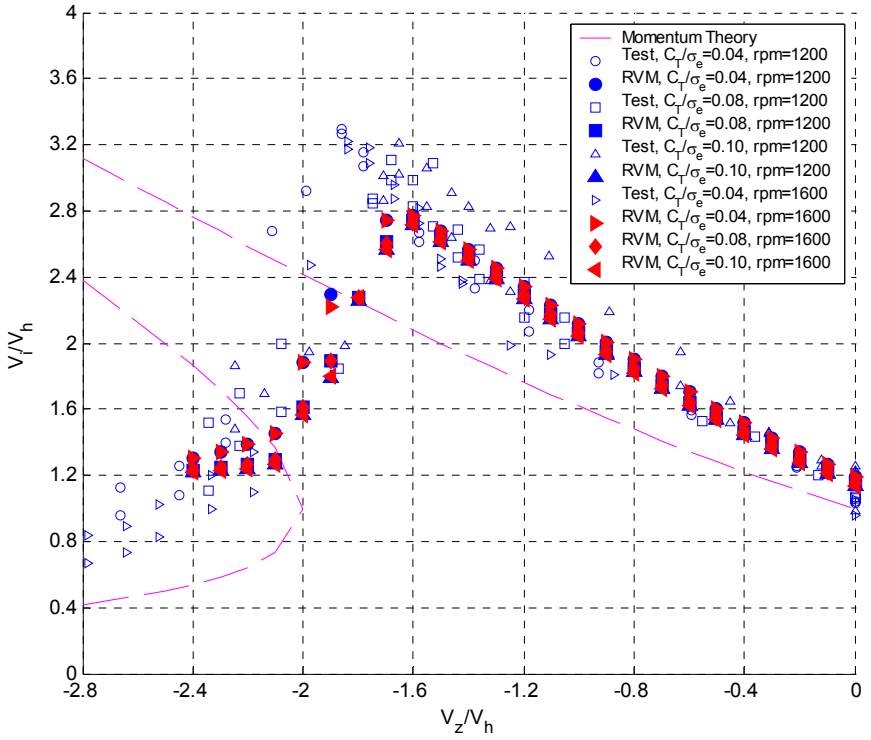

Figure 3.4: Induced velocity variations with Castles and Gray's twisted rotor model: axial flow.

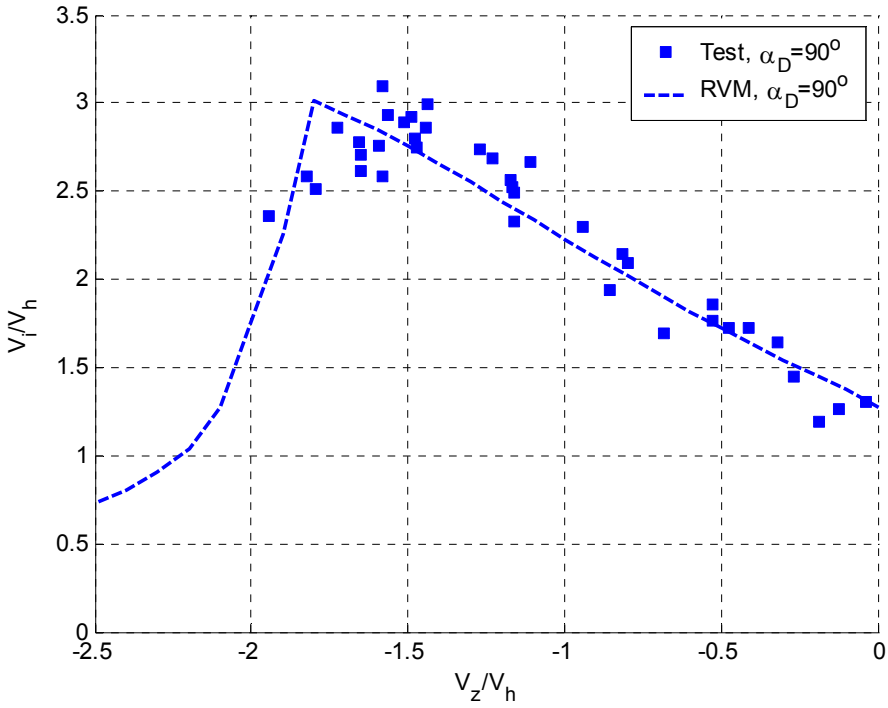

Figure 3.5: Induced velocity variations with Yaggy and Mort's flapping rotor model: axial flow.

phase, the transition phase, and the windmill phase. The results from all four rotor configurations clearly indicate that rotor rotational speed has no significant effect on the variations of induced velocity. This finding is consistent with the conclusion from Ref. [7]. Moreover, comparing between Figure 3.1 (baseline rotor configuration, *R=3 ft*) and Figure 3.2 (reduced-radius rotor configuration, *R=2 ft*), it can be concluded that rotor radius has insignificant influence on the normalized induced velocity. This result also conforms to the finding from Ref. [7]. As both rotor speed and rotor radius have only negligible influence, it is possible to use scaling technique (Froude Scaling or Mach Scaling) to enhance numerical reliability for small-scaled rotor models (including rotary wing UAVs), as indicated in Ref. [32].

In the second validation associated with Yaggy and Mort's experiment, an in-house flapping propeller model is used to predict normalized induced velocity, as shown in Figure 3.5. The comparison is satisfactory between the test data and the predications along the helicopter branch and a portion of the transition phase. Notice that both the test

results and the predictions exhibit a sharp turn at the start of the transition phase. This is because the vortex rings move much quicker above the rotor disk once they pass the accumulation stage near the disk. On the other hand, smaller steps near the η_{peak} during the numerical computation may smooth out the sharp corner. It is also noted that among the selected experiments, Yaggy and Mort's propeller has the highest blade twist (-22.5^o). Due to radial variation adopted in the finite-state inflow model, the ring vortex model is able to account for induced velocity distribution along the blade due to the blade twist.

Heyson compared the experimental results from both Castles and Washizu in terms of induced velocity in axial descent (Ref. [20]). Heyson concluded that while average normalized values from both experiments appeared to be consistent (Figures 4 and 5 in Ref. [20]), Washizu's results showed wider variation of induced velocity. The lower boundary of the variation tended to conform to the momentum theory, while the upper boundary appeared to double the average values from Castles' results. In order to investigate the scattered pattern of induced velocity which appeared in the Washizu's experiment, the number of vortex rings (N_{ring}) is allowed to vary from zero (without vortex rings) to four (two additional vortex rings). With different number of rings, the magnitudes of induced velocities vary around their nominal values, and the scattered pattern is expected to be nonlinear with the increase of descent rate. Predicted induced velocities with varying number of rings are presented in Figure 3.6 to Figure 3.8 with three different collective settings ($\theta_{0.75}$): 8.0^o, 7.5^o, and 4.5^o. Induced velocities calculated with different number of vortex rings are indicated with filled markers of different sizes. In all three figures, the induced velocities predicted with $N_{ring} = 0$ appear to be close to the momentum theory and the lower boundary of the test data. With $N_{ring} = 2$, the calculated induced velocities tend to agree with the average values of the test data. With $N_{ring} = 4$,

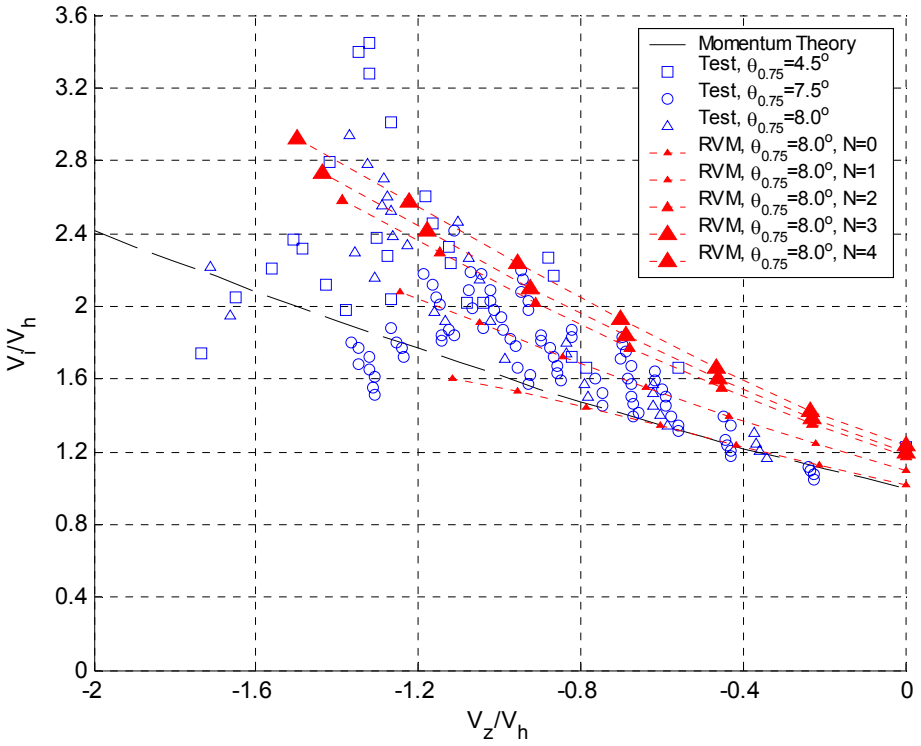

Figure 3.6: Induced velocity variations with Washizu's rotor model: axial flow and $\theta_{0.75}=8.0^{o}$.

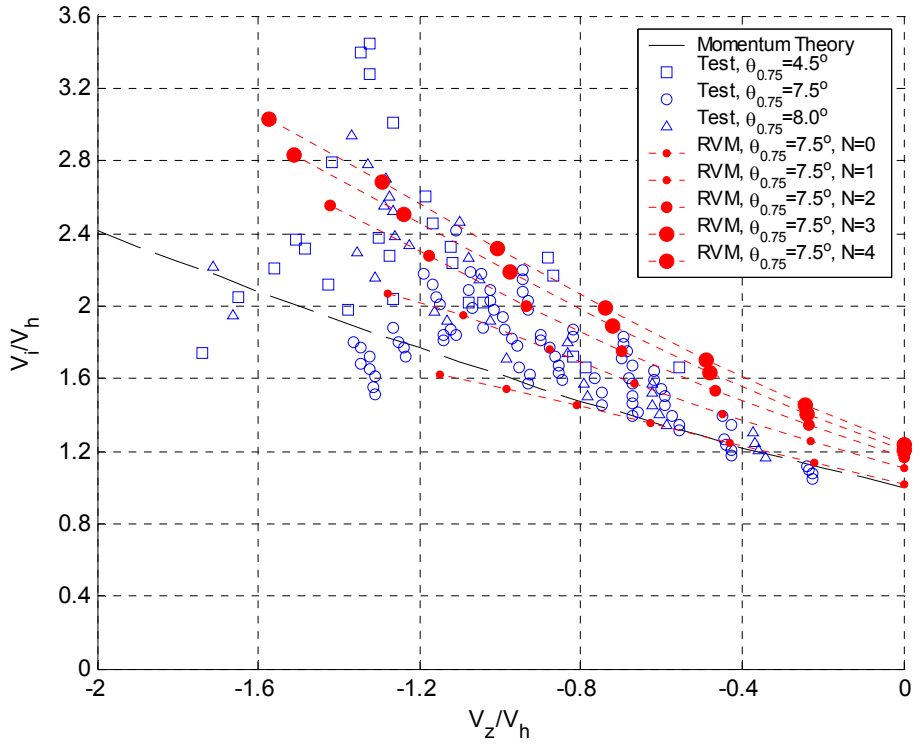

Figure 3.7: Induced velocity variations with Washizu's rotor model: axial flow and $\theta_{0.75}=7.5^{o}$.

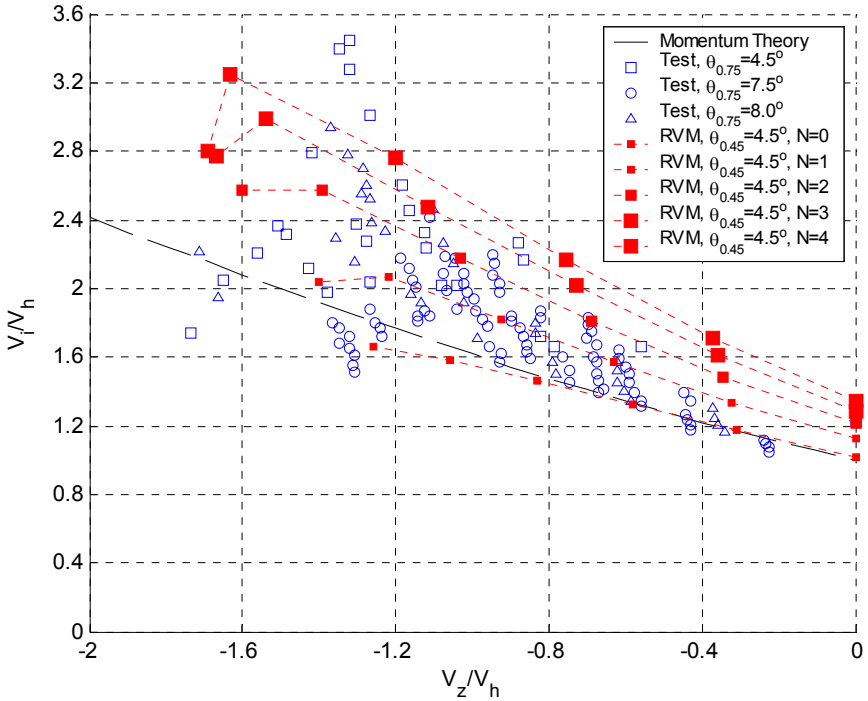

Figure 3.8: Induced velocity variations with Washizu's rotor model axial flow and $\theta_{0.75}=4.5^{o}$.

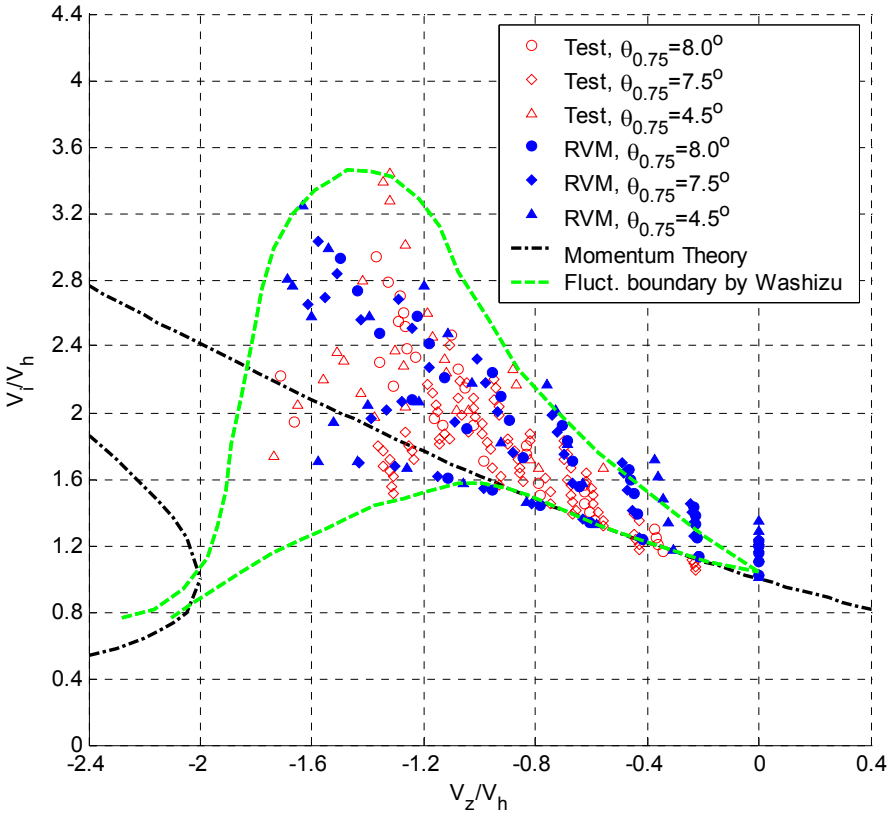

Figure 3.9: Fluctuations of induced velocity with Washizu's rotor model: axial flow.

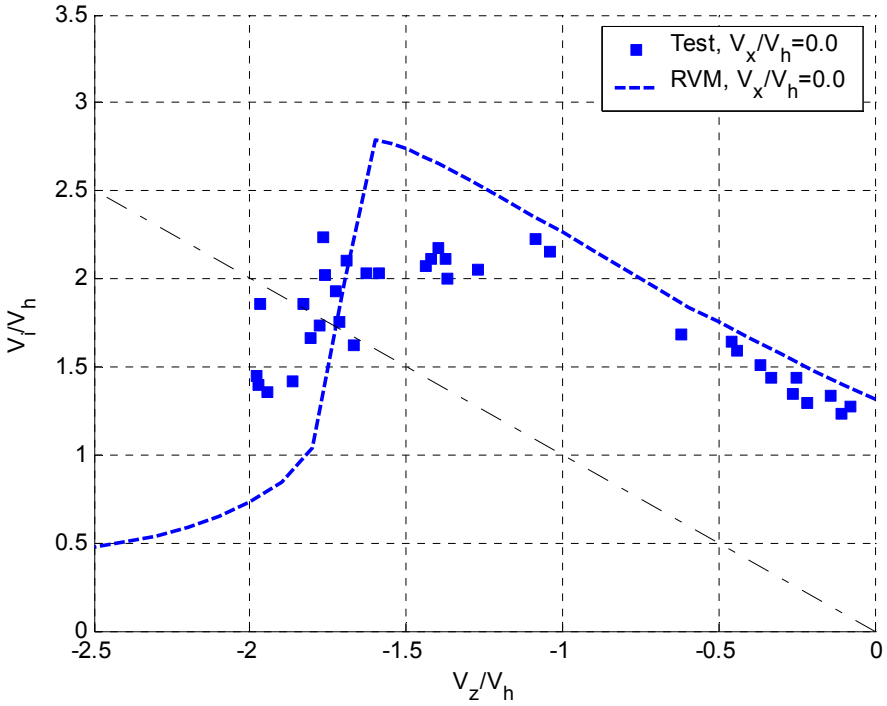

Figure 3.10: Induced velocity variations with Dauphin's main rotor model: axial flow.

the upper boundary of scattered test data correlates well with the prediction, especially over moderate descent rate.

For a further comparison, all test data and predicted induced velocities are plotted together in Figure 3.9. Fluctuation boundary given by Washizu (Ref. [12]) is also included. It is clear that predictions using the ring vortex model with varying number of rings are well within the boundary.

In the last validation, induced velocity predictions using the main rotor model of the Dauphin helicopter are provided in Figure 3.10. The predictions are consistent with the test data, especially in the regions with low and high descent rates. It is also noted that the test data appear to be saturated in the moderate descent regime. Accurate measurements are difficult in this descent region due to complex aerodynamic environment associated with the VRS.

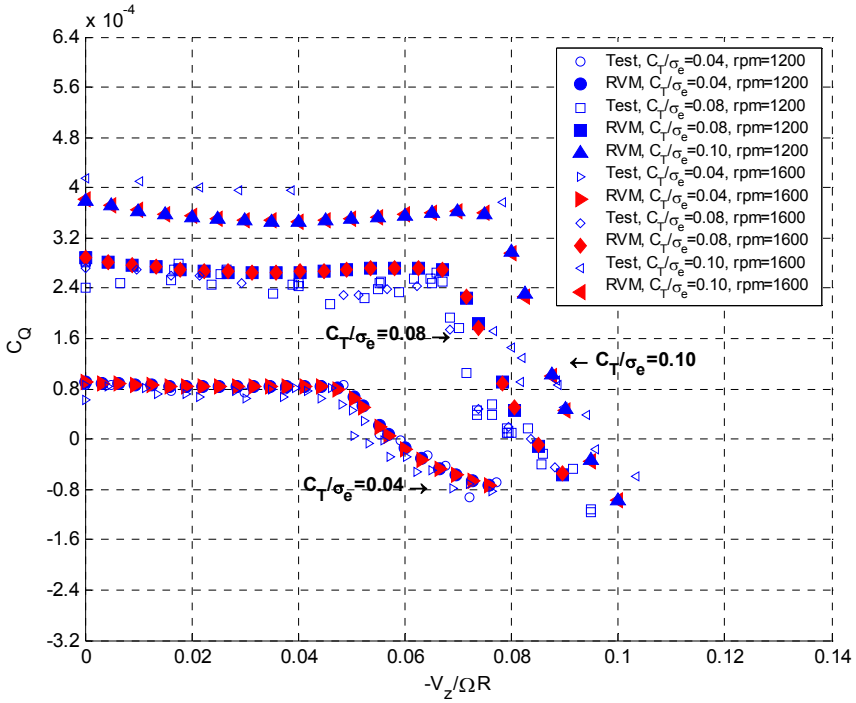

Figure 3.11: Torque coefficient variations with Castles and Gray's baseline rotor model: axial flow.

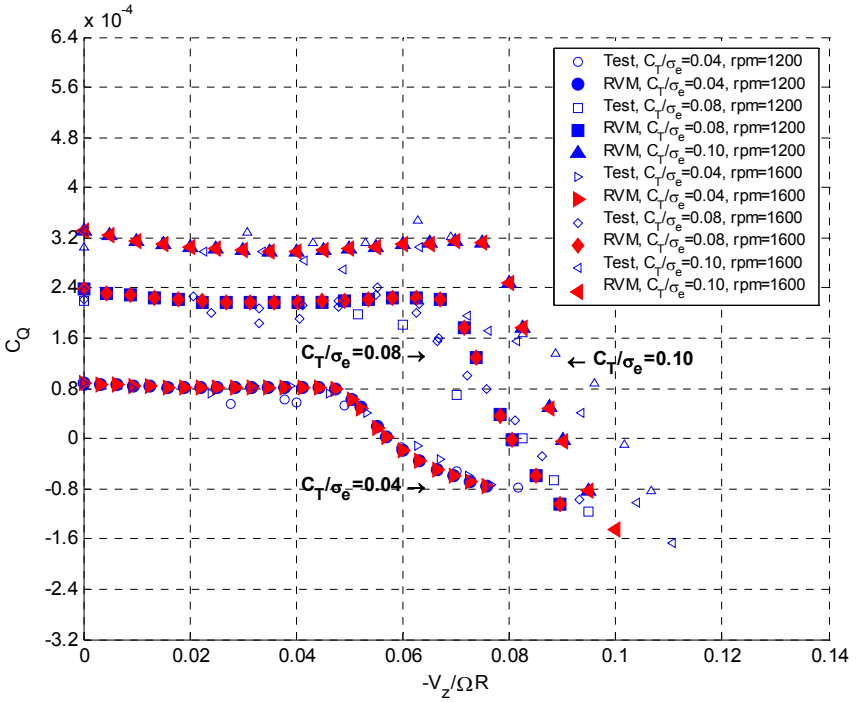

Figure 3.12: Torque coefficient variations with Castles and Gray's reduced-radius rotor model: axial flow.

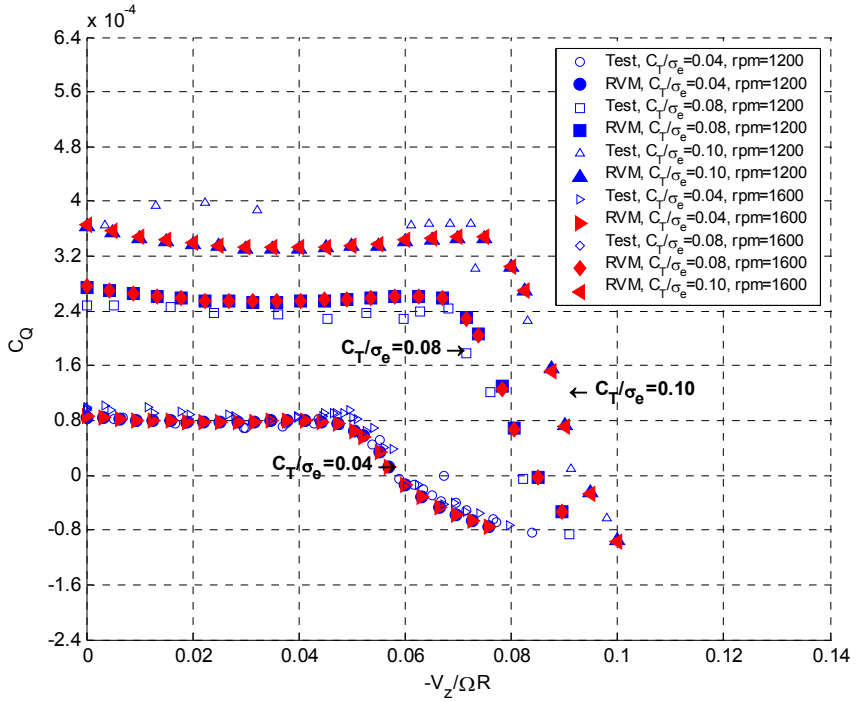

Figure 3.13: Torque coefficient variations with Castles and Gray's tapered rotor model: axial flow.

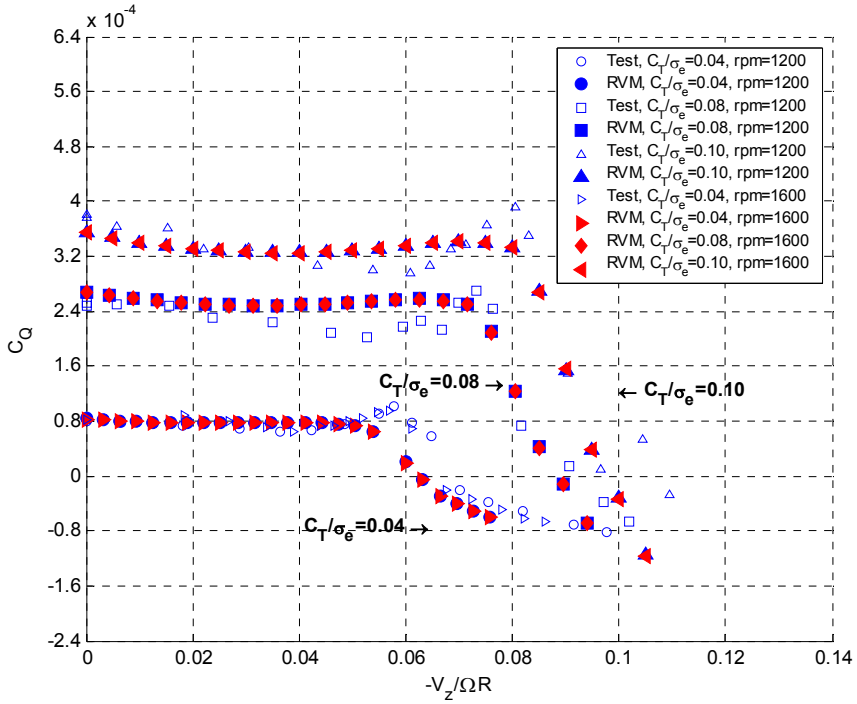

Figure 3.14: Torque coefficient variations with Castles and Gray's twisted rotor model: axial flow.

3.3 Torque Requirement

A rotor may consume more power in descent flight than at hover, a phenomenon known as power settling to pilots. Torque coefficients as a function of descent rate are provided in Figure 3.11 to Figure 3.14, corresponding to four different rotor configurations from Castles and Gray's wind-tunnel tests. Satisfactory agreements between predictions and test data are shown in the four figures. As expected, the rotor requires almost the same or even higher torque as descent rate increases from hover to transition phase. Once the transition phase starts, torque required decreases rapidly. The rotor enters the windmill mode once the value of torque coefficient becomes negative.

3.4 Collective Control Setting

Validation in terms of collective control setting is conducted with Castles and Gray's tests, as shown in Figure 3.15 to Figure 3.18. The required collective control for a given rotor thrust shows a trend similar to that of the torque coefficient. As the rotor starts to descend from hover, the rotor needs to maintain almost constant or even higher values of collective pitch in order to descend further. Once the transition phase starts, there is an immediate reduction in the collective control. At a high descent rate, a negative value of collective control may be required.

3.5 Changes in Thrust and Torque

Variations of induced velocity associated with Washizu's moving track tests have already been shown in Figure 3.6 to Figure 3.8. In those four figures, the number of rings is varied in order to reproduce scattered pattern of induced velocity. Changes in rotor thrust and torque can also be calculated from the same steady state simulation.

Changes in thrust with respect to non-dimensional descent rate ($V_z / \Omega R$) are provided in Figure 3.19. The top plot of the figure corresponds to a collective pitch setting ($\theta_{0.75}$) of 8.0^o, while the bottom plot is for a collective pitch setting of 4.5^o.

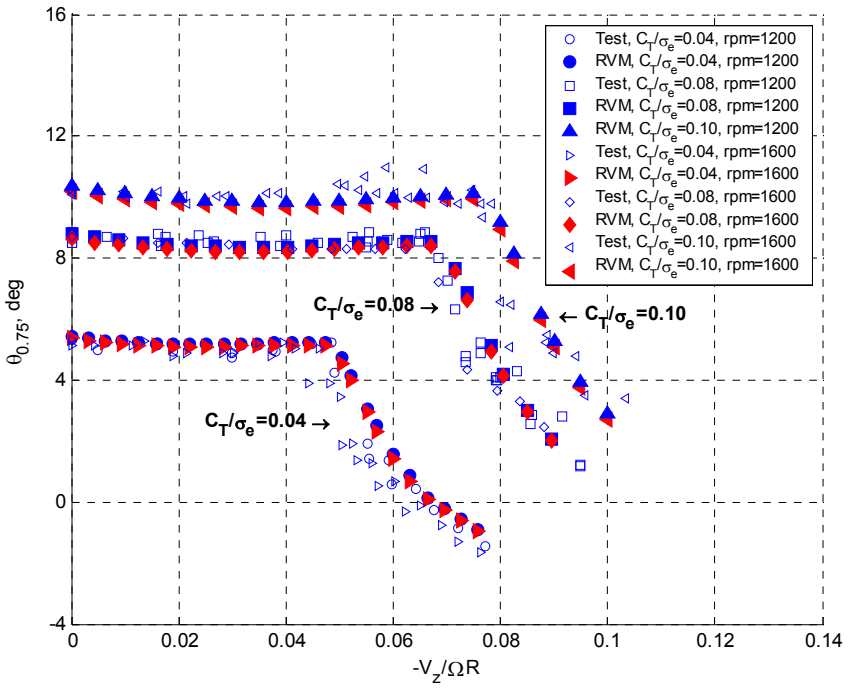

Figure 3.15: Collective control variations with Castles and Gray's baseline rotor model: axial flow.

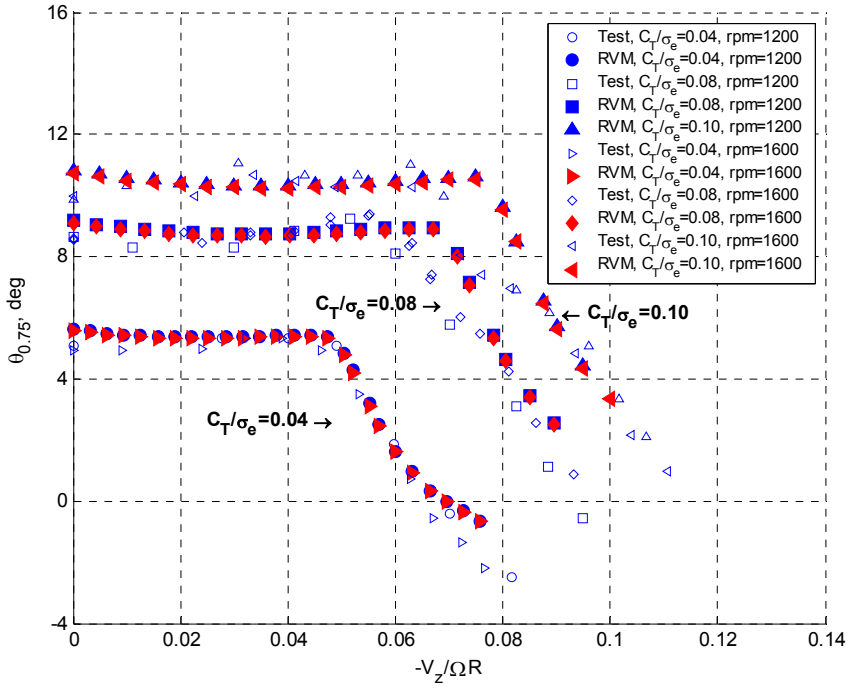

Figure 3.16: Collective control variations with Castles and Gray's reduced-radius rotor model: axial flow.

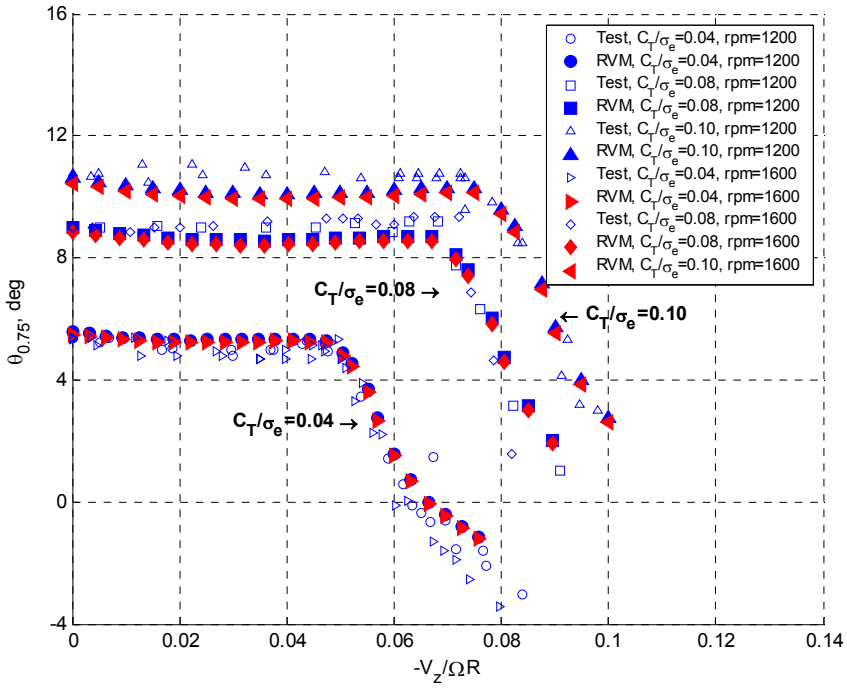

Figure 3.17: Collective control variations with Castles and Gray's tapered rotor model: axial flow.

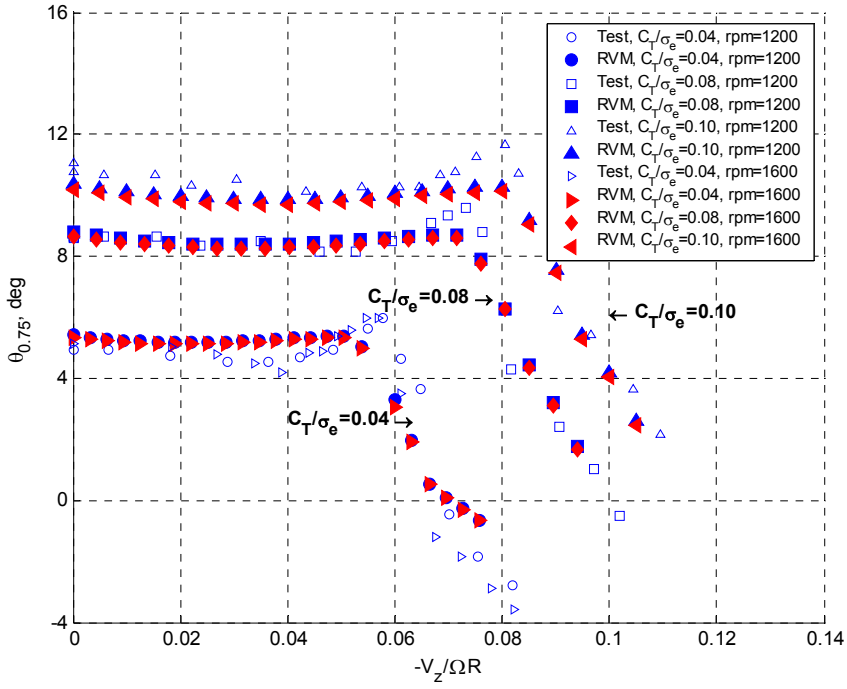

Figure 3.18: Collective control variations with Castles and Gray's twisted rotor model: axial flow.

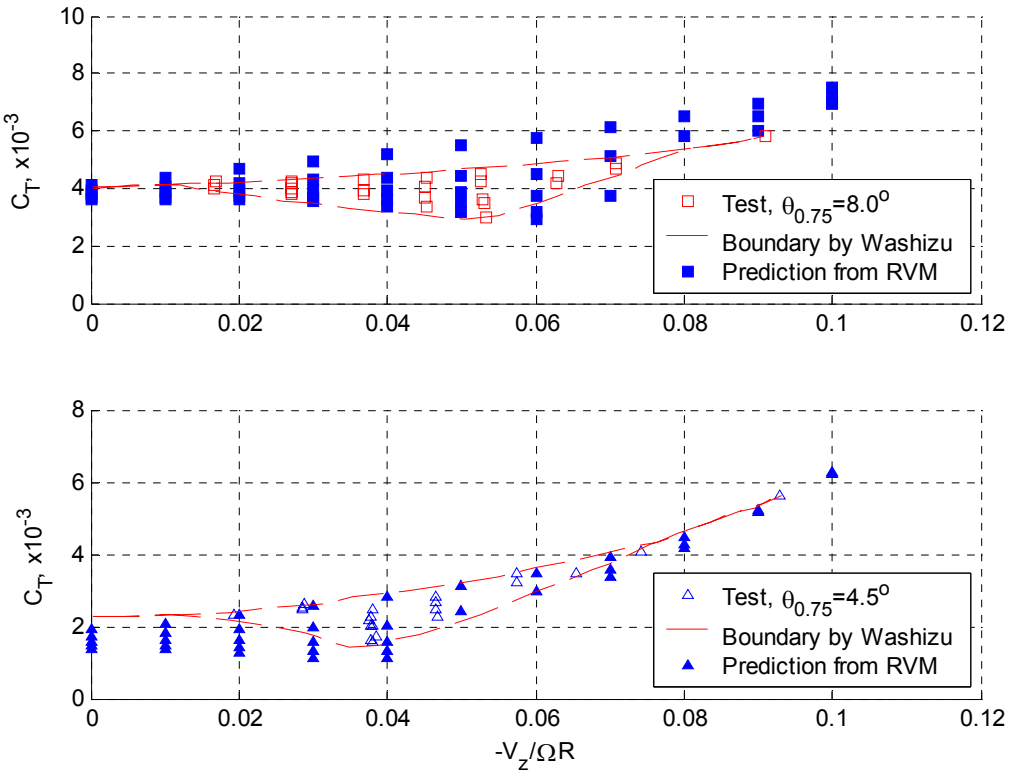

Figure 3.19: Thrust variations with Washizu's rotor model: axial flow.

Measurements from Washizu's experiment are given together with the variation boundary specified by Washizu. Predicted results include steady state thrust and torque with the number of rings varied from zero to four. In Figure 3.19, changes in rotor thrust from both measurements and predictions pick up when the descent rate increases from hover. The maximum magnitude of thrust variations occur at $V_z / \Omega R = 0.05$ with $\theta_{0.75} = 8.0^o$ and $V_z / \Omega R = 0.04$ with $\theta_{0.75} = 4.5^o$. As the rotor moves towards autorotation, thrust variations decrease and eventually disappear. In both cases, the ring vortex model is able to reproduce the pattern of changes in thrust.

In a further study, $\Delta T / T$ is used as an indicator of changes in rotor thrust, where T and ΔT are the mean value of thrust and the amplitude of changes in thrust, respectively. The results are shown in Figure 3.20 with $\Delta T / T$ given as a function of normalized descent rate. Measurements and predictions using the ring vortex model are provided

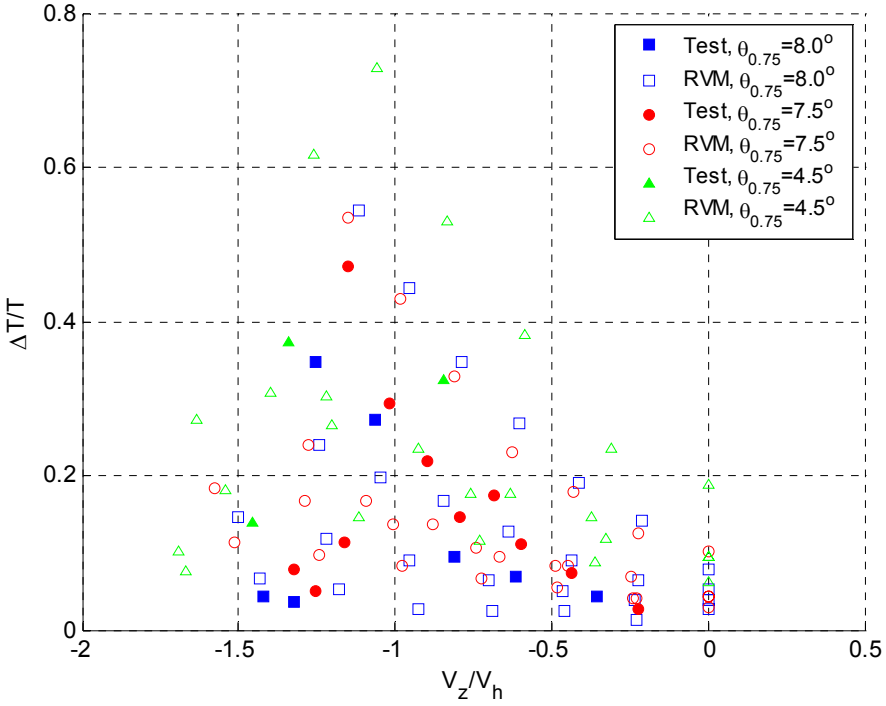

Figure 3.20: Thrust variations *versus* rate of descent with Washizu's rotor model: axial flow.

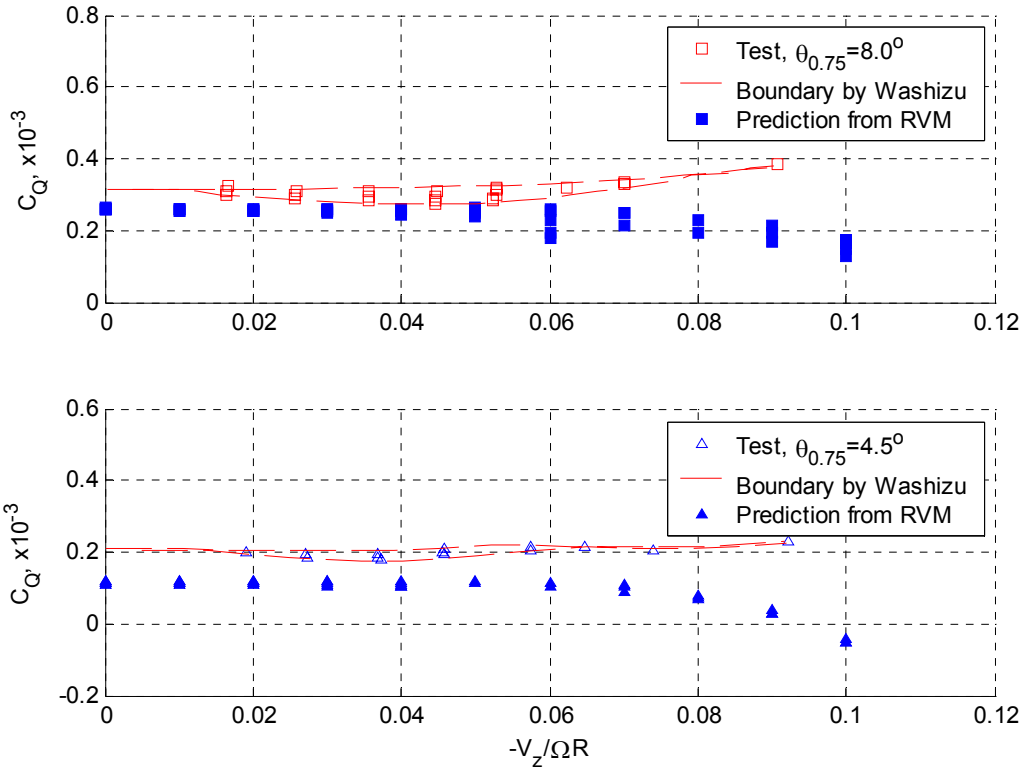

Figure 3.21: Torque variations with Washizu's rotor model: axial flow.

with three different collective pitch settings: 8.0^{o}, 7.5^{o}, and 4.5^{o}. In all cases, the predicted descent rates at which the maximum values of thrust variations occur correlate well with the wind-tunnel data. However, it is also noticed that the maximum magnitudes of thrust changes are over-predicted when using the ring vortex model.

Torque variations versus descent rate are provided in Figure 3.21. From both measurements and predictions using the ring vortex model, rotor torque (and hence power consumption) has much less variations when compared with thrust variations over a wide range of descent rates. This observation is in line with most experiments in the open literature (except perhaps Xin and Gao's whirling beam test, Refs. [14]-[15]). Figure 3.21 also indicates that the predicted torque coefficient drops pre-maturely as the rotor starts to approach the windmill state.

3.6 Effects from Blade Taper, Blade Twist and Rotor Thrust

As mentioned in Chapter 2, it is feasible to investigate the effects from blade taper, blade twist, and rotor thrust with the ring vortex model.

3.6.1 Blade Taper

According to Ref. [7], main effects of blade taper are that it slightly decreases the normalized induced velocity at hover and small rates of descent, and it increases the rate of descent for ideal autorotation by about 3% over that for the rotor with constant-chord blades operating at the same thrust-coefficient. For the convenience of assessment, two inflow curves with and without blade taper are placed together in Figure 3.22. There is a very minor reduction in the predicted induced velocity at hover and small rates of descent for the rotor with blade taper. The predicted descent rate for ideal autorotation increases about 3.55% over the rotor without blade taper. Therefore, using the ring vortex model captures the effect of blade taper.

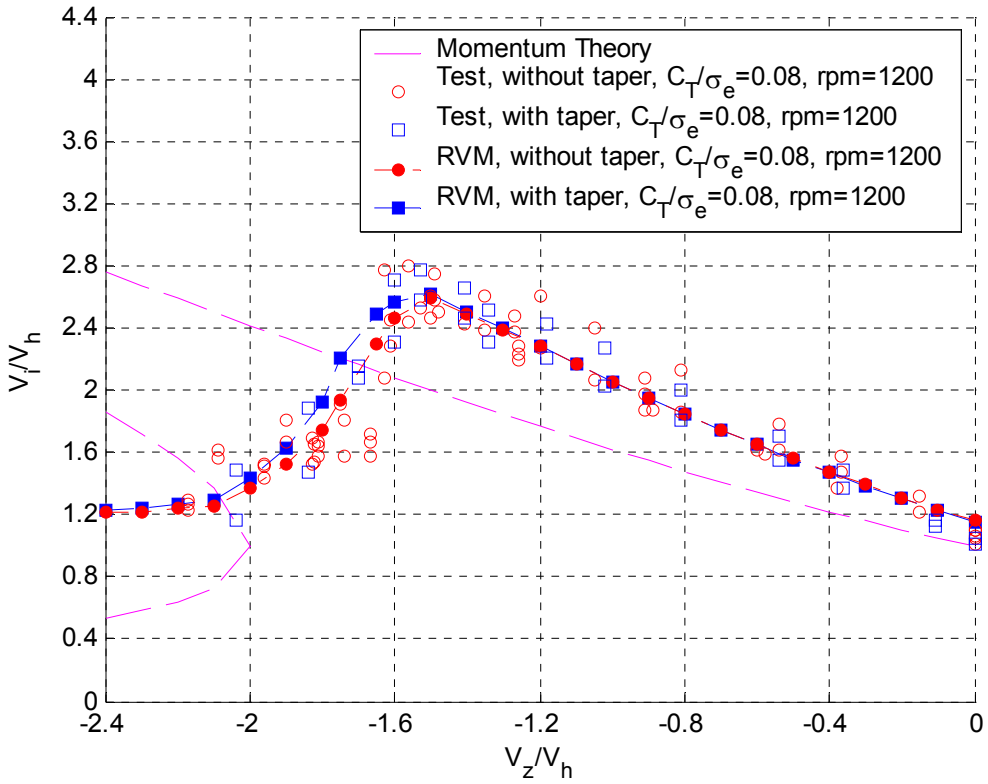

Figure 3.22: Sensitivity study on blade taper.

3.6.2 Blade Twist

A study of blade twist is of particular interest as findings from past studies have been inconclusive. Castles and Gary observed strong effect of blade twist in the wind-tunnel tests (Ref. [7]). An increase of 10% in the rate of descent for ideal autorotation, and an increase of 24% of peak mean induced velocity at 17% higher descent rate were reported. Brown predicted that a rotor with high blade twist was more prone to develop wake instability (Ref. [24]). On the other hand, the V-22 flight test found that the effect from high blade twist is less significant in the establishment of VRS boundary (Refs. [17]-[18]).

In order to analyze the blade twist effect, numerical studies are performed with both Castles and Gray's rotor model and Yaggy and Mort's flapping propeller model. The values of blade twist are -12° and -22.5°, respectively. Figure 3.23 presents two inflow

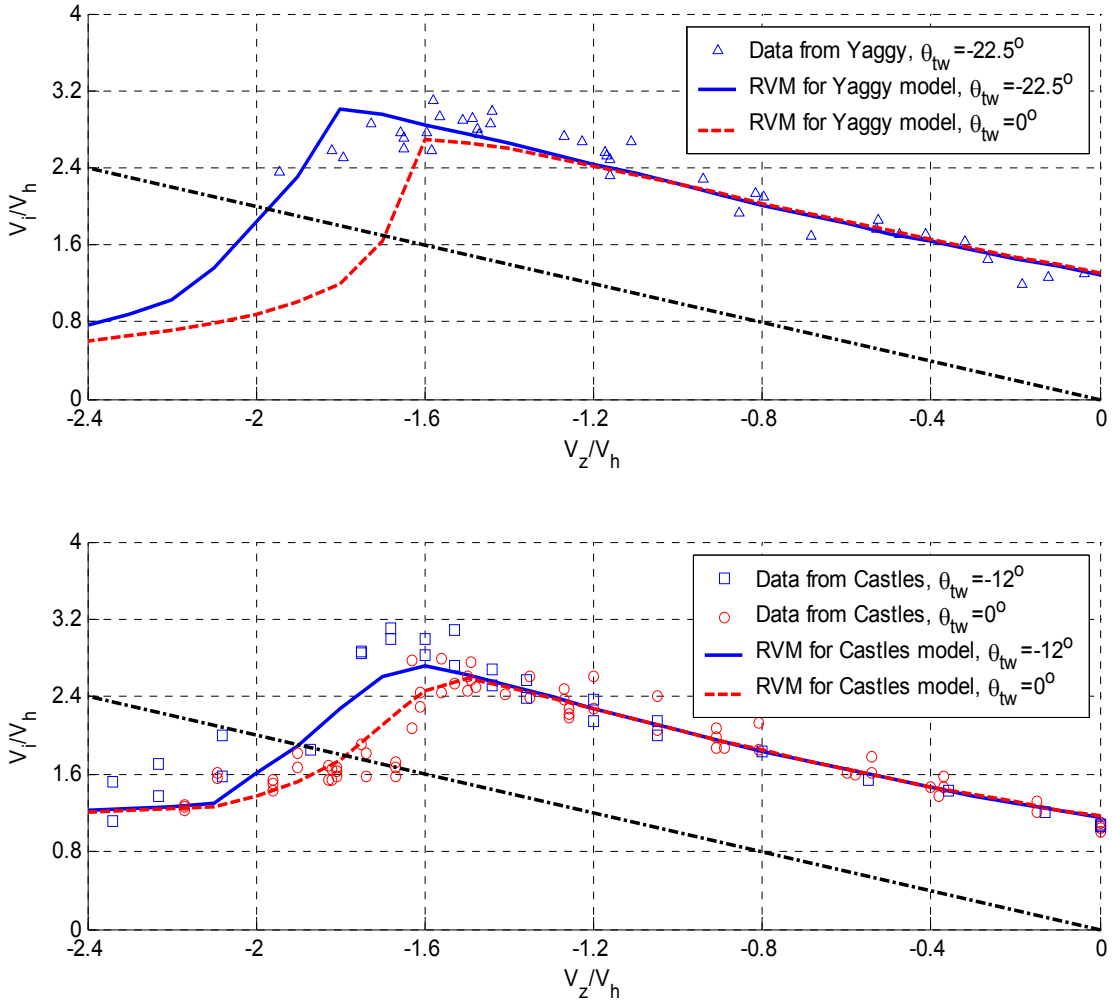

Figure 3.23: Sensitivity study on blade twist.

curves with and without blade twist. When compared with the inflow curve with blade taper in the figure, the predicted inflow curve from Castles and Gary's twisted rotor model has higher peak value of normalized induced velocity and higher normalized descent rate for ideal autorotation. This indicates that the effect of blade twist is stronger than that of blade taper. On the other hand, as compared with the inflow curves with and without blade twist in the bottom plot of Figure 3.23, the predicted increase of descent rate at ideal autorotation is only 7.1% instead of 10% reported by Castles and Gray. The peak normalized induced velocity increases 5.0% at 6.67% higher descent rate due to blade twist. Both values are less than the ones reported in the wind-tunnel tests. It is pointed out in Ref. [8] that Castles and Gray conducted the test in a 9-foot wind-tunnel with a 6-foot rotor model. Facility effects may be significant when examining turbulent environment due to blade twist.

A higher rate of descent for ideal autorotation and a higher peak value of normalized induced velocity are also observed in the case of Yaggy and Mort's experiment. With higher blade twist in Yaggy and Mort's propeller, these two effects appear to be stronger than they are in Castles and Gray's twisted rotor model. This suggests that these two effects tend to grow stronger as blade twist increases.

A more subtle observation is that there is a crossover between the two inflow curves with and without blade twist. Due to blade twist, mean induced velocity across the rotor disk is reduced. This explains that at low descent rates, the inflow curve without blade twist is slightly on top of the inflow curve with blade twist. As the descent rate increases, induced velocity distribution along the blade becomes more and more *uniform* due to the effects from blade twist and vortex rings. At certain descent rate, the mean induced velocities for a twisted blade becomes higher than those for an untwisted blade. Consequently, convection speed of a vortex ring approaches zero at a higher descent rate with a twisted blade, which in turn results in a higher peak value of normalized induced velocity.

3.6.3 Rotor Thrust

Castles indicated in Ref. [7] that there was no significant difference in the inflow curves due to the variations in rotor thrust. Yet it is noticed in Figure 3.1 to Figure 3.4 that a rotor with lower thrust coefficient (or lower disk loading for a given rotor) has slightly higher normalized induced velocity than the rotor with higher thrust coefficient. The average increment on the normalized induced velocity ranges from 6% at hover to 2% at $\eta = -1.5$. The increment results in very minor difference in the slope of the inflow curve. In the ring vortex model, downward velocities at the rotor disk due to vortex rings are affected by the strength of the vortex rings as well as by their distance away from the rotor disk. A smaller thrust coefficient corresponds to weaker vortex ring strength. On the other hand, smaller thrust coefficient gives rise to a slower convection speed, thus resulting in a closer distance of vortex rings from the rotor disk. The effect of rotor thrust is thus a result of two competing factors involving the strength of the vortex rings and their distance away from the rotor disk. The influence from the reduction of convection speed appears to be stronger in the simulation with Castles and Gray's rotors. As a consequence, the inflow curve with smaller thrust coefficient is on top of the curve with larger thrust coefficient.

The impact from thrust coefficient becomes more tangible in terms of thrust oscillation. This is because the difference between inflow curves with the number of vortex rings varying from zero to two is more obvious with a smaller thrust coefficient. For a given rotor, an increase in thrust coefficient thus gives rise to smaller thrust oscillation. Similar observation was reported in Ref. [11].

CHAPTER 4 VALIDATIONS FOR A ROTOR IN INCLINED DESCENT

Further validations of the ring vortex model are considered in inclined descent. Except for Castles and Gray's wind-tunnel tests, the three other experiments described in the last chapter involve non-axial flow and will be further utilized for validations in inclined descent. These experiments include Yaggy and Mort's wind-tunnel tests, Washizu's moving track tests, and ONERA's Dauphin flight tests. Furthermore, the finite-state inflow model with 7 states is selected over the momentum theory in order to include both radial and azimuthal variations.

4.1 Induced Velocity Variations

The first validation involves Yaggy and Mort's flapping propeller. Variations of induced velocity from both measurements and predictions are shown in Figure 4.1. The descent angle (α_D) is varied from 90^o (axial descent) to 30^o in steps of 15^o. In all five cases, predictions using the ring vortex model correlate very well with the experimental data. This successful correlation demonstrates the effectiveness of azimuthal variation in the 7-state inflow model.

In Washizu's experiment, descent angle ranges from 90^o (illustrated in the previous chapter) to 20^o. Test results and predictions from both the momentum theory and the ring vortex model are provided from Figure 4.2 to Figure 4.4. A summary of the results are also given in Figure 4.5. In the numerical simulation, the number of rings is allowed to vary from zero to four. Observations can be made in the following:

- When the number of rings is zero, predictions using the ring vortex model are close to the momentum theory and the lower boundary of test data;

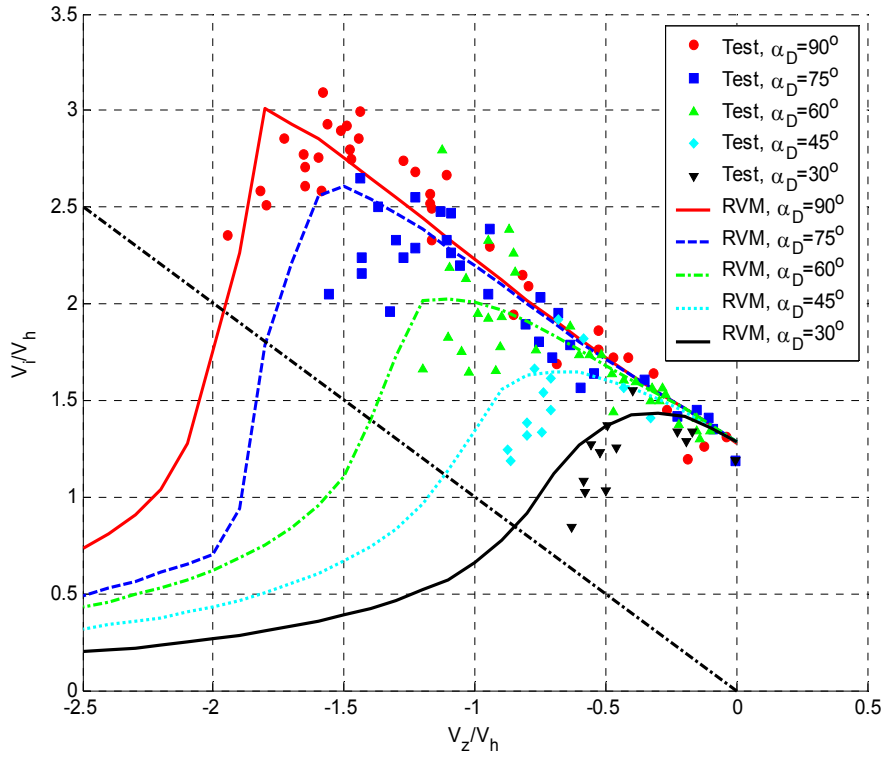

Figure 4.1: Induced velocity variations with Yaggy and Mort's flapping rotor model: axial and non-axial flow.

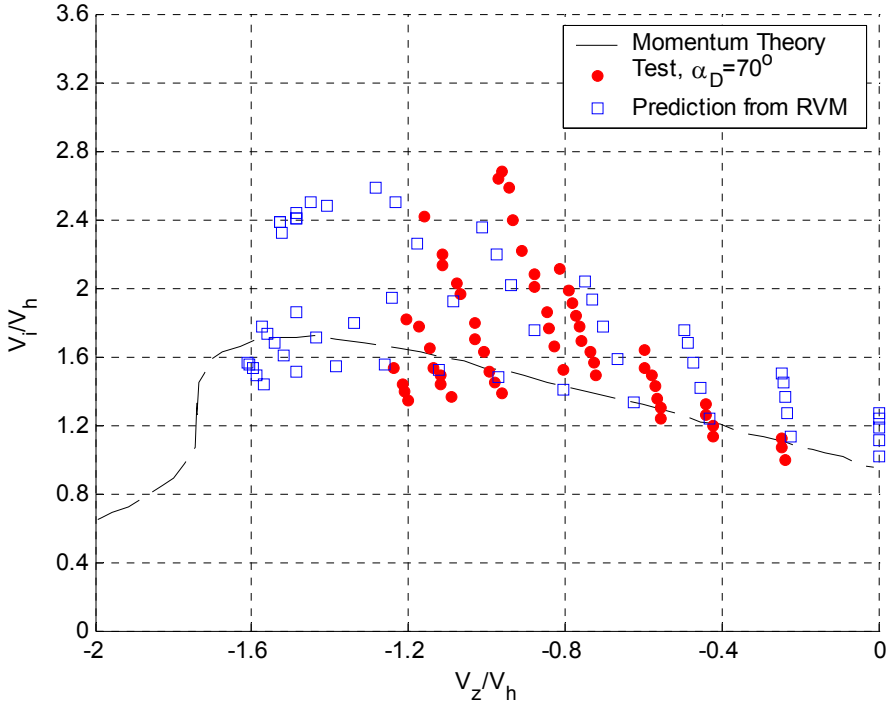

Figure 4.2: Induced velocity variations with Washizu's rotor model: non-axial flow and α_D=70°.

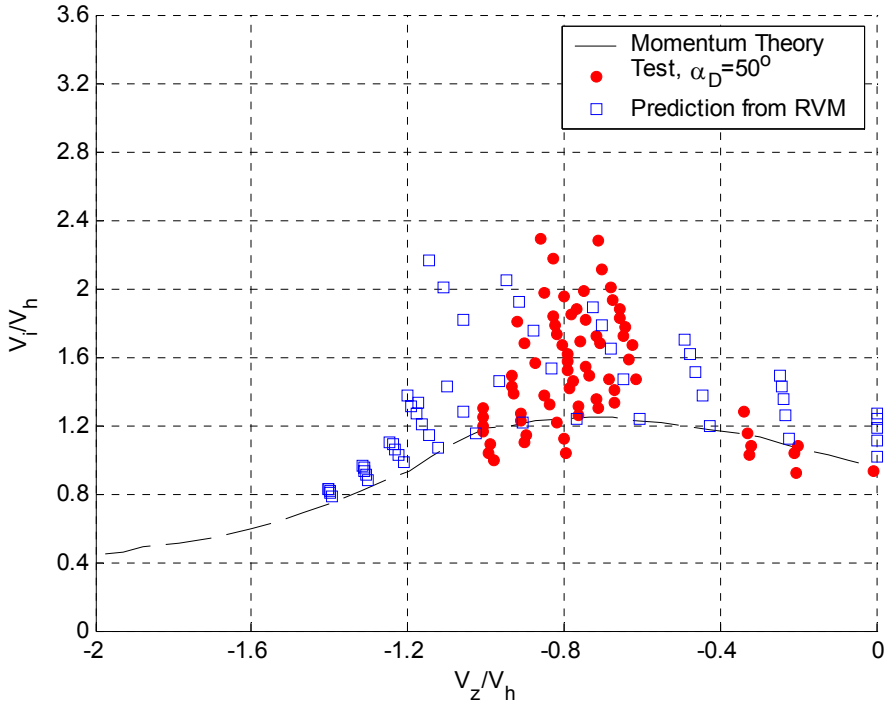

Figure 4.3: Induced velocity variations with Washizu's rotor model: non-axial flow and α_D=50°.

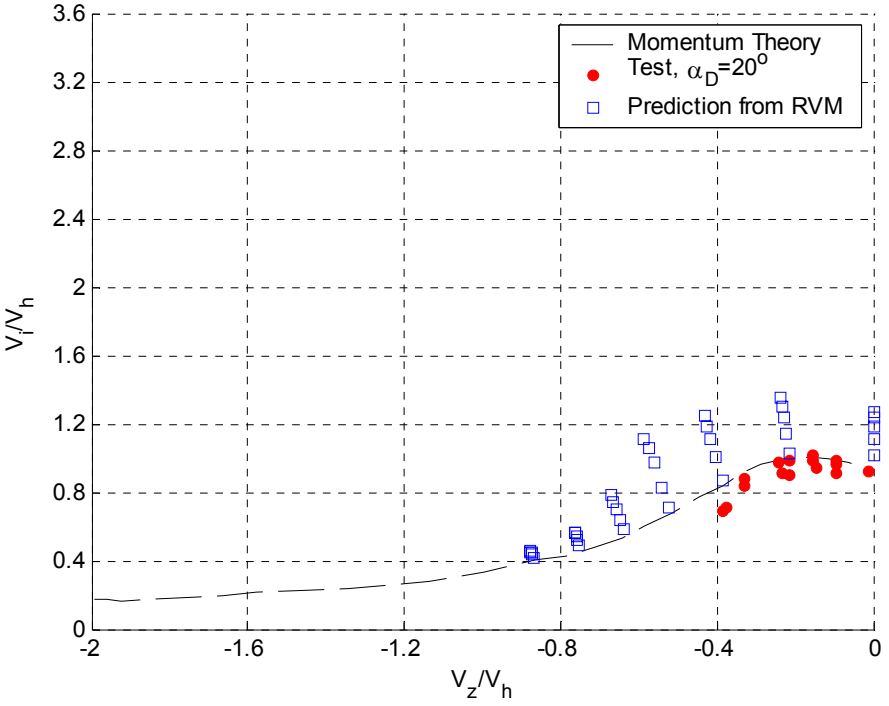

Figure 4.4: Induced velocity variations with Washizu's rotor model: non-axial flow and α_D=20°.

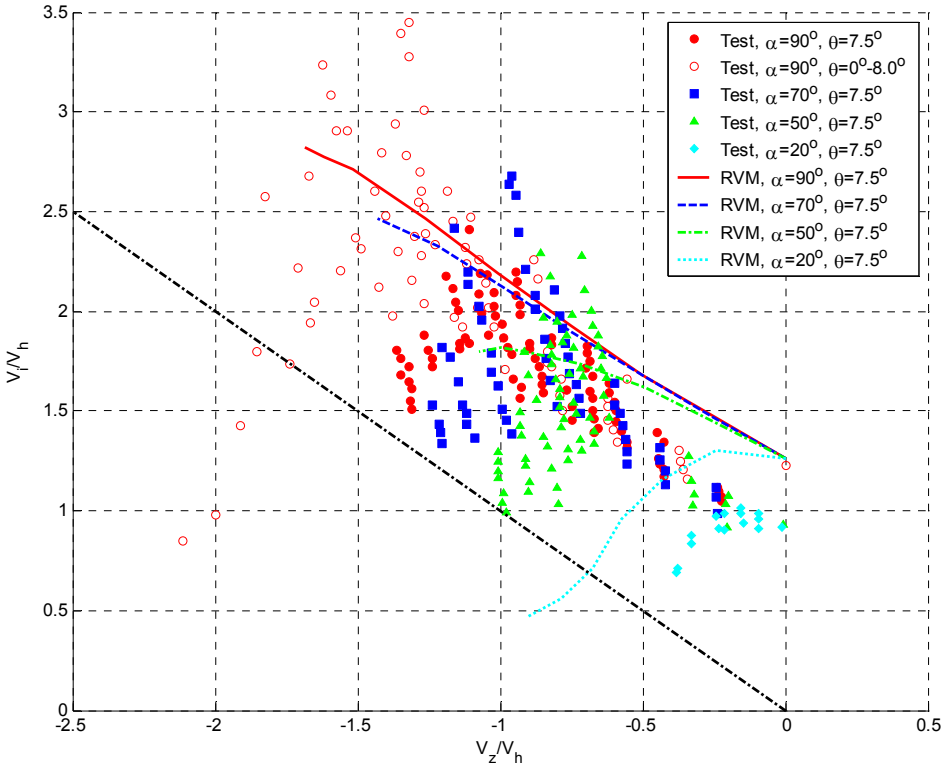

Figure 4.5: Induced velocity variations with Washizu's rotor model: axial and non-axial flow.

- When the number of rings is four, the maximum values of predicted induced velocity have similar magnitude as test data in the cases of $\alpha_D = 70^o$ and $\alpha_D = 50^o$. When $\alpha_D = 20^o$, the maximum value is slightly over-predicted. This indicates that the vortex rings may be swept faster than expected once VRS is cleared in the flight;
- As descent angle decreases, so does fluctuation of induced velocity. In fact, when $\alpha_D = 20^o$, the fluctuation almost disappears.

The third validation involves ONERA's Dauphin main rotor model. The flight tests were conducted with forward velocity (V_x / V_h) fixed at 0.0, 0.23, 0.69, 0.92, 1.16, and 1.85. Predictions using the ring vortex model are shown in Figure 4.6. Generally, results using the ring vortex model agree well with the test data. This suggests that the ring vortex model is able to cover a wide range of descent flight.

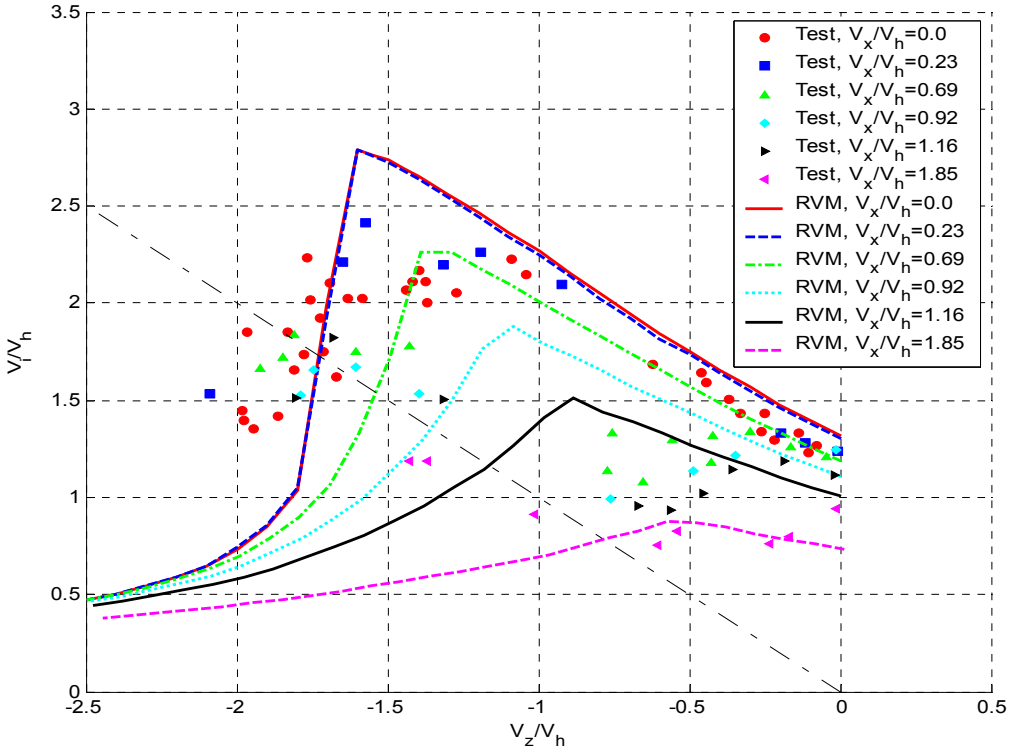

Figure 4.6: Induced velocity variations with Dauphin's main rotor model: axial and non-axial flow.

4.2 Changes in Rotor Thrust

This section is a continuation of discussion on steady state thrust variations with Washizu's rotor model. In Section 3.5, steady state changes in rotor thrust were studied for axial descent with $\alpha_D = 90^o$ as the number of vortex rings varied from zero to four. In the case of non-axial flow, the angle of descent (α_D) is selected as 70°, 50°, and 20°. Test results and predictions using the ring vortex model are shown in Figure 4.7 to Figure 4.9. Again, the number of rings in the numerical investigation is allowed to vary from zero to four to reproduce the variations in rotor thrust. When $\alpha_D = 70^o$ and $\alpha_D = 50^o$, the ring vortex model is able to capture the maximum magnitude of $\Delta T / T$. There is a slight offset in terms of the normalized descent rate at which the maximum magnitude of $\Delta T / T$ occurs. When $\alpha_D = 20^o$, both test results and predictions show diminished thrust variations.

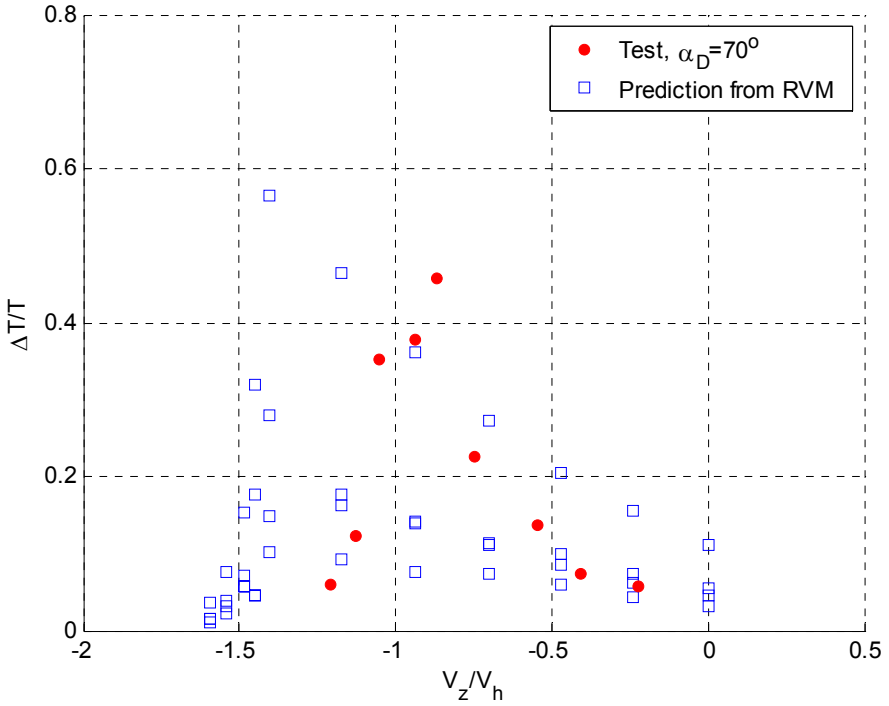

Figure 4.7 Thrust variations with Washizu's rotor model: non-axial flow with α_D=70°.

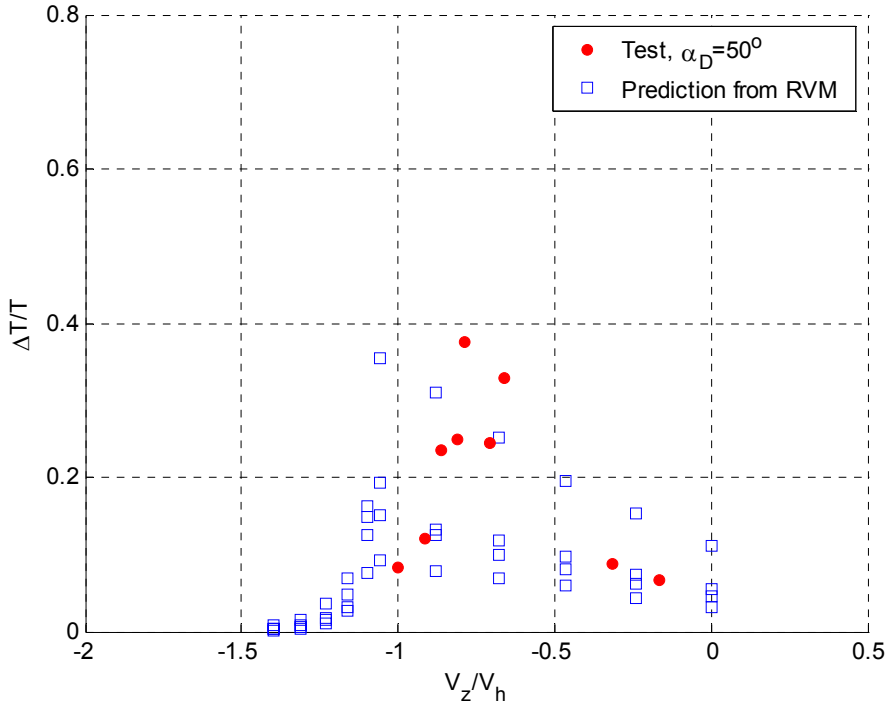

Figure 4.8: Thrust variations with Washizu's rotor model: non-axial flow with α_D=50°.

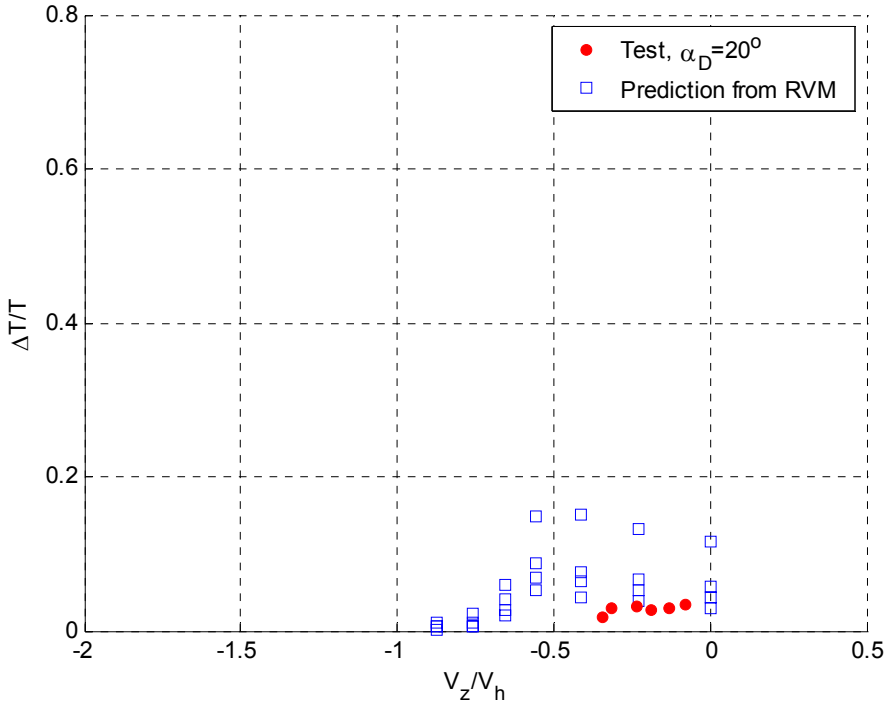

Figure 4.9: Thrust variations with Washizu's rotor model: non-axial flow with α_D=20°.

CHAPTER 5 APPLICATION TO A SINGLE MAIN-ROTOR HELICOPTER

While routine operations of a helicopter in the VRS are restricted, a better understanding of the VRS problem and an ability to accurately predict the VRS boundary provide certain advantages. For example, a detailed understanding of the VRS problem may lead to the development of an automated system for VRS avoidance. Also, the ability to accurately predict the VRS boundary may lead to a better utilization of the safe operational envelope to facilitate significant noise abatement, e.g., through segmented steep approaches for civilian helicopters.

In this chapter, a historical review of various VRS boundaries is provided. Subsequent numerical investigations focus on the prediction of the VRS boundary for the Dauphin helicopter. Since the Dauphin VRS boundary is primarily defined by uncommanded drop in descent rate, heave stability criterion becomes a natural choice to determinate the VRS boundary. An in-house Dauphin flight dynamic model is formulated and simulations are carried out to predict the Dauphin VRS boundary.

5.1 Review of VRS Boundaries

Over the years, a number of criteria for arriving at VRS boundaries have been proposed. Some criteria are more aerodynamics-based. These include region of roughness, thrust and torque fluctuations, mean thrust reduction, tip vortices, wake breakdown, and vibration. Other criteria such as bifurcation, heave and roll stability are more flight dynamics-based.

The most common way of displaying a VRS boundary is to use free stream velocity components, V_x and V_z, normalized by hover induced velocity V_h. The area within the VRS boundary indicates that the effects of VRS are significant in terms of the chosen

criterion. Another commonly used variable in the VRS boundary is the descent angle (α_D) with $\alpha_D = 90^o$ representing axial descent. A summary of VRS boundaries from previous studies is included in Figure 5.1. What follows is a brief description of the various criteria that have been used by the researchers in arriving at the VRS boundaries shown as subplots in Figure 5.1.

Region of Roughness

Drees identified a region of roughness from the investigation of a helicopter in VRS (Ref. [43]). In this region, the helicopter behavior was rough with respect to attitude and control. Unexpected loss of altitude and extreme nose-down pitching motion were also observed. The region of roughness ranged from $V_z / V_h = -0.62$ to $V_z / V_h = -1.53$ in axial descent, extending in inclined descent to $V_x / V_h = 1.0$.

Thrust Fluctuations

Washizu derived the VRS boundary based on rotor thrust fluctuations (Ref. [12]). The VRS boundary was determined from the magnitude of $\Delta T / T$ with two reference values set at 0.15 and 0.30. When $\Delta T / T = 0.15$, the corresponding boundary extended from axial descent to inclined descent with a forward velocity component of $V_x / V_h < 1$. When $\Delta T / T = 0.30$, the corresponding boundary mainly covered the inclined descent region with descent angle ranging from 45^o to 80^o.

Wolkovitch Criterion

As illustrated in Chapter 1, Wolkovitch proposed a flow model consisting of a slipstream with uniform flow at any section of the rotor surrounded by a protective tube of vorticity (Ref. [19]). The tube was made up of tip vortices leaving the rotor. Wolkovitch postulated that unsteady vortex ring flow was associated with a breakdown of this protective tube of vorticity. Consequently, the entry of VRS occurred when the net

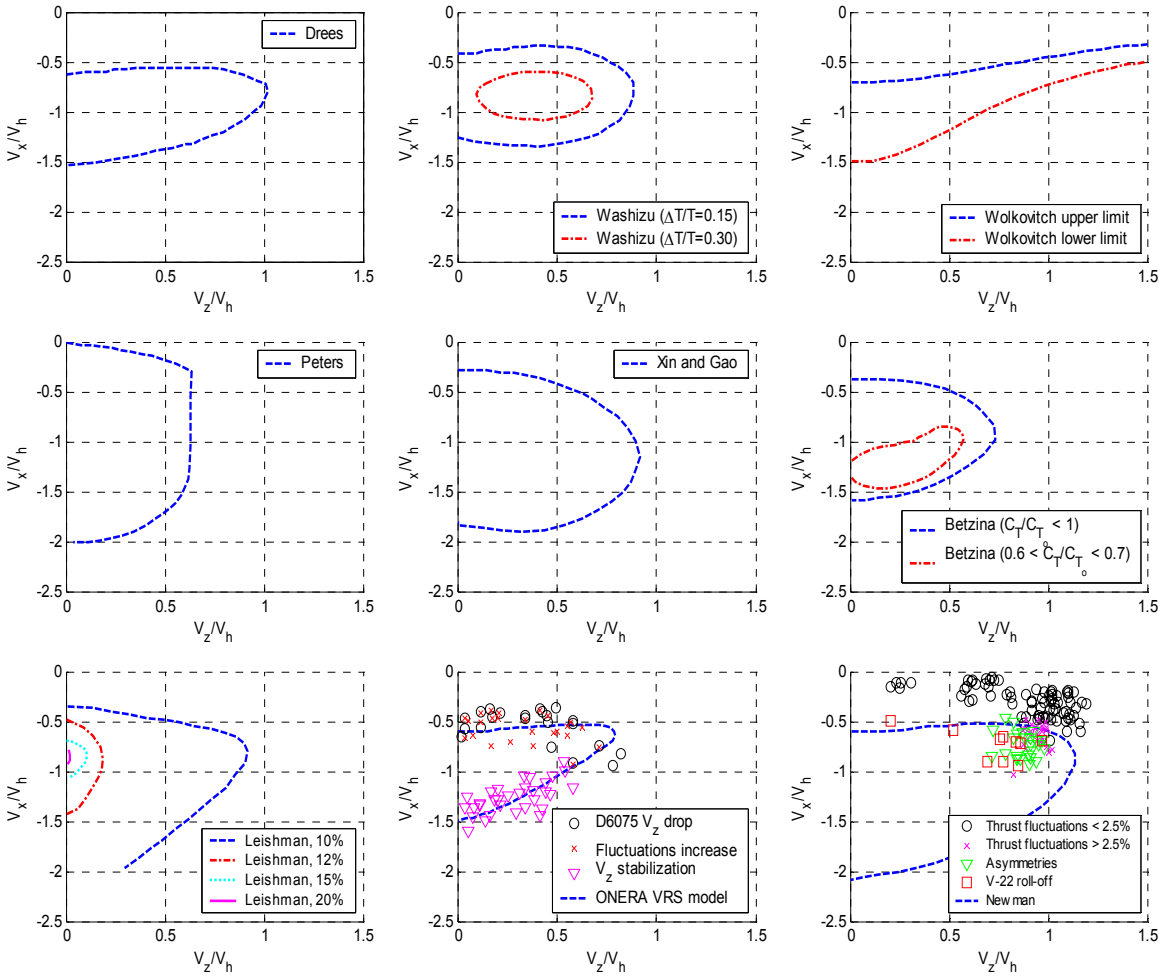

Figure 5.1: A historical review of VRS boundaries.

velocity of tip vortices became zero:

$$V_Z = -\frac{V_i}{2} \tag{5.1}$$

As to the VRS departure, a coefficient k_z was utilized to take into account the distance above the rotor where the vorticity would accumulate:

$$V_Z = -\frac{k_z V_i}{2}, 1 \le k_z \le 2 \tag{5.2}$$

A value of 1.4 was suggested for k_z by Wolkovitch. According to Ref. [9], Wolkovitch's boundaries were close to experimental data at low forward speed. Nevertheless, the boundaries were not consistent with experiments at high forward velocities.

Peters modified Wolkovitch's method by removing several inconsistencies in the flow model and taking into account the wake skew angle (Ref. [38]). After modification, Peters' boundary showed no VRS for $\mu > 0.62$ and predicted VRS over a wider range of V_z / V_h.

Torque Fluctuations

Xin and Gao observed irregular variations of the rotor torque at about $V_z / V_h = -0.28$ (Refs. [14]-[15]). Torque fluctuations were more severe for $\alpha_D = 60^o$ and $\alpha_D = 75^o$ than in axial descent. As the descent angle decreased, torque fluctuations also diminished and finally disappeared below $\alpha_D = 40^o$.

Based on observations from the experiment, Xin and Gao pointed out that there were three problems associated with Peters' VRS boundary. First, Peters' boundary showed that the rotor entered VRS even at small descent rates. Second, no occurrence of VRS existed for $\mu > 0.62$. Third, VRS occurred at every descent angle.

Xin and Gao thus proposed an improved VRS boundary as shown in the subplot of Figure 5.1. The boundary was more consistent with experimental results.

Mean Thrust Reduction

Betzina observed a significant mean thrust reduction in VRS (Ref. [16]). As a result, thrust ratio C_T / C_{T_o} was used as an indicator, where C_T and C_{T_o} represented the mean thrust coefficient and the thrust coefficient at hover, respectively. It was shown that the lowest thrust ratio centered at about $\alpha_D = 75^o$ and $V_x / V_h = 0.3$, and extended from $\alpha_D = 60^o$ to $\alpha_D = 90^o$.

Blade Flapping Fluctuations

The free-vortex wake method was applied in the VRS study by Leishman (Ref. [44]). Besides thrust and torque fluctuations, it was suggested that blade flapping fluctuations may also be a concern as a result of unsteady airloads found near or in the VRS. An excessive blade flapping angle (greater than 10% of the mean) may lead to piloting difficulty. As such, contours of blade flapping fluctuations were obtained.

Newman Criterion

Newman developed a wake transport criterion for VRS assessment (Ref. [45]). An effective wake transport velocity was defined as follows:

$$\overline{\mu}_{WTVE} = \sqrt{k^2 \overline{\mu}_x^2 + (\overline{\mu}_z + \overline{\lambda}_i)^2} \tag{5.3}$$

where *k* represented relative effectiveness of an in-plane velocity component compared to a normal velocity component. A critical value of $\overline{\mu}_{WTVE}$ existed, indicating an onset of flow breakdown in the wake stream tube, denoted as $\overline{\mu}_{WTVECRIT}$. The true wake transport velocity at this critical condition can be expressed with respect to the effective velocity:

$$\overline{\mu}_{WTV} = \sqrt{\overline{\mu}_{WTVECRIT}^2 + (1 - k^2)\overline{\mu}_x^2} \tag{5.4}$$

On the other hand, the mean induced velocity $\overline{\lambda}_i$ was represented as

$$\overline{\lambda}_i = \frac{1}{\overline{\mu}_{WTV}} \tag{5.5}$$

Thus, the boundary for the onset of flow breakdown was given by:

$$\bar{\mu}_z = \pm\sqrt{\bar{\mu}_{WTVECRIT}^2 - k^2\bar{\mu}_x^2} - \bar{\lambda}_i \tag{5.6}$$

Based on experimental observations from Drees (Ref. [43]), Newman selected values of empirical factors as $k = 0.65$ and $\bar{\mu}_{WTVECRIT} = 0.74$.

Heave Stability

During the ONERA Dauphin flight tests, several behaviors were observed, especially in the VRS region (Ref. [9]). During the phase leading to VRS, the crew first felt an increased level of vibration, followed by a sudden decrease in the rate of descent. Increasing the collective did not prevent the helicopter from further descent. During the descent, the helicopter was very unstable and hard to control. The flight tests also established that the VRS effects disappeared beyond a certain forward velocity. The final VRS boundary was determined based on three criteria: (1) Increased level of vibration; (2) Starting of sudden drop in the descent rate; (3) Exit by stabilization of descent rate.

Taghizad also described how the flight procedures were established to determine the VRS boundary (Ref. [9]). First, the forward speed was kept at constant while the collective was progressively reduced. Each moderate collective reduction led to a gentle decrease in descent rate. Then, after some time, a sudden increase in the descent rate would occur. The procedure was repeated for different forward velocities, determining the upper limit of the VRS boundary. In the second procedure, the descent rate was fixed while the forward velocity was gradually decreased until a high level of vibration occurred, indicating the entrance of VRS. Repeating this procedure determined the lower limit of the VRS boundary.

Roll Stability

During the steep descent tests of the V-22 tilt-rotor aircraft (Refs. [17]-[18]), an increase of thrust fluctuations was observed. Subsequently, asymmetries in the rotor

behavior occurred; particularly in an increase in differential thrust error. As the situation degraded, pilot experienced uncommanded roll response. The VRS boundary was defined primarily by this roll-off response. For comparison, Newman's VRS boundary was superimposed with V-22 test data in the subplot of Figure 5.1. It was found that the VRS boundaries between the tilt-rotor aircraft and the conventional helicopter were remarkably similar.

Bifurcation

Bifurcation theory is a nonlinear analysis tool that deals with multiple equilibrium points for a nonlinear dynamical system. As an illustration of the multiple equilibrium points for a helicopter in descent flight, a typical variation of descent rates with respect to collective pitch from ONERA is shown in Figure 5.2 (Ref. [37]). Note that a selected value of collective pitch may correspond to three different values of descent rate. In the figure, the helicopter and windmill branches of the equilibrium curve are stable whereas the curve in between these two branches is unstable. The connection points between stable and unstable parts on the equilibrium curve are called bifurcation points. In the bifurcation criterion, bifurcation points are identified for the generation of the VRS boundary.

ONERA has developed a rotorcraft modeling and simulation software package called HOST (Helicopter Overall Simulation Tool). HOST makes use of Newton-Raphson method as trim algorithm. Nevertheless, as described in Ref. [32], classical Newton-Raphson method is not efficient in predicting possible multiple equilibrium points. For this reason, ONERA developed an in-house nonlinear analysis tool ASDOBI (Analyse des Systèmes Différentiels Ordinaires par la méthode des BIfurcations). With ASDOBI, ONERA is able to predict a VRS boundary based on bifurcation criterion using the HOST flight dynamic model of the Dauphin helicopter.

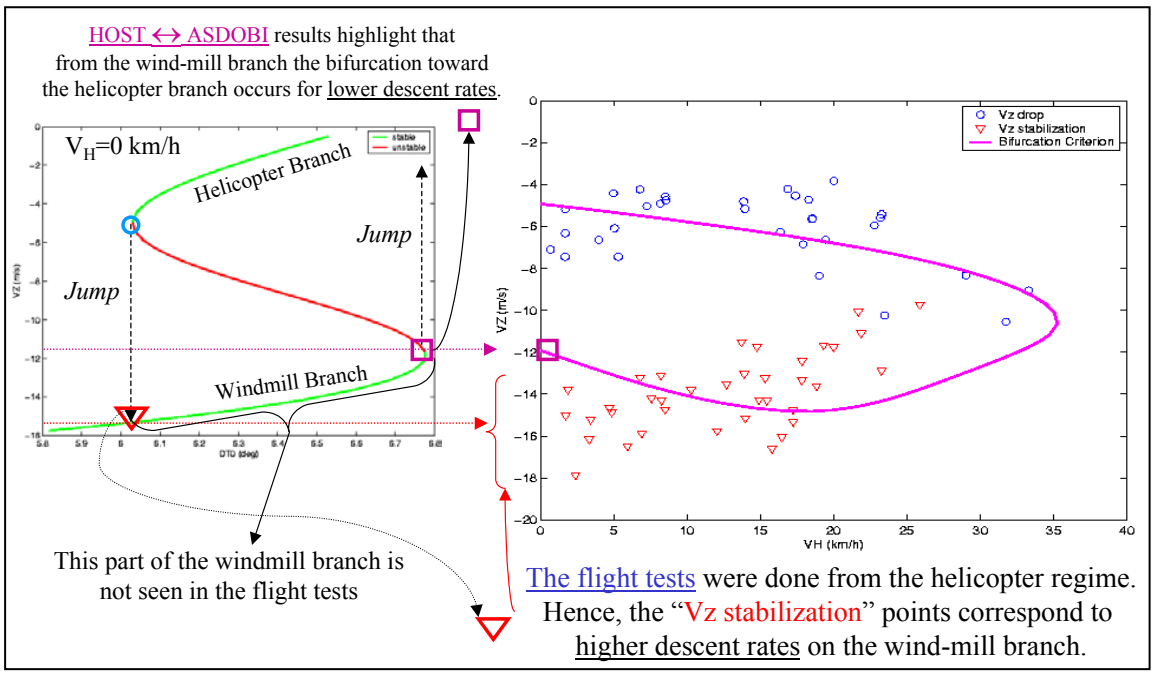

Figure 5.2: An example of multiple equilibrium points from dynamic study with HOST+ASDOBI coupling (Ref. [37]).

According to Ref. [37], during the first application of HOST+ASDOBI bifurcation computation, it was found that blade flapping and lead-lag dynamics did not play a significant role on the VRS boundaries (at least for the case of the Dauphin helicopter).

5.2 Heave Stability Criterion

In Chapters 3 and 4, inflow curves were calculated using the ring vortex model. It is noted from those inflow curves that there is not only an increase in the magnitude of induced velocity over the prediction from the momentum theory, but also a steeper gradient of inflow curve. At certain descent rates, the increase of induced velocity may be more rapid than the increase of descent rate.

According to Ref. [31], the derivative of the inflow curve from the momentum theory can be obtained as follows:

$$\frac{dv}{d\eta} = -\frac{1}{2} + \frac{\eta}{2\sqrt{\eta^2 + 4}} \tag{5.7}$$

In the range from $\eta = 0$ to $\eta = -1.5$, the absolute value of $\frac{d\nu}{d\eta}$ from the momentum theory is always less than 1. This indicates that with the momentum theory, a change in descent rate is associated with $|\Delta\nu| < |\Delta\eta|$, whereas with the ring vortex model, a change in descent rate results in $|\Delta\nu| > |\Delta\eta|$ (for values of η roughly in the range of -0.5 to -1.5).

The overall effect of a decrease in descent rate ($\Delta\eta > 0$) on blade angle of attack (α) and hence on heave damping ($\partial T / \partial \eta$) is:

$$\Delta\alpha \propto -\Delta\eta(1 + \frac{d\nu}{d\eta}) < 0 \quad \rightarrow \partial T / \partial \eta < 0 \tag{5.8}$$

with the momentum theory, and

$$\Delta\alpha \propto -\Delta\eta(1 + \frac{d\nu}{d\eta}) > 0 \quad \rightarrow \partial T / \partial \eta > 0 \tag{5.9}$$

with the ring vortex model. Thus, for values of η roughly in the range of -0.5 to -1.5, with the momentum theory, a decrease in descent rate results in a decrease in rotor thrust. This is the case when the vehicle vertical dynamics has positive (stable) heave damping, *i.e.*, $\partial T / \partial \eta < 0$. However, with the ring vortex model, an increase in descent rate from a value of η in the above-mentioned range gives rise to a decrease in rotor thrust, resulting in negative (unstable) heave damping, *i.e.*, $\partial T / \partial \eta > 0$.

5.3 Prediction of Dauphin VRS Boundary

The Dauphin model used in this study is an in-house rigid body flight dynamics model coded in MATLAB™. It includes three translational motions as well as roll and pitch motions. Blade flapping motion is assumed to be quasi-steady and there is no yaw degree-of-freedom. The aircraft gross weight is selected at 3500 kg. The Newton-Raphson algorithm is utilized for trim purpose.

The ring vortex model is used in the simulation for rotor inflow modeling in descent flight. Seven inflow states are chosen for both radial and azimuthal variations up to 1st harmonic. It is important to remember that the actual number of vortex rings is allowed to vary within a given range. In the earlier study, magnitudes of induced velocities were shown to scatter around their nominal values with a random choice of the number of rings. For the prediction of VRS boundary, a different number of vortex rings may result in a VRS boundary of different size. In this study, the nominal number of vortex rings are again chosen as two, while three vortex rings are considered as a worse case.

Following trim and linearization, eigenvalue of the heave dynamics mode is identified. The damping of its heave mode (real part of the eigenvalue, positive value for unstable heave mode) can be computed. The computations are conducted with two different numbers of vortex rings, as shown in Figure 5.3. From the damping results, the VRS boundary can be described based on stability characteristics of heave mode, as provided in Figure 5.4. In the figure, the VRS boundary consists of two contours. The small contour corresponds to $N_{ring} = 2$, while the large contour matches with $N_{ring} = 3$. For comparison, VRS boundary prediction using the parametric extension of momentum theory (Ref. [8]) is also provided in the figure.

When $N_{ring} = 2$, the corresponding contour appears to circle around inner points of test data. When $N_{ring} = 3$, the corresponding contour embraces all the test points. A stability strip is created between these two contours. Within the strip, even if the heave mode is stable at one moment, it may become unstable at another moment due to a random variation in the number of rings associated with the unsteady nature of flow in VRS.

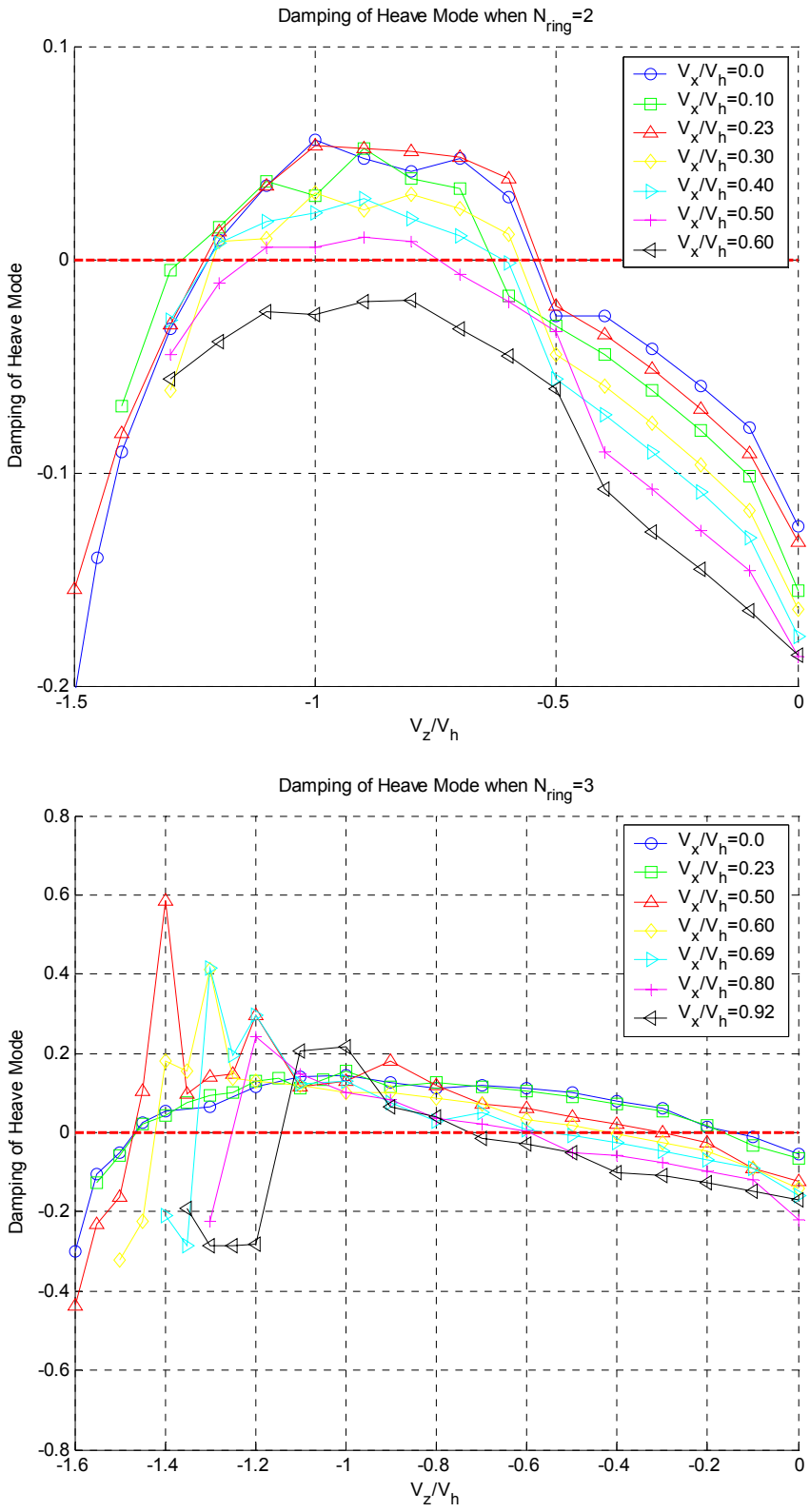

Figure 5.3: Damping of heave mode for two different numbers of vortex rings.

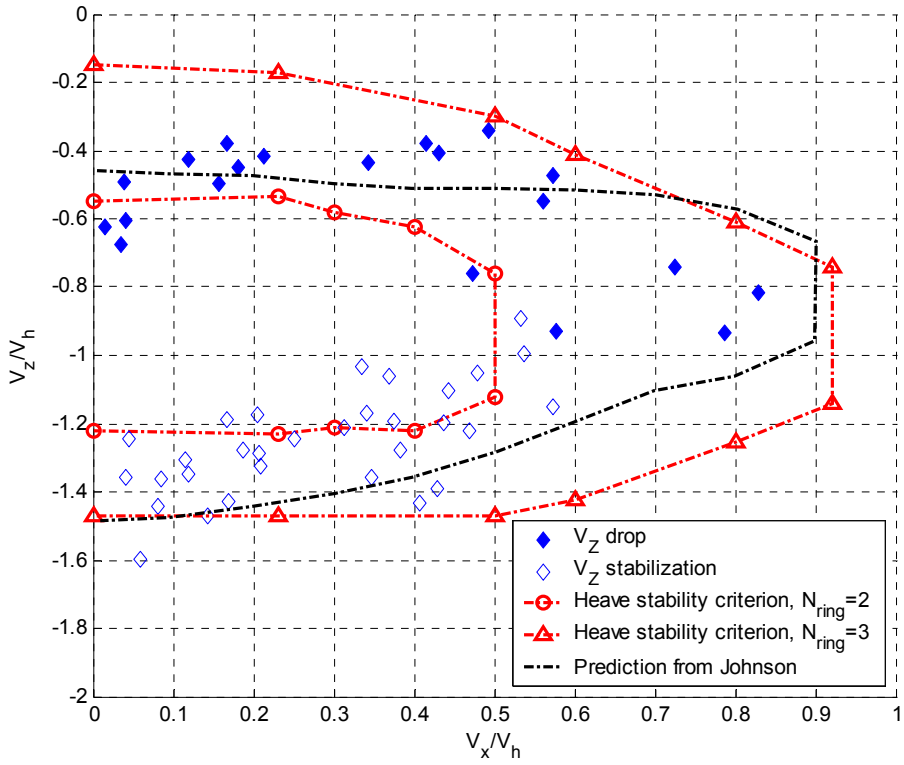

Figure 5.4: A comparison between Dauphin flight test results and VRS prediction based on heave stability criterion.

In a broader view, the contour with $N_{ring} = 3$ provides an advance warning to the helicopter at descent flight for potential VRS occurrence. The contour with $N_{ring} = 2$ gives the most conservative (most severe) condition. Consequently, it is possible to design a VRS detection and avoidance system based on information from the predicted VRS boundary.

The predicted VRS boundary from the parametric extension of momentum theory by Johnson is also computed based on heave stability criterion. It is noticed that Johnson's boundary locates in between the small and large contours computed using the ring vortex model. There is no stability strip in Johnson's boundary. From this aspect, the predicted VRS boundary using the ring vortex model is more practical.

The effect of the number of inflow states on the predicted VRS boundary is shown in Figure 5.5. Two sets of VRS boundaries are specified in the figure: one with three inflow

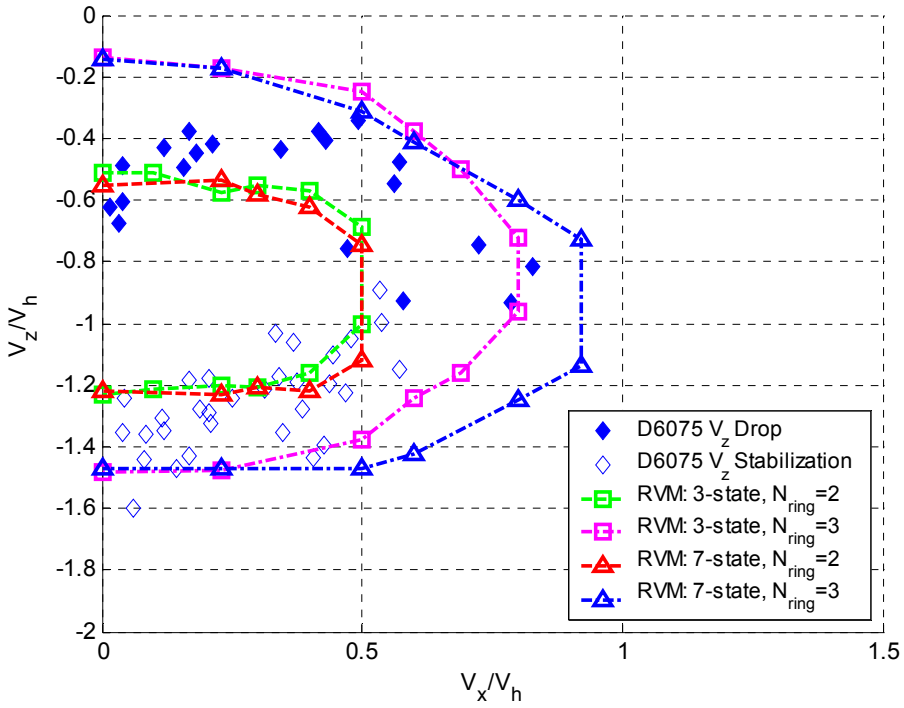

Figure 5.5: Effect of the finite-state inflow model in determining Dauphin VRS boundaries based on heave stability criterion.

states (radial variation), and the other with seven states (radial and azimuthal variations). The effect of the 7-state model tends to expand the VRS boundary at relatively high forward speed. When the forward speed is low, the boundaries are almost identical.

One amazing discovery is the correlation between heave stability criterion and bifurcation criterion. Three subplots are presented in Figure 5.6 for the Dauphin helicopter operating in axial descent. The top graph is the collective control trimmed result with respect to descent rate using the Newton-Raphson algorithm. Notice that the collective control initially decreases with the increase of descent rate. After approximately $\eta = -0.5$, the collective curve reverses its downward trend and keeps increasing until roughly $\eta = -1.2$. This is due to the nonlinear increase of induced velocity at the rotor disk. After $\eta = -1.2$, there is a rapid reduction in the collective control. The corresponding heave damping result is given in the middle graph. Note that the vertical dynamics is unstable in the range between $\eta = -0.5$ and $\eta = -1.2$.

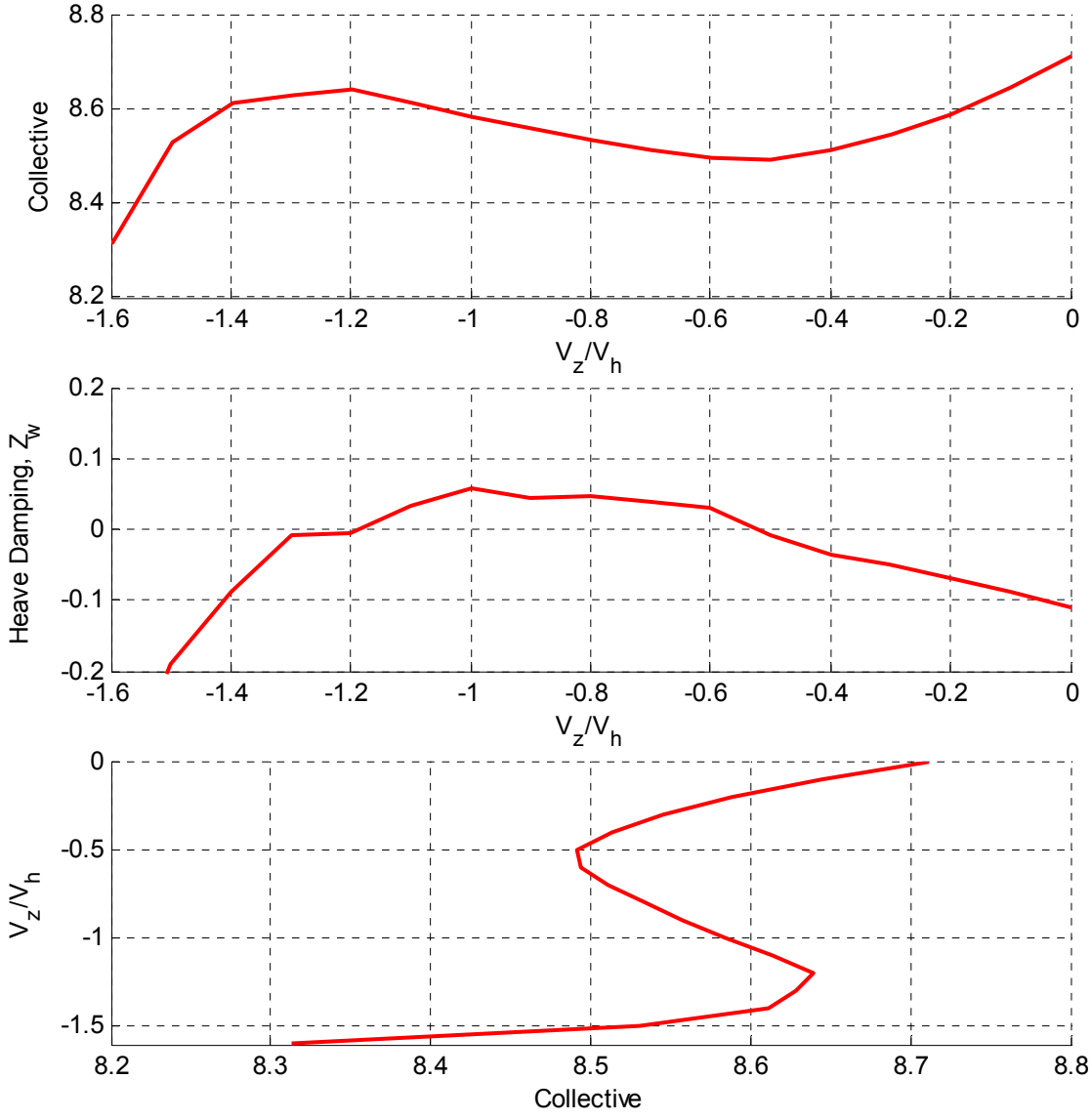

Figure 5.6: Correlation study between heave stability and bifurcation criteria.

It becomes interesting when both x and y axes are swapped in the top graph. The result is shown in the bottom subplot. Notice the similarity between this plot and the left plot in Figure 5.2. Multiple equilibria are clearly shown in the bottom subplot. The collective control is initially reduced as the descent rate increases. At nearly $\eta = -0.5$, a slight reduction in the collective control causes a fairly large increment in descent rate. On the other hand, if the helicopter is trimmed at a high descent rate, an increase of the collective control initially results in a reduction of descent rate. At approximately $\eta = -1.2$, a slight increase in the collective control gives rise to a rapid reduction of the descent rate. This is the exact phenomenon shown in the bifurcation study from ONERA (Refs. [31]-[32], [37]). Consequently, it can be concluded that heave stability and bifurcation are just two different aspects of the same phenomenon, *i.e.*, uncommanded drop in descent rate as observed from the Dauphin flight test. If the descent rate is fixed, unstable heave dynamics can be observed from the trim calculation and linearization study. If the collective control is perturbed at certain descent rate, a rapid increase of the descent rate can be experienced from time history dynamic analysis. Both result in a sudden increase of descent rate.

5.4 Dynamic Response in Descent flight

Time simulations are conducted with the in-house Dauphin flight dynamic model. The aircraft gross weight is again set at 3500 kg. Two flight cases are simulated. In the first case, the helicopter performs axial descent from hover with designated collective reduction profile. The purpose is to reproduce uncommanded drop of descent rate observed in the flight test. The second case involves vertical response of the vehicle following an increase of collective pitch initialized at different times. The objective is to identify effectiveness of collective control in descent flight.

Results for the case of a selected collective control profile are shown in Figure 5.7 In the top plot, the main rotor collective pitch is reduced from its trimmed value. The

reduction is gentle with total collective change of -0.45^o in 80 seconds. In the bottom plot, vertical responses are provided with inflow modeling based on both the momentum theory and the ring vortex model. There is a clear contrast between these two vertical responses. With the momentum theory, the vertical motion of the helicopter responds in a similar gentle fashion. At the end of the simulation, the descent rate stabilizes at $\eta = -0.3$. With the ring vortex model, two gentle increases in the descent rate can be first observed. Between 40 to 70 seconds, a sudden increase of descent rate appears following the third moderate reduction of collective control. This indicates the occurrence of unstable heave mode, as predicted in the previous section. The rate of descent eventually stabilizes at $\eta = -1.6$.

Figure 5.8 shows the calculated results for different collective control inputs. The helicopter is initially trimmed at $\eta = -0.6$. The designed collective control profiles are given in the top plot. All three collective controls are increased by 0.8^o during the subsequent dynamic simulation. The difference among three cases is the time at which the collective control is invoked. In the first instance, the control starts at $t = 0.2$ second. As shown in the bottom plot, the corresponding descent rate bounces back. This indicates that the pilot is still able to recover the descent motion by pulling up the collective control. When the time for control invocation increases to 1.2 second, the descent rate tends to remain around $\eta = -0.6$. In the third instance, change of the collective control only starts after $t = 3.2$ second when the descent rate has already increased beyond $\eta = -1.0$. Notice that the descent rate continues to increase despite the collective control increment. In this case, the collective control is no longer effective.

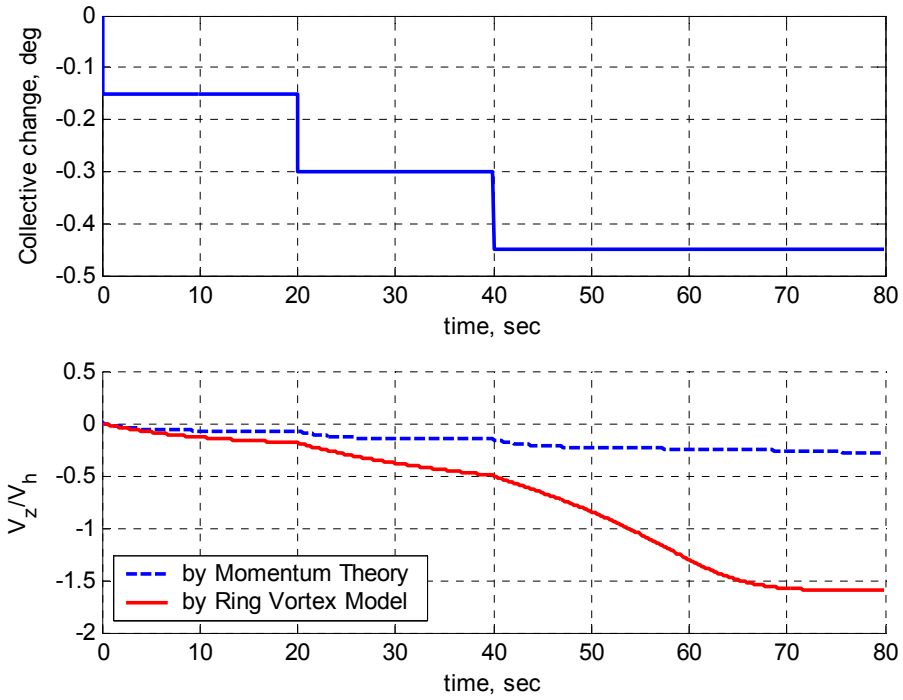

Figure 5.7: Dynamic response of descent rate following moderate reduction in collective control.

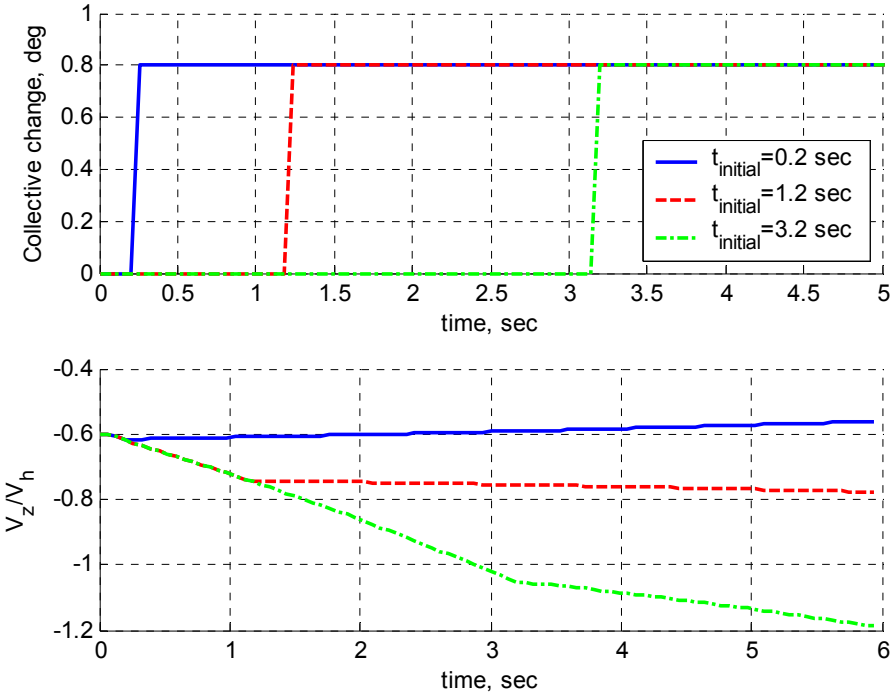

Figure 5.8: Dynamic Response of descent rate following increase of collective control initialized at different times.

CHAPTER 6 APPLICATION TO A SIDE-BY-SIDE ROTOR CONFIGURATION

6.1 Introduction

Compared to the number of studies for a single rotor in VRS, experiments and research for a side-by-side rotor configuration (including tilt-rotor) have been relatively sparse. Washizu et al conducted the tests on a tandem rotor system for both axial and non-axial conditions but found only insignificant differences between the single rotor and tandem rotors (Ref. [46]). Betzina used a rotor and an image plane to emulate tilt-rotor in a wind-tunnel test and discovered that the image plane had large effect on the rotor in terms of induced velocity and thrust fluctuations (Ref. [16]). However, as pointed out in Ref. [8], the image plane may not be a true representation of a tilt-rotor configuration, in which two unsteady rotor wakes are interacting with each other.

In Refs. [23]-[24], specific concerns were raised regarding the potential impact of the VRS on a tilt-rotor aircraft. It was argued that VRS could be initiated on one or both rotors simply by the effect of yaw rate or roll rate, even when a tilt-rotor aircraft was operating outside the steady state VRS boundary. In roll maneuver, one rotor would descend faster, which could place this rotor near VRS boundary. The concern on yaw rate was similar. It was also suggested that significant loads, large thrust fluctuations, and potential loss of control could occur during these maneuvers.

The investigations conducted by the V-22 flight test team included a formulation of the steady state VRS boundary, an establishment of safe operation procedures for VRS avoidance, and a sensitivity study of critical rotor parameters (Refs. [17]-[18]). To respond specifically to the concerns from Refs. [23]-[24], corresponding dynamic maneuvers were added to the test matrix. Following the tests, Ref. [18] confirmed that

rapid rolling and yawing, high pitch decelerations, and a combination of multi-axis maneuvers could not induce VRS inside the steady state VRS boundary. Rotor control inputs and maneuvers actually suppressed VRS symptoms. From another perspective, the steady state VRS boundary in fact defined the most conservative boundary for VRS avoidance.

In this chapter, a preliminary study is conducted on a side-by-side rotor configuration. This study is a further application of the ring vortex model. Each of the two rotors has its own set of vortex rings, which affects inflow of not only the original rotor but also that of the second rotor. Therefore, the aerodynamic environment and the behaviors of the two rotors are affected by the characteristics of the two sets of vortex rings, including the number of rings, the vortex strength, and the locations of the rings. While detailed parameters for the V-22 tilt-rotor aircraft are not available in the open literature, a simplified side-by-side rotor model is set-up in the MATLAB™ environment. Each rotor has a diameter of 40 feet with a moderate blade twist of -10^{o}. Total thrust generated from the two rotors is 15500 lb. The separation distance between the two rotors is 2.1 times the rotor radius. The focus of the numerical investigation is to demonstrate the impact of vortex rings on latent thrust deficit and on lateral AFCS limit.

6.2 Latent Thrust Deficit

Latent thrust deficit, a term used in Refs. [17]-[18], refers to one of the two rotors operating at a higher collective pitch to equalize its thrust relative to that of the opposite rotor. In the ring vortex model, the phenomenon can be captured by selecting different numbers of vortex rings on each rotor. Collective pitch asymmetry is thus developed in order to achieve wing-level trim condition. Note that the asymmetry is caused not only by the difference in the numbers of rings, but also by the natural interaction from one set of vortex rings on the other.

As an illustration, the two rotors are assumed to have different number of vortex rings, *i.e.*, $N_{ring} = 1$ and $N_{ring} = 3$. Differences in the trimmed collective pitch between two rotors, known as differential collective control, are calculated as a function of both descent rate (from 0 to $\eta = -2.5$) and forward velocity (from 0 to $V_x V_h = 1.5$). Results are shown in Figure 6.1. Observations from the figure can be summarized as follows:

- Effect from uneven distribution of vortex rings dominates the differential collective control. Aerodynamic interaction from the two sets of vortex rings tends to increase the differential collective control but its influence appears to be insignificant.
- As forward velocity increases, the differential collective control generally decrease since vortex rings are swept away at a greater distance.
- The maximum value for the differential collective control occurs when the side-by-side rotor model is in axial descent.

A missing component in the numerical simulation is wake interference from the finite-state inflow model. He (Ref. [47]) proposed a finite-state rotor wake interference model, capable of predicting both non-uniform and unsteady rotor wake flow field. Although the effect from the rotor wake interference is expected to be less dominant than the effect from uneven distribution of vortex rings, an inclusion of such interference may be needed for a comprehensive full-vehicle study in the future.

6.3 Dynamic Response

In Section 6.2, when lateral thrust asymmetry is encountered, collective controls of the two rotors need to be adjusted in order to achieve wing-level flight. In the case of V-22 tilt-rotor aircraft, the adjustment is automatically performed by a lateral AFCS (Automatic Flight Control System), provided that the control authority of the lateral AFCS is sufficient. Once the lateral AFCS runs out of authority, a roll response develops.

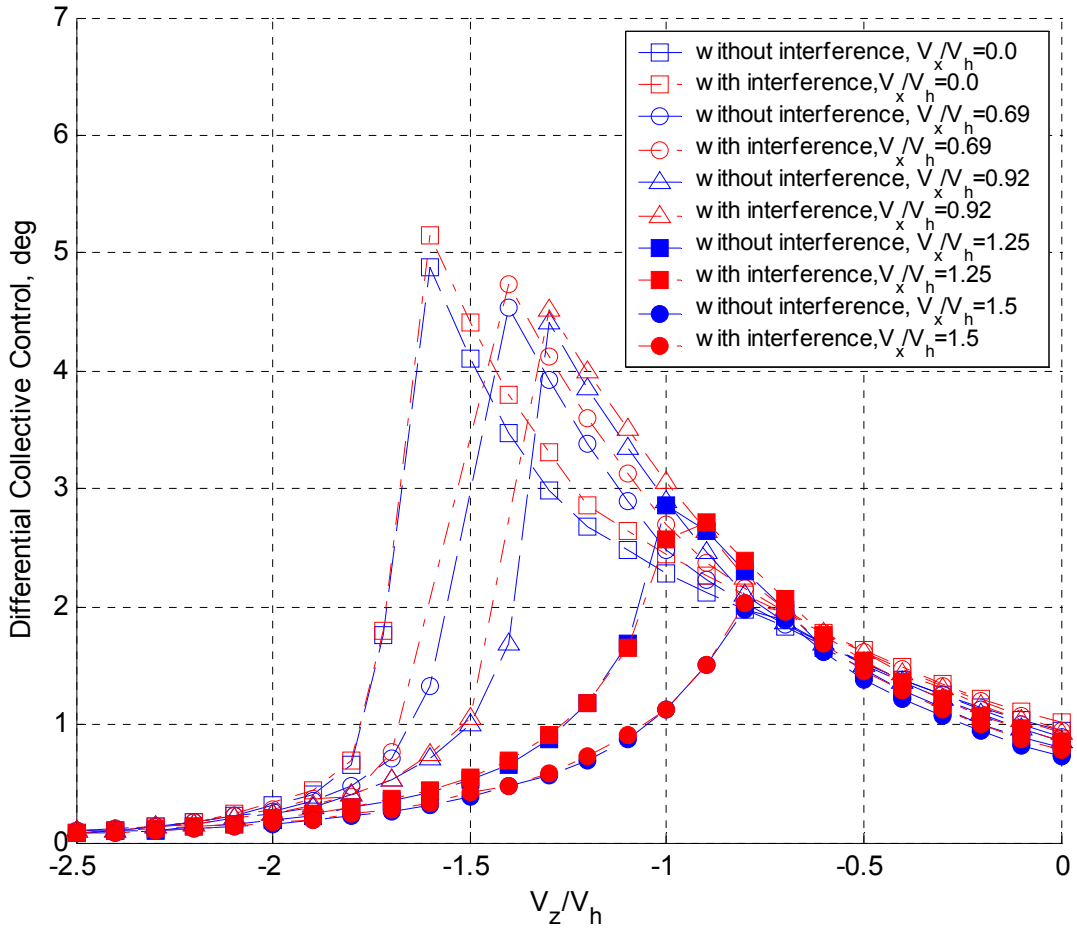

Figure 6.1: Differential collective control due to asymmetry in the numbers of rings and interference from the vortex rings

If pilot intervention is not followed in a timely fashion, a potential hazardous situation may occur.

To numerically reproduce the situation, a simple AFCS is incorporated in the lateral channel, with both roll rate and roll attitude feeding back to the lateral control (differential collective). An artificial limit of lateral AFCS is set at 1^{o}[2]. Time simulation is conducted with the in-house side-by-side rotor model in order to compare the dynamic response with and without the lateral AFCS limit. Results are provided in Figure 6.2. The side-by-side rotor model starts at moderate descent rate with $\eta = -0.6$. The number of vortex rings on both of the two rotors is first set at two. As time increases to 0.2 second, the number of vortex rings on one rotor decreases to one and increases to three on the other rotor. The induced inflow on the rotor with one vortex ring decreases, while the inflow on the rotor with three vortex rings increases. In order to maintain wing-level flight, the collective control on the rotor with one vortex ring needs to be reduced, while the collective on the rotor with three vortex rings has to increase. The resultant differential collective control profiles generated from the lateral AFCS are shown in the top chart. The effect of 1^{o} limit is clearly presented. The responses of normalized vertical speed are given in the middle plot. Without the AFCS limit, the side-by-side rotor model recovers from the descent. When the AFCS limit is imposed, the side-by-side rotor model continues its descent motion. The corresponding roll attitude increases rapidly within a second, as evident in the bottom plot of the figure. This indicates that the lateral control has become ineffective.

[2] Johnson set a 2^{o} limit on differential collective in his study of asymmetric rotor aerodynamics but he used a different autopilot (Ref. [8]).

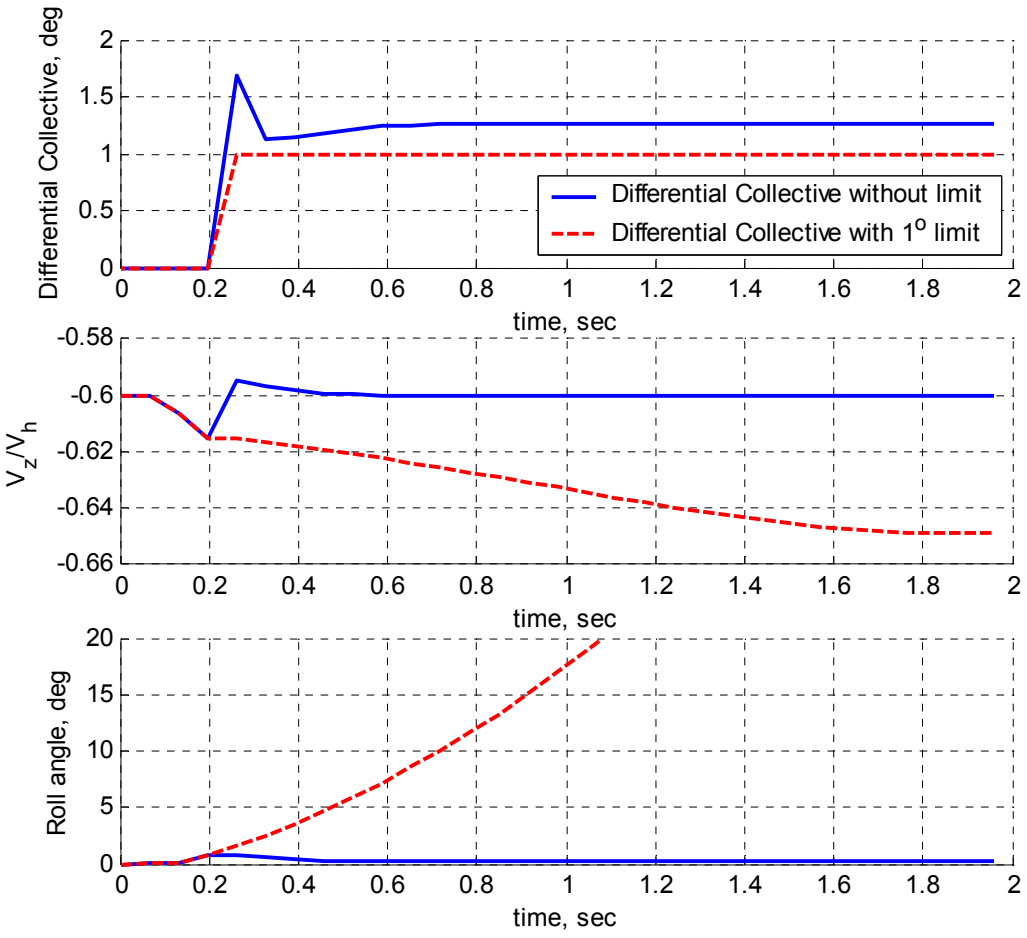

Figure 6.2: Dynamic response of a side-by-side rotor model with and without limit on differential collective control.

CHAPTER 7 CONCLUSIONS AND RECOMMENDATIONS

7.1 Conclusions

In this dissertation, a ring vortex model has been developed for rotor inflow modeling in descent flight. Validations of the new inflow model have revealed good correlations with experiments in both axial and inclined descent. The ring vortex model can be utilized in the rotorcraft flight dynamic study and simulation in descent flight. Further, it can be used in the sensitivity studies associated with various rotor parameters and different rotor configurations.

Highlights of the ring vortex model are given as follows:

1. One major objective of the ring vortex model is to address the strong interaction between the rotor wake and the surrounding airflow in descent flight. Vortex rings are thus created due to this flow interaction. Each vortex ring induces normal velocity at the rotor disk. In addition, the total mass flow parameter in the existing flow models (including the momentum theory) is adjusted to create a steady state transition between the helicopter and the windmill branches. The combined effect of the additional normal velocity from the vortex rings and the baseline induced velocity from the augmented inflow models provides an improvement in predicting the inflow at the rotor disk in descent flight. With the ring vortex model, the rotor induced inflow can be adequately computed over the entire range of descent flight.
2. The new inflow model utilizes the concept of vortex rings to create a nonlinear effect on rotor induced velocity. The closer a vortex ring is located to the rotor

disk, the larger the magnitude of normal velocity that acts on the disk. This non-uniform effect conforms to the observations from experiments.

3. As a rotor begins to descend, the vortex rings gradually move upwards. As the descent rate increases, those rings tend to accumulate near the rotor disk, resulting in a significant increment in the mean induced velocity. As the rate of descent increases further, the vortex rings pass through the rotor disk and move upwards quickly above the rotor disk, entering into autorotation stage.
4. In order to investigate the effects from blade taper, blade twist, and forward velocity, the modified momentum theory is further replaced by an augmented finite-state inflow model (see Appendix A). Seven inflow states are chosen to include both radial and azimuthal variations up to 1st harmonic.
5. The number of vortex rings can vary within a selected range. By doing so, it is conceived that vortex rings may survive beyond its nominal value with slightly benign aerodynamic environment at a particular moment or prematurely burst with slightly adversary environment at another moment. Such a random representation of the number of vortex rings can create the randomness in the induced velocity results seen in experiments.

Specific findings from the studies are summarized as follows:

1. Validations of induced velocity prediction have shown satisfactory agreement with four different experimental sets from the open literature. In particular, the lower boundary of predicted induced velocity variations tends to conform to the momentum theory, while the upper boundary appears to double the average values. This result matches with the observation made by Heyson (Ref. [20]).
2. Once a rotor starts to descend, its collective control and corresponding torque requirement (and hence power consumption) remain almost the same as or even higher than at hover. The increased power requirement in the descent is also

known as power settling. As the rotor enters into the transition phase, both collective control and power diminish rapidly.

3. In the study of changes in rotor thrust due to variation in the number of vortex rings, a reduction in average thrust is shown. As the rotor descends from hover, an increase in the rate of descent is accompanied by an increase in the changes in thrust. With a further increase in the descent rate (beyond transition phase), changes in thrust diminish and finally disappear.
4. Compared with changes in rotor thrust, rotor torque variations are less significant in descent flight.
5. There are no substantial differences in the inflow curves due to variations in rotor rotational speed and rotor radius.
6. The effects of blade twist include a higher rate of descent for ideal autorotation and a higher normalized peak induced velocity (ν_{peak}) at increased normalized rate of descent (η_{peak}). Within the range of the study (θ_{tw} from 0^o to -22.5^o), the effects tend to grow stronger with the increased blade twist.
7. The effect of blade taper on VRS is moderate and weaker than the effect of blade twist.
8. The influence from rotor thrust appears to be minor. The effect is a result of two competing factors involving vortex strength and translation of vortex rings away from the rotor disk.
9. A number of criteria for arriving at VRS boundaries have been proposed over the years. It is seen that VRS boundaries are significantly influenced by the specific criterion used.
10. The Dauphin VRS boundary is predicted based on heave stability criterion. Two contours are given corresponding to different number of vortex rings. The large contour provides an advance warning to the helicopter for potential VRS

occurrence, while the small one gives the most severe condition. Consequently, it is possible to design a VRS detection and avoidance system based on information from the predicted VRS boundary.

11. Heave stability and bifurcation are two different aspects of the same phenomenon, *i.e.*, uncommanded drop in descent rate. If the descent rate is fixed, unstable heave dynamics can be observed from the trim calculation and linearization study. If the collective control is perturbed at certain descent rate, a rapid increase of the descent rate can be experienced from time history dynamic analysis. Both result in a sudden increase of descent rate.
12. By uneven distribution of vortex rings on each rotor, collective control asymmetry in a side-by-side rotor configuration can be captured. Aerodynamic interaction from two sets of vortex rings appears to be insignificant.
13. Roll-off response is reproduced in the dynamic simulation associated with the typical limited authority of a lateral AFCS.

7.2 Recommendations for Future Work

Recommendations for future work are listed as follows:

1. In the present study, vortex rings are assumed to move along a hypothetical straight line determined by the vector sum of the forward velocity component of free stream air and the convection speed of the rings. In the helicopter maneuvering flight, the wake behind the rotor disk is curved (Ref. [48]). Better prediction may be achieved in the dynamic simulation if the vortex rings move along a curved trajectory determined by the critical parameters in a maneuvering flight, e.g., pitch rate in a pull-up maneuver.
2. In the study, the interaction between vortex rings is ignored. However, complex motion of the vortex rings, known as vortex pairing, was observed in the

experiment (Ref. [49]). Inclusion of vortex pairing will shed new light on the unsteady aspect of rotor thrust and torque fluctuations.

3. Efforts have been taken to acquire data for a comprehensive study of the V-22 tilt-rotor aircraft. Nevertheless, detailed parameters for the V-22 aircraft are not available in the open literature. In the future, once a V-22 flight dynamic model is built-up in conjunction with the ring vortex model, more engineering analyses can be performed.
4. One of the motivations for this study is to develop an efficient and easy-to-implement rotor inflow model. The ring vortex model fulfills these requirements and is thus suitable for high fidelity flight simulations and for handling qualities assessment.
5. In addition to further validation of the ring vortex model using additional wind-tunnel and flight test data, the most natural step is to carry out pilot-in-the-loop simulation evaluations.

APPENDIX A: AUGMENTED FINITE-STATE INFLOW MODELS FOR TRANSITION

In the ring vortex model, the finite-state inflow models of different inflow states (Refs. [39], [41]) are augmented to create a transition phase for the inflow curves in descent flight. The augmented inflow models are summarized as follows:

Augmented One-State Inflow Model

$$M\dot{\alpha}_1^0 + L^{-1}V_T\alpha_1^0 = \tau_1^{0c} \tag{A.1}$$

where

$$M = 0.6366 \tag{A.2}$$

$$L^{-1} = 1.3333 \tag{A.3}$$

$$V_T = \sqrt{\left(\frac{\mu_z}{2.72(1+\bar{\mu}^2)}\right)^2 + \mu^2 + \lambda^2} \tag{A.4}$$

$$\lambda = -\mu_z + \lambda_m \tag{A.5}$$

$$\lambda_m = \sqrt{3}\alpha_1^0/(\Omega R) \tag{A.6}$$

and $\alpha_1^0, \tau_1^{0c}, \mu, \mu_z, \bar{\mu}$ are the inflow state, the pressure coefficient, in-plane and vertical velocity components in the tip path plane (positive upwards), and normalized advance ratio, respectively. V_T is also known as total flow parameter.

Augmented Three-State Inflow Model

$$M\dot{x} + L^{-1}\widetilde{V}x = \tau \tag{A.7}$$

where

$$M = \begin{bmatrix} 0.6366 & 0 & 0 \\ 0 & 0.2829 & 0 \\ 0 & 0 & 0.1811 \end{bmatrix} \tag{A.8}$$

$$L^{-1} = \begin{bmatrix} 1.4694 & -0.4988 & 0.2274 \\ -0.4988 & 1.8624 & -0.6174 \\ 0.2274 & -0.6174 & 1.7591 \end{bmatrix} \tag{A.9}$$

$$\widetilde{V} = \begin{bmatrix} V_T & & \\ & V & \\ & & V \end{bmatrix} \tag{A.10}$$

$$V = \frac{\left(\frac{\mu_z}{2.72(1+\overline{\mu}^2)}\right)^2 + \mu^2 + (\overline{\lambda} + \overline{\lambda}_m)\overline{\lambda}}{\sqrt{\left(\frac{\mu_z}{2.72(1+\overline{\mu}^2)}\right)^2 + \mu^2 + \overline{\lambda}^2}} \tag{A.11}$$

$$\overline{\lambda} = -\mu_z + \overline{\lambda}_m \tag{A.12}$$

$$\overline{\lambda}_m = \frac{1}{2}\frac{\overline{C}_T}{\sqrt{\mu^2 + \overline{\lambda}^2}} \tag{A.13}$$

$x = [\alpha_1^0, \alpha_3^0, \alpha_5^0]^T$ is the inflow state vector for radial variation with 0^{th} harmonic. $\tau = [\tau_1^{0c}, \tau_3^{0c}, \tau_5^{0c}]^T$ is the cosine pressure coefficient vector. The formula for V_T can be referred from one-state inflow model. In addition, V is known as flow parameter and $\overline{C}_T$ is steady thrust coefficient.

Augmented Seven-State Inflow Model

$$M\dot{x} + L^{-1}\widetilde{V}x = \tau \tag{A.14}$$

where

$$M = \begin{bmatrix} 0.6366 & 0 & 0 & 0 & 0 & 0 & 0 \\ 0 & 0.2829 & 0 & 0 & 0 & 0 & 0 \\ 0 & 0 & 0.1811 & 0 & 0 & 0 & 0 \\ 0 & 0 & 0 & 0.4244 & 0 & 0 & 0 \\ 0 & 0 & 0 & 0 & 0.2264 & 0 & 0 \\ 0 & 0 & 0 & 0 & 0 & 0.4244 & 0 \\ 0 & 0 & 0 & 0 & 0 & 0 & 0.2264 \end{bmatrix} \tag{A.15}$$

$$\widetilde{V} = \begin{bmatrix} V_T & 0 & 0 & 0 & 0 & 0 & 0 \\ 0 & V & 0 & 0 & 0 & 0 & 0 \\ 0 & 0 & V & 0 & 0 & 0 & 0 \\ 0 & 0 & 0 & V & 0 & 0 & 0 \\ 0 & 0 & 0 & 0 & V & 0 & 0 \\ 0 & 0 & 0 & 0 & 0 & V & 0 \\ 0 & 0 & 0 & 0 & 0 & 0 & V \end{bmatrix} \tag{A.16}$$

$$L = \begin{bmatrix} \left(L_{11}^{00}\right)^c & \left(L_{13}^{00}\right)^c & \left(L_{15}^{00}\right)^c & \left(L_{12}^{01}\right)^c & 0 & 0 & 0 \\ \left(L_{31}^{00}\right)^c & \left(L_{33}^{00}\right)^c & \left(L_{35}^{00}\right)^c & \left(L_{32}^{01}\right)^c & \left(L_{34}^{01}\right)^c & 0 & 0 \\ \left(L_{51}^{00}\right)^c & \left(L_{53}^{00}\right)^c & \left(L_{55}^{00}\right)^c & 0 & \left(L_{54}^{01}\right)^c & 0 & 0 \\ \left(L_{21}^{10}\right)^c & \left(L_{23}^{10}\right)^c & 0 & \left(L_{22}^{11}\right)^c & \left(L_{24}^{11}\right)^c & 0 & 0 \\ 0 & \left(L_{43}^{10}\right)^c & \left(L_{45}^{10}\right)^c & \left(L_{42}^{11}\right)^c & \left(L_{44}^{11}\right)^c & 0 & 0 \\ 0 & 0 & 0 & 0 & 0 & \left(L_{22}^{11}\right)^s & \left(L_{24}^{11}\right)^s \\ 0 & 0 & 0 & 0 & 0 & \left(L_{42}^{11}\right)^s & \left(L_{44}^{11}\right)^s \end{bmatrix} \tag{A.17}$$

$$\left(L_{11}^{00}\right)^c = 0.75, \left(L_{13}^{00}\right)^c = \left(L_{31}^{00}\right)^c = 0.1909, \left(L_{15}^{00}\right)^c = \left(L_{51}^{00}\right)^c = -0.0299 \tag{A.18}$$

$$\left(L_{33}^{00}\right)^c = 0.6563, \left(L_{35}^{00}\right)^c = \left(L_{53}^{00}\right)^c = 0.20579, \left(L_{55}^{00}\right)^c = 0.6445 \tag{A.19}$$

$$\left(L_{22}^{11}\right)^c = (1 - X^2)\Gamma_{22}^{11} \tag{A.20}$$

$$\left(L_{24}^{11}\right)^c = \left(L_{42}^{11}\right)^c = (1 - X^2)\Gamma_{24}^{11} \tag{A.21}$$

$$\left(L_{44}^{11}\right)^c = (1 - X^2)\Gamma_{44}^{11} \tag{A.22}$$

$$\Gamma_{22}^{11} = 0.6250, \Gamma_{24}^{11} = 0.1914, \Gamma_{44}^{11} = 0.6328 \tag{A.23}$$

$$\left(L_{22}^{11}\right)^s = (1 + X^2)\Gamma_{22}^{11} \tag{A.24}$$

$$\left(L_{24}^{11}\right)^s = \left(L_{42}^{11}\right)^s = (1 + X^2)\Gamma_{24}^{11} \tag{A.25}$$

$$\left(L_{44}^{11}\right)^s = (1 + X^2)\Gamma_{44}^{11} \tag{A.26}$$

$$\left(L_{12}^{01}\right)^c = 2X\Gamma_{12}^{01} \tag{A.27}$$

$$\left(L_{32}^{01}\right)^c = 2X\Gamma_{32}^{01} \tag{A.28}$$

$$\left(L_{34}^{01}\right)^c = 2X\Gamma_{34}^{01} \tag{A.29}$$

$$\left(L_{54}^{01}\right)^c = 2X\Gamma_{54}^{01} \tag{A.30}$$

$$\Gamma_{12}^{01} = -0.2485, \Gamma_{32}^{01} = -0.2437, \Gamma_{34}^{01} = -0.2489, \Gamma_{54}^{01} = -0.2480 \tag{A.31}$$

$$\left(L_{21}^{10}\right)^c = 2X\Gamma_{21}^{10} \tag{A.32}$$

$$\left(L_{23}^{10}\right)^c = 2X\Gamma_{23}^{10} \tag{A.33}$$

$$\left(L_{43}^{10}\right)^c = 2X\Gamma_{43}^{10} \tag{A.34}$$

$$\left(L_{45}^{10}\right)^c = 2X\Gamma_{45}^{10} \tag{A.35}$$

$$\Gamma_{21}^{10} = 0.4965, \Gamma_{23}^{10} = 0.4878, \Gamma_{43}^{10} = 0.4978, \Gamma_{45}^{10} = 0.4965 \tag{A.36}$$

$$X = \frac{\mu}{V_T + |\lambda|} \tag{A.37}$$

$x = [\alpha_1^0, \alpha_3^0, \alpha_5^0, \alpha_2^1, \alpha_4^1, \beta_2^1, \beta_4^1]^T$ is the inflow state vector for radial and azimuthal variations up to 1st harmonic. $\tau = [\tau_1^{0c}, \tau_3^{0c}, \tau_5^{0c}, \tau_2^{1c}, \tau_4^{1c}, \tau_2^{1s}, \tau_4^{1s}]^T$ is the pressure coefficient vector with both cosine and sine terms.

APPENDIX B: COMPUTATIONAL PROCEDURE WITH THE RING VORTEX MODEL

In this appendix, a step-by-step computational procedure with the ring vortex model is provided in the following:

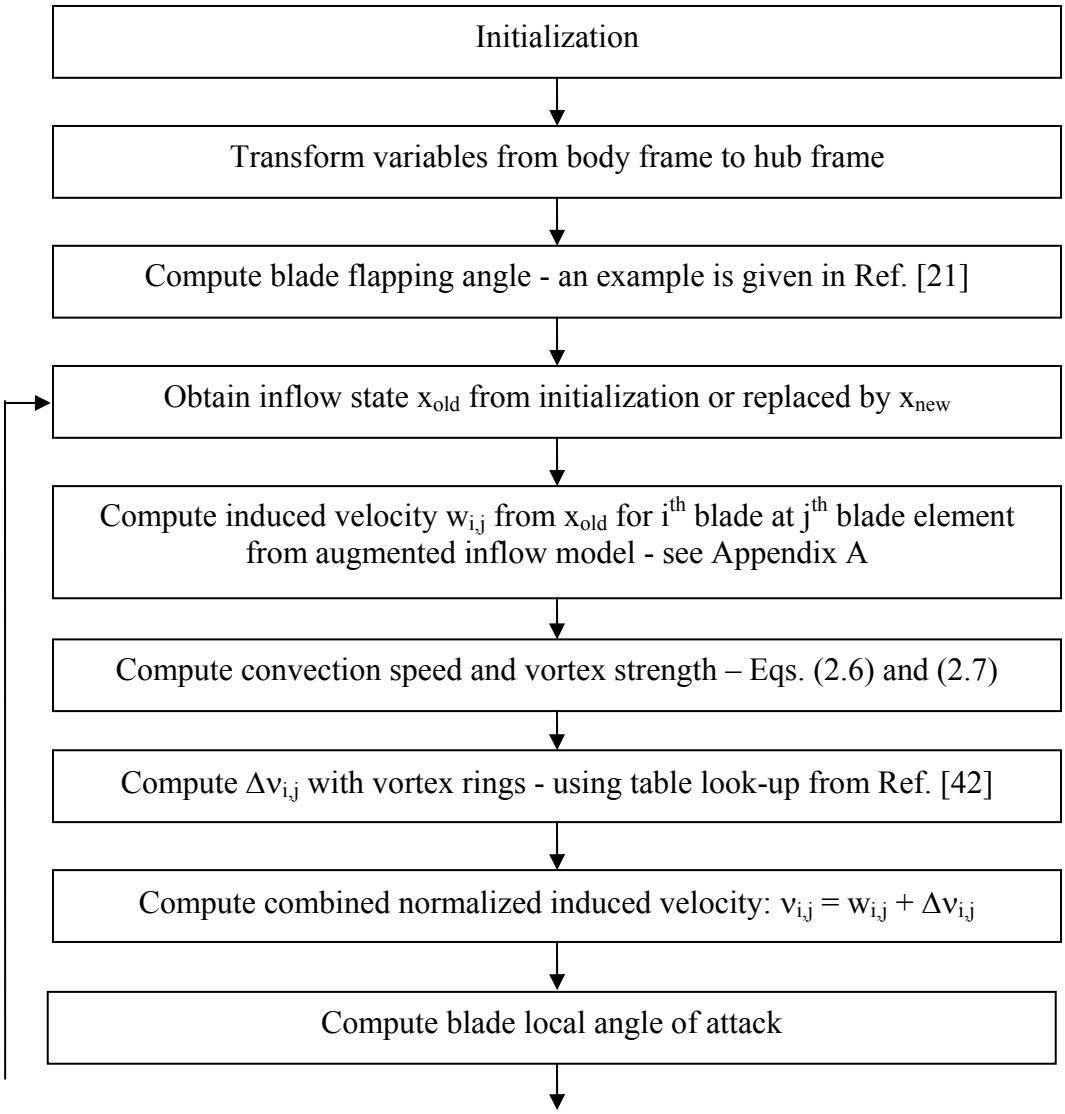

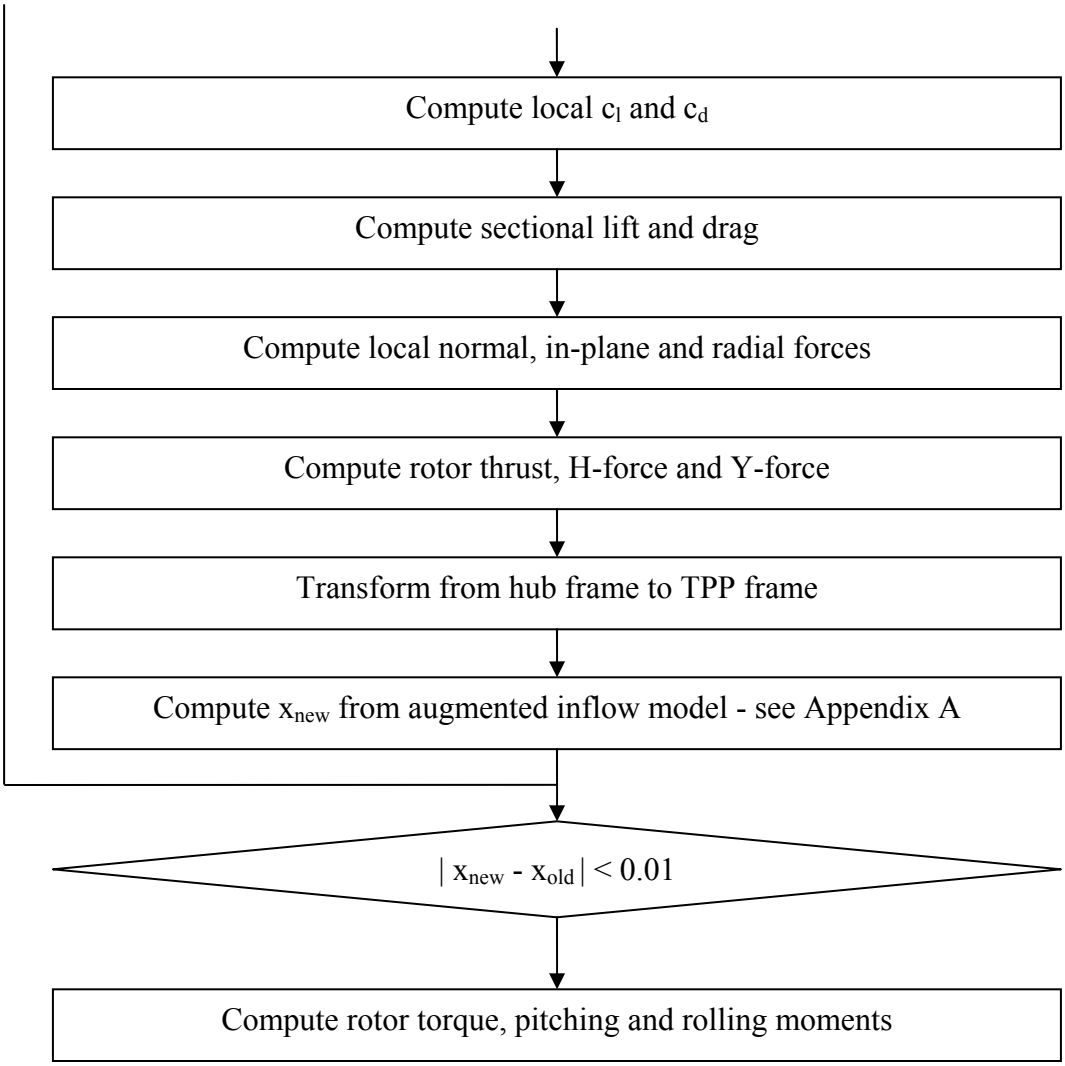
Compute local c_l and c_d
Compute sectional lift and drag
Compute local normal, in-plane and radial forces
Compute rotor thrust, H-force and Y-force
Transform from hub frame to TPP frame
Compute x_{new} from augmented inflow model - see Appendix A
$| x_{new} - x_{old} | < 0.01$
Compute rotor torque, pitching and rolling moments

REFERENCES

[1] Drees, J.M., and Hendal, W.P., "The Field of Flow Through a Helicopter Rotor Obtained from Wind-tunnel Smoke Tests", Journal of Aircraft Engineering, Vol 23(266), 1950.

[2] Prouty, R.W., "Helicopter Performance, Stability, and Control", Robert K. Krieger Publishing Company, Malabar, Florida, 1986.

[3] Varnes, D.J., Duren R.W., and Wood E.R., "An Onboard Warning System to Prevent Hazardous Vortex Ring State Encounters", 26th European Rotorcraft Forum, 2000.

[4] Daiey, J.R., "Report of the Panel to Review the V-22 Program," Memorandum for the Secretary of Defense, 30 April 2001.

[5] -, "U.S. Preliminary Accident Report Summaries, April – June 2000", Helicopter Association International, August 2000.

[6] -. "AAIU Report NO.: 2002/005", Air Accident Investigation Unit, Department of Transport, Ireland.

[7] Castles, W. Jr., and Gray, R.B., "Empirical Relation Between Induced Velocity, Thrust, and Rate of Descent of a Helicopter Rotor as Determined by Wind-Tunnel Tests on Four Model Rotors", NACA TN 2474, October 1951.

[8] Johnson, W., "Model for Vortex Ring State Influence on Rotorcraft Flight Dynamics", AHS 4th Decennial Specialist's Conference on Aeromechanics, San Francisco, California, January 21-23, 2004.

[9] Taghizad, A., Jimenez, J., Binet, L, and Heuzé, D., "Experimental and Theoretical Investigation to Develop a Model of Rotor Aerodynamics Adapted to Steep Descent", American Helicopter Society 58th Annual Forum, Montréal, Canada, June 11-13, 2002.

[10] He, C.J., Lee, C.S., and Chen, W.B., "Finite State Induced Flow Model in Vortex Ring State", Journal of the American Helicopter Society, Vol. 45, No. 4, October 2000.

[11] Yaggy, P.F., and Mort, K.W., "Wind-Tunnel Tests of Two VTOL Propellers in Descent", NACA TN D-1766, 1962.

[12] Washizu, K., Azuma, A., Koo, J., and Oka, T., "Experiemnts on a Model Helicopter Rotor Operating in the Vortex Ring State", Journal of Aircraft, Vol. 3 (3), May-June 1966.

[13] Empey, R.W., and Ormiston, R.A., "Tail-Rotor Thrust on a 5.5-foot Helicopter Model in Ground Effect", American Helicopter Society Annual National Forum, Washington, D.C., May 1974.

[14] Xin, H., and Gao, Z., "An Experimental Investigation of Model Rotors Operating in Vertical Descent", European Rotorcraft Forum, Cernobbio, Italy, September, 1993.

[15] Xin, H., and Gao, Z., "A Prediction of the Vortex-Ring State Boundary Based on Model Tests", Transactions of Nanjing University of Aeronautics and Astronautics, Vol. 11 (2), December 1994.

[16] Betzina, M.D., "Tiltrotor Descent Aerodynamics: A Small-Scale Experimental Investigation", American Helicopter Society Annual Forum, Washington D.C., May 2001.

[17] Brand, A., Kisor, R., Blyth, R., Mason, D., and Host, C., "V-22 High Rate of Descent (HOD) Test Procedures and Long Record Analysis", American Helicopter Society 60th Annual Forum, Baltimore, MD, June 7-10, 2004.

[18] Kisor, R., Blyth, R., Brand, A., and MacDonald, T., "V-22 Low-Speed/High Rate of Descent (HROD) Test Results", American Helicopter Society 60th Annual Forum, Baltimore, MD, June 7-10, 2004.

[19] Wolkovitch, J. "Analytic Prediction of Vortex-Ring Boundaries for Helicopters in Steep Descents", Journal of the American Helicopter Society, Vol. 17, No. 3, July 1971.

[20] Heyson, H.H., "A Momentum Analysis of Helicopters and Autogyros in Inclined Descent, with Comments on Operational Restrictions", NASA TN D-7917, October 1975.

[21] Johnson, W., "Helicopter Theory", Princeton University Press, Princeton, New Jersey, 1980.

[22] Wang, S.C., "Analytical Approach to the Induced Flow of a Helicopter Rotor in Vertical Descent", Journal of the American Helicopter Society, January, 1990.

[23] Leishman, J.G., Bhagwat, M.J., and Ananthan S., "Free-Vortex Wake Predictions of the Vortex Ring State for Single-Rotor and Multi-Rotor Configurations", American Helicopter Society 58th Annual Forum, Montréal, Canada, June 11-13, 2002.

[24] Brown, R.E., Leishman, J.G., Newman, S.J., and Perry, F.J., "Blade Twist Effects on Rotor Behavior in the Vortex Ring State", 28th European Rotorcraft Forum, Bristol, England, September 17-20, 2002.

[25] Basset, P.M., and Prasad, J.V.R., "Study of the Vortex Ring State Using Bifurcation Theory", American Helicopter Society 58th Annual Forum, Montréal, Canada, June 11-13, 2002.

[26] Glauert, H., "The Analysis of Experimental Results in the Windmill Bake and Vortex Ring States of an Airscrew", R. & M. No. 1026, British A.R.C., 1926.

[27] Padfield, R.W., "Helicopter Flight Dynamics", Blackwell Science, Oxford, 1996.

[28] Brown, R.E., Line, A.J., and Ahlin, G.A., "Fuselage and Tail-Rotor Interference Effects on Helicopter Wake Development in Descending Flight", American Helicopter Society 60th Annual Forum, Baltimore, Maryland, June 7-10, 2004.

[29] Reeder, J.P., and Gustafson, F.B., "On the Flying Qualities of Helicopters", NACA TN 1799, January 1949.

[30] Stewart, W., "Helicopter Behavior in the Vortex-Ring Conditions", Aeronautical Research Committee, R&M No. 3117, November 1951.

[31] Chen, C., Prasad, J.V.R., and Basset, P.M., "A Simplified Inflow Model of a Helicopter Rotor in Vertical Descent", American Helicopter Society 60th Annual Forum, Baltimore, Maryland, June 7-10, 2004.

[32] Prasad, J.V.R., Chen, C., Basset, P.M., and Kolb, S., "Simplified Model and Nonlinear Analysis of a Helicopter Rotor in Vortex Ring State for Flight Simulation", 30th European Rotorcraft Forum, Marseilles, France, September 14-16, 2004.

[33] Chen, C., and Prasad, J.V.R., "A Simplified Inflow Model of a Helicopter Rotor in Forward Descent", 43rd AIAA Aerospace Sciences Meeting and Exhibit, Reno, Nevada, January 10-13, 2005.

[34] Chen C., and Prasad, J.V.R., "Improvements to Vortex-Ring Model in Descent Flight", American Helicopter Society 61st Annual Forum, Grapevine, Texas, June 1-3, 2005.

[35] Chen C., and Prasad, J.V.R., "Theoretical Investigations of a Helicopter Rotor in Steep Descent", AIAA Modeling and Simulation Technologies Conference and Exhibit, San Francisco, California, August 15-18, 2005.

[36] Chen C., and Prasad, J.V.R., "A Simplified Inflow Model for Descent Flight", The 11th International Workshop on Rotorcraft Dynamics and Aeroelasticity, Boca Raton, Florida, October 12-14, 2005.

[37] Chen, C., Prasad, J.V.R., Basset, P.M., and Kolb, S., "Prediction of VRS Boundaries of Helicopters in Descent Flights", American Helicopter Society 62nd Annual Forum, Phoenix, Arizona, May 9-11, 2006.

[38] Peters, D.A., and Chen, S.Y., "Momentum Theory, Dynamic Inflow, and the Vortex Ring State", Journal of the American Helicopter Society, Vol. 27, No. 3, July 1982.

[39] He, C.J., "Development and Application of a Generalized Dynamic Wake Theory for Lifting Rotors", Ph.D. Dissertation, Georgia Institute of Technology, School of Aerospace Engineering, August 1989.

[40] Ermentrout, E., "XPPAUT 5.0 – The Differential Equations Tool", January 2001.

[41] Advance Rotorcraft Technology, Inc., "FLIGHTLAB Theory Manual", April 2001.

[42] Castles, W., and Leeuw, J.H., "The Normal Component of the Induced Velocity in the Vicinity of a Lifting Rotor and Some Examples of its Application", NACA TN 2912, 1953.

[43] Drees, J.M., and Hendal, W.P., "The field of Flow through s Helicopter Rotor Obtained from Wind Tunnel Smoke Test", Report 1535, National Aeronautical Research Institute, Amsterdam, February 1950.

[44] Leishman, J.G., Bhagwat, M.J., and Ananthan, S., "Free-Vortex Wake Predictions of the Vortex Ring State for Single-Rotor and Multi-Rotor Configurations", the 58th American Helicopter Society Annual Forum, Montréal, Canada, June 11-13, 2002.

[45] Newman, S., Brown, R., Perry, J., Lewis, S., Orchard M., and Modha, A., "Predicting the Onset of Wake Breakdown for Rotors in Descent Flight", Journal of the American Helicopter Society, Vol. 48, No. 1, January 2003.

[46] Washizu, K, Azuma, A., Koo, J., and Oka, T., "Experimental Study on the Unsteady Aerodynamics of a Tandem Rotor Operating in the Vortex Ring State", the American Helicopter Society Annual Forum, Washington, D.C., May 1966.

[47] He, C.J., "Finite State Dynamic Wake Interference Modelling for Rotorcraft Simulation", the American Helicopter Society 53rd Annual Forum, Virginia Beach, Virginia, April 29 – May 1, 1997.

[48] Zhao, J.G., "Dynamic Wake Distortion Model for Helicopter Maneuvering Flight", Ph.D. Dissertation, School of Aerospace Engineering, Georgia Institute of Technology, March 2005.

[49] Stack, J, Caradonna, F.X., and Savas, Savas, Ö, "Flow Visualizations and Extended Thrust Time Histories of Rotor Vortex Wakes in Descent", AHS 4th Decennial Specialist's Conference on Aeromechanics, San Francisco, California, January 21-23, 2004.

VITA

Chang Chen was born on 5 January 1970 in Shanghai, China. He received a Bachelor of Engineering degree from the Beijing University of Aeronautics and Astronautics in June 1991. He then worked as a research assistant on control theory and its applications at the Chinese Academy of Sciences.

Chen continued his graduate study at the Nanyang Technological University, Singapore, and obtained a Master of Engineering degree in May 1996. Upon graduation, he joined the DSO National Laboratories, Singapore, and worked on rotorcraft flight dynamic modeling and simulation. He was awarded the DSO Postgraduate Scholarship in December 2001, and enrolled in the graduate program at the Georgia Institute of Technology in August 2002, under the supervision of Dr. J.V.R. Prasad. He was awarded the Vertical Flight Foundation Scholarship from the American Helicopter Society (AHS) in June 2004. He received a Master of Science degree in Mathematics in May 2006, and is expecting a Doctor of Philosophy degree in August 2006.

Chen is currently a Senior Member of Technical Staff at DSO. He has been a member of AHS Flight Simulation Committee since 2001 and has served as Flight Simulation Session Co-Chair and Chair at the AHS 60th and 61st Annual Forums, respectively.